Spring 2020

Trend Analyses of the Abundances of Atmospheric Molecules

Anton Fernando
Old Dominion University, afern018@odu.edu

TREND ANALYSES OF THE ABUNDANCES OF ATMOSPHERIC MOLECULES

by

Anton M. Fernando
B.S. November 2011, University of Colombo, Sri Lanka
M.S. May 2014, Old Dominion University

A Thesis Submitted to the Faculty of the Department of Physics
Old Dominion University in Partial Fulfillment of the
Requirements for the Degree of

DOCTOR OF PHILOSOPHY

PHYSICS

OLD DOMINION UNIVERSITY
May 2020

Approved by:

Peter Bernath (Director)

Charles Sukenik (Member)

Anatoly Radyushkin (Member)

Alexander Godunov (Member)

Craig Bayse (Member)

ABSTRACT

TREND ANALYSES OF THE ABUNDANCES OF ATMOSPHERIC MOLECULES

Anton M. Fernando
B.S. November 2011, University of Colombo, Sri Lanka
M.S. May 2014, Old Dominion University
Old Dominion University, 2020
Director: Dr. Peter Bernath

A new linelist for the $A^3\Pi - X^3\Sigma^-$ electronic transition of NH has been prepared using line positions from the literature and calculated line intensities. High level *ab initio* calculations were performed with the `MOLPRO` program to obtain the $A - X$ transition dipole moment function. Potential energy curves and line strengths were calculated with Le Roy's `RKR1` and `LEVEL` programs. Line intensities and Einstein A values were calculated with Western's `PGOPHER` program after converting the Hund's case (b) output of `LEVEL` to Hund's case (a) input needed for `PGOPHER`. The Herman-Wallis effect is included in the Einstein A calculations of the bands for the levels with $v' = 0 - 2$ and $v'' = 0 - 6$.

Spectra of pure isobutane were recorded at high temperature in the CH stretching region (2700-3100 cm^{-1}) by high resolution Fourier transform spectroscopy. Isobutane absorption cross sections were determined for six temperatures from 273 K to 723 K. Integrated cross sections were compared with cross section data from the Pacific Northwest National Laboratory (PNNL) database.

Near global ozone isotopologue distributions have been determined from infrared solar occultation measurements of the Atmospheric Chemistry Experiment (ACE) satellite mission. ACE measurements are made with a high resolution Fourier transform spectrometer (ACE-FTS). Annual and seasonal latitudinal fractionation (δ value) distributions of the ozone isotopologues $^{16}O^{16}O^{18}O$, $^{16}O^{18}O^{16}O$ and $^{16}O^{17}O^{16}O$ were obtained. Asymmetric ozone ($^{16}O^{16}O^{18}O$) shows higher fractionation compared to symmetric ozone ($^{16}O^{18}O^{16}O$). The maximum ozone fractionation occurs in the tropical stratosphere as expected from the contribution of photolysis to the enrichment of heavy isotopologues. An enhancement of the heavy ozone isotopologues is also seen in the upper stratosphere of the Antarctic polar vortex.

A new version of ACE-FTS routine data product (4.0) provides near global VMR

altitude profiles of low altitude CO_2 on a 1 km grid from 5-18 km. An initial evaluation of these data has been carried out for the years 2004-2017 and for the month May in the 55°-70°S latitude range. The ACE-FTS data has been compared with ground-based measurements at Macquarie Island, the South Pole, the CarbonTracker 2017 model and G. Toon's empirical model. Trends agree, but ACE-FTS data has a low bias at 5.5 and 6.5 km in altitude.

The Montreal Protocol banned the production of major ozone depleting substances such as chlorofluorocarbons (CFCs) to protect the Earth's ozone layer. These halogenated compounds are inert in the troposphere and ultimately converted to HCl in the upper atmosphere. Therefore, by measuring stratospheric HCl concentrations, the effectiveness of the Montreal Protocol can be evaluated. After banning the production of CFCs, the increased production and emissions of CFC-replacement hydrofluorocarbons (HFCs) has caused a dramatic increase in their atmospheric abundances. Although these HFCs do not contribute directly to the depletion of the ozone layer because they contain no chlorine, they are powerful greenhouse gases with large global warming potentials. In January 2019, the Kigali Amendment to the Montreal Protocol came into force to phase out long-lived HFCs. The two most abundant HFCs in the atmosphere, HFC-134a (CF_3CH_2F) and HFC-23 (CHF_3), are measured from orbit by ACE-FTS. These measurements will be useful for monitoring the Kigali Amendment to the Montreal Protocol. A trend analysis of the ACE-FTS near-global measurements confirms the rapid increase in HFC-134a (4.9±0.1 ppt per year) and HFC-23 (0.75±0.02 ppt per year) volume mixing ratios (VMRs). A trend analysis has been carried out for HCl volume mixing ratio profiles provided by ACE-FTS as well; and the upper stratospheric HCl VMR time series of ACE-FTS shows a linear trend of -4.8±0.2%/decade for 2004-2017, highlighting the continuing success of the Montreal Protocol.

ACKNOWLEDGEMENTS

First of all, I would like to express my sincere gratitude to my advisor, Prof. Peter Bernath for the endless support he provided throughout my Ph.D study. His guidance, motivation and immense knowledge helped me to successfully finish my graduate studies and grow as a research scientist.

I should specially thank my office-mates, Chris Beale and Eric Buzan who supported me when I first joined the Bernath group to settle in, in my office and start my research work. Also, I should thank my batchmate Mahdi Yousefi for helping me to complete my graduate course work and providing ideas that were important for my research. The past members of the group, Drs. Robert Hargreaves, Andy Wong, James Hodges, Dan Hewett, Dan Frohman and Dror Bittner should also receive special thanks for helping with my research. I would also like to give special thanks to Dr. Mike Dulick for setting up the lab to record spectra and making early working hours an enjoyable time to work by sharing his experience and immense knowledge on many different topics. I should also acknowledge my graduate committee members for the great support and invaluable advice provided to complete my thesis. I am also thankful to Prasanna, Iranga, Eranga, Shamika, Supem, Dror, Hashir, Randika, Doug, Jamie, Junki and many others for their friendship, valuable support and advice.

One of the best things that happened to me after I came to the United States is finding a family that loves me and cares for me. I should express my sincere gratitude to my parents-in-law Tyrone Sykes and Mary Ann Sykes for their unparalleled love, care and support and to all the extended members of the Sykes family for making me feel at home. Without them, living far away from my own family would have been much harder. Also, I express my love and gratitude to my parents, brother and sister who have always been there for me, cheering and encouraging me in all of my pursuits and inspiring me to follow my dreams. Finally, I would like to express my love and appreciation to my wife Asia for keeping me happy and motivated throughout my university life. Also I am thankful to her for proofreading, providing valuable advice and insight to successfully finish my thesis.

TABLE OF CONTENTS

LIST OF TABLES

LIST OF FIGURES

CHAPTER 1

INTRODUCTION

The search for existence of life beyond the Earth and understanding the origin of our solar system have been of great interest for humans even before the birth of science. The improvement of sophisticated remote sensing techniques that are used to detect extraterrestrial objects (planets, exoplanets and stars) has provided an opportunity to achieve these goals effectively, as physically reaching them is nearly impossible. The chemical composition of the atmospheres of planets and exoplanets, interstellar clouds and stars can reveal important information about the early days of our solar system and can be used to verify whether solar system-like planetary formation and evolution models that were developed since 1950s are correct. Also, these data can be used to understand the origin of the Earth's atmosphere and its evolution as well. The emission and absorption of radiation by atoms, molecules and ions give rise to spectra; and by recording and analyzing them, the chemical composition of atoms, molecules and ions can be calculated. Spectra are recorded regularly of stars, exoplanets, comets and interstellar clouds; and among them NH is one of the molecules that is often detected. Chapter 4 provides a spectral signature (a linelist) of the NH radical, which can be used to identify NH in spectra that are recorded of extraterrestrial objects.

Titan, the largest moon of Saturn, shows similar physical properties as the pre-biotic Earth. Isobutane is one of the isomers of butane that could possibly exist in Titan [124]. Also, butane can be found in Earth's atmosphere due to anthropogenic emissions (oil and gas production) [117]. Cross sections of isobutane were determined at high temperatures to aid its detection in atmospheres of exoplanets, hot Jupiters and brown dwarfs; and are presented in Chapter 5.

Human activities such as combustion of fossil fuel, deforestation for agriculture and release of industrially utilized gases to the atmosphere have surged since the beginning of the industrial revolution in the 1750s. Due to these activities, the surface temperature of the Earth is increasing, the lower atmosphere is getting polluted and atmospheric dynamics is changing. These are the major aspects of the climate change which have become a main concern in the 21st century. In order to understand

how human activities affect the climate change, calculation of long term trends of industrial gases, atmospheric trace gases and temperature is necessary. It also helps understanding the emergence of extreme weather and the change of atmospheric circulation patterns in the lower atmosphere.

Global atmospheric circulation patterns have changed significantly because of climate change. Although accurately measuring and predicting those patterns have been a challenge, such as change of heat and moisture transport, because obtaining direct data of these processes is difficult. The dynamic vertical properties of the atmosphere, such as tropical upwelling are generally understood using general circulation models. The analysis of concentrations of isotopes in the atmosphere, relative to the main atom or molecule provides important knowledge about vertical transport, which is crucial for the accuracy of circulation models [171]. In the Earth's atmosphere, some trace gases (CO_2, O_3 and N_2O) and their isotopes show different concentrations and fractionations (concentration relative to the main atom or molecule) in different parts of the atmosphere. This is also known as the "isotopic signature" of the particular atom or the molecule. As an example, ozone shows high fractionations in the stratosphere compared to elsewhere in the atmosphere. By analyzing and tracking this isotopic signature, information on atmospheric transport and chemical reactions in the stratosphere is obtained. An analysis on the stratospheric ozone isotopic signature is provided in Chapter 6.

The temperature of the Earth's surface is increasing because greenhouse gas emissions have been increasing since the start of the industrial revolution. The most important greenhouse gas in the atmosphere is carbon dioxide (CO_2) since it is responsible for the total terrestrial greenhouse effect (20%) and controls water vapor (responsible for 50% of the total greenhouse effect) from oceans and other surface water reservoirs [77]. Also, CO_2 is the most abundant greenhouse gas in the atmosphere. The rapid rise of atmospheric carbon dioxide levels has become a major concern for climate scientists and policy makers. Therefore, the scientific community is showing a great interest in accurately measuring global atmospheric carbon dioxide concentrations and trends. Satellite based measurements provide extensive coverage of global atmospheric CO_2. ACE (Atmospheric Chemistry Experiment) is a Canadian satellite that produces volume mixing ratio (VMR) profiles of several atmospheric molecules such as CO_2. Chapter 7 presents a trend analysis of tropospheric and lower stratospheric CO_2 concentrations calculated from ACE observations that

provide useful information for global CO_2 forecasting and surface models.

The ozone layer in the Earth's atmosphere filters out deleterious ultraviolet (UV) radiation emitted by the Sun, which is associated with skin cancer, cataracts, reduced agricultural productivity and disruption of marine ecosystems. In 1974, Molina and Rowland discovered that chlorofluorocarbon (CFC) gases that were mainly used for refrigerators as a cooling agent are inert in the troposphere but photolyzed in the stratsophere and release chlorine atoms. These chlorine atoms are involved in destroying stratospheric ozone through a catalytic cycle with ozone and ultimately end up in the stratospheric HCl reservoir. Therefore, the emissions of ozone depleting substances can be monitored by measuring the stratospheric and lower tropospheric HCl concentrations. Atmospheric HCl trends derived from ACE satellite observations are presented in Chapter 8.

The Montreal Protocol is an international treaty that was signed in 1987 to control ozone depleting substances such as CFCs and halons. In accordance with the Protocol, initially, CFC and halon production was phased out. As replacements for CFCs, hydrochlorofluorocarbons (HCFCs) were used as they have smaller ozone depleting ability compared to CFCs. However, HCFCs also contain chlorine atoms and can still destroy stratospheric ozone. Therefore, under Montreal Protocol, HCFCs are now essentially phased out in developed countries but are still produced in developing countries. After phasing out HCFC production, hydrofluorocarbons (HFCs) were introduced as their replacements. Although HFCs do not deplete ozone, some of them are potent greenhouse gases. Therefore, the parties of the Montreal Protocol came to an agreement in 2016 (Kigali Amendment) to phase down HFC production as well. HFC-134a is a replacement that was used for CFC-12 and has been the most abundant HFC in the atmosphere. HFC-23 is mainly a byproduct of HCFC-22 production and is the second most abundant HFC in the atmosphere. Therefore, monitoring trends and distributions of these two atmospheric gases is important for the Kigali Amendment to the Montreal Protocol. The global trends and distributions of HFC-134a and HFC-23 based on ACE-FTS satellite measurements are provided in Chapter 8.

CHAPTER 2

ATMOSPHERIC BACKGROUND

2.1 INTRODUCTION

This chapter covers the basic principles of atmospheric science that were used for the calculations of ozone isotopologue measurements (Chapter 6), trends of low altitude CO_2 abundances (Chapter 7) and trends in atmospheric HCl, HFC-23 (CHF_3) and HFC-134a abundances (Chapter 8).

2.2 THE EARTH'S ATMOSPHERE

The Earth's atmosphere is mainly composed of nitrogen (78.08%), oxygen (20.98%) and argon (0.93%). Other important constituents in the atmosphere are greenhouse gases [35]. The most abundant and important greenhouse gases in the Earth's atmosphere are carbon dioxide (CO_2), methane (CH_4) and water vapor. Greenhouse gases absorb infrared radiation and warm the Earth enough to support life. If it was not for greenhouse gases the average temperature of the Earth's surface would be around 255 K, instead of 288 K (global mean surface temperature) which is suitable for the existence of human life.

Since the beginning of the industrial revolution in the 1750s, human activities related to energy production have caused the increase of greenhouse gases in the atmosphere and as a result, the surface temperature of the Earth has been increasing rapidly (known as global warming). Global warming has a number of negative effects on the environment including the rise of sea levels, heavy rainfall, snow cover deterioration and the change of atmospheric and oceanic circulation patterns. Therefore, monitoring and controlling these anthropogenic greenhouse gases has become a major concern. Ozone (O_3) is another important gas in the atmosphere. Ozone blocks deleterious ultraviolet radiation reaching the Earth's surface from the Sun.

2.3 VERTICAL STRUCTURE OF THE ATMOSPHERE

The Earth's atmosphere is layered based on temperature. Starting from the surface, these layers are named the troposphere, stratosphere, mesosphere, thermosphere

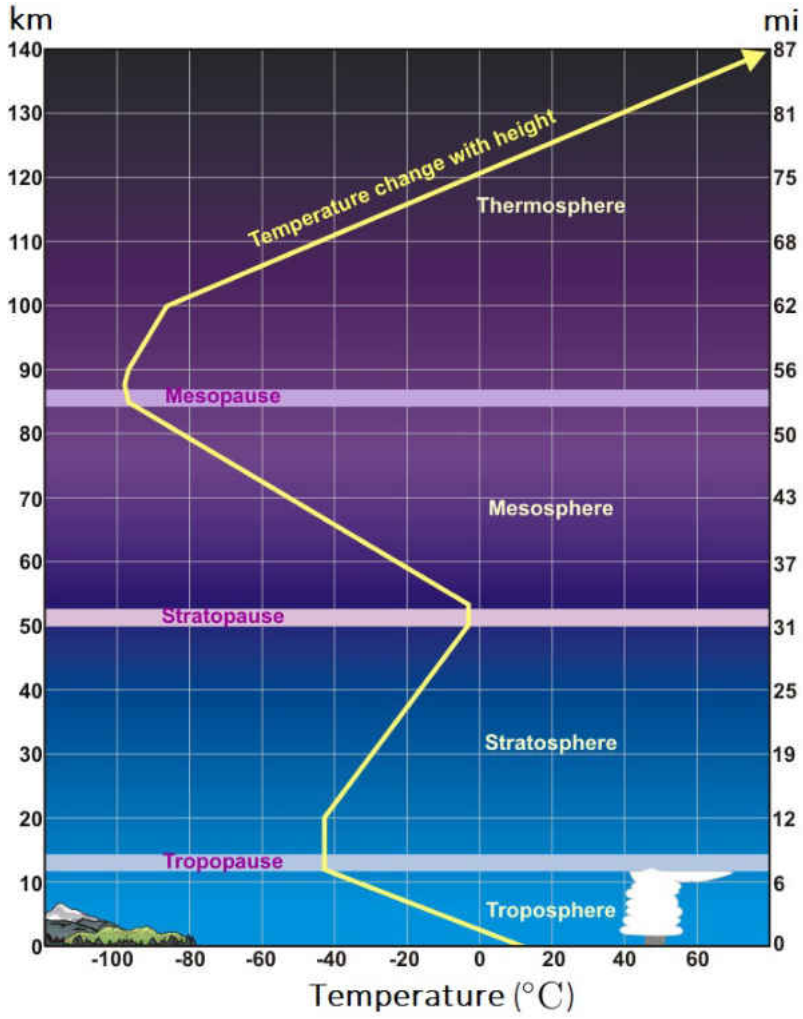

FIG. 1: Atmospheric layers based on temperature (Figure is from https://www.weather.gov/jetstream/layers).

and exosphere. The exosphere extends to the interplanetary space and gradually fades away.

2.3.1 THE TROPOSPHERE

The troposphere is the closest layer to the Earth's surface and it extends from the surface up to approximately 8-18 km depending on latitude and season. Most of the weather related activities occur with clouds, rain and snow in this part of the atmosphere. The troposphere includes 75% of the atmosphere and almost all the water vapor in the atmosphere that forms clouds and rain. The density and the

temperature of the troposphere decrease as the altitude increases. In general, the motion of air in the troposphere is governed by turbulence which is generated by thermal activity that originates from the heated Earth's surface. Turbulence helps keep tropospheric air well mixed and redistributes heat and moisture in the lower part of the Earth's atmosphere. The boundary or the sub-layer between the troposphere and the statosphere is called the tropopause. The temperature remains constant throughout this sub-layer and it acts as a barrier to air entering the stratosphere.

2.3.2 THE STRATOSPHERE

The stratosphere extends upward from the tropopause to about 50 km in altitude. The temperature of this layer increases with height because of ozone chemistry. A large amount of ozone exists in the stratosphere that absorbs ultraviolet (UV) radiation emitted by the Sun and causes a strong temperature inversion. This layer is generally stable and air mixing in it is weak compared to the troposphere. The sub-layer that lies above the stratophere is called the stratopause. In this sub-layer, the temperature remains constant with increasing height similar to the tropopause.

2.3.3 THE MESOSPHERE AND THERMOSPHERE

The mesosphere extends from the stratopause (around 50 km) to around 85 km (mesopause). The temperature in this layer again decreases with height and the minimum temperature can reach a value around -90°C. The layer above the mesopause is called the thermosphere where temperature increases again with height due to the absorption of strong UV radiation by N_2 and O_2. The mesosphere is the coldest layer of the Earth's atmosphere and the thermosphere is the hottest.

2.3.4 ATMOSPHERIC MEASUREMENTS

There are two measurement types that can be used to study atmospheric composition: *in situ* and remote sensing measurements. In order to take *in situ* measurements, it requires measuring instruments to be located at the point where measurements are taken and be in contact with the subject of interest. In *in situ* measurements, samples are collected on the ground or from balloons, aircraft and rockets. These collected samples can be analyzed at the point of collection or sending them to the ground.

The basic idea of remote sensing is collecting data of an object without making physical contact with it. Generally, remote sensing manipulates electromagnetic radiation to collect information. Depending on how physical objects interact with electromagnetic radiation, remote sensing systems can be classified into two categories: passive systems and active systems. In passive systems, natually occuring electromagenetic (EM) radiation is used, while in active systems manipulated and artificially generated radiation is utilized. Active systems can use EM radiation at any wavelength. Passive remote sensing systems can be further divided into two subcategories: systems that detect thermal radiation and systems that detect radiation emitted by the Sun. Objects with typical terrestrial temperatures emit radiation in the thermal infrared region at wavelengths on the order of 10 μm and also some measurements can be obtained at longer wavelengths (microwave region). There are two main 'windows' that the atmosphere is transparent. The first window includes visible and infrared parts of the spectrum between wavelengths around 0.3 μm and 10 μm. The second window region corresponds to the microwave region (between wavelengths of a few millimeters and a few meters).

2.4 SATELLITE REMOTE SENSING

Satellite remote sensing is one of the technologies that is used to gather global atmospheric information with sensors mounted on satellites. Monitoring global measurements from the orbit provides excellent spatial coverage that is difficult to obtain from ground-based, aircraft and balloon platforms. There are two main geometrical methods that are used in passive satellite remote sensing: vertical (nadir) and horizontal (limb). Nadir-viewing is looking straight down and limb-view is looking at the edge of the atmosphere to detect radiation (Figure 2). Similarly, solar occultation measurements are taken in the limb-view through the atmosphere using the Sun as a light source. This process is carried out for different tangent heights with increasing altitude during a sunrise and decreasing altitude during a sunset. In this method, a slant column is used for each measurement that includes multiple atmospheric layers which contain information on the atmosphere. Figure 3 shows the solar occultation measurements taken by the ACE satellite.

2.5 ACE SATELLITE

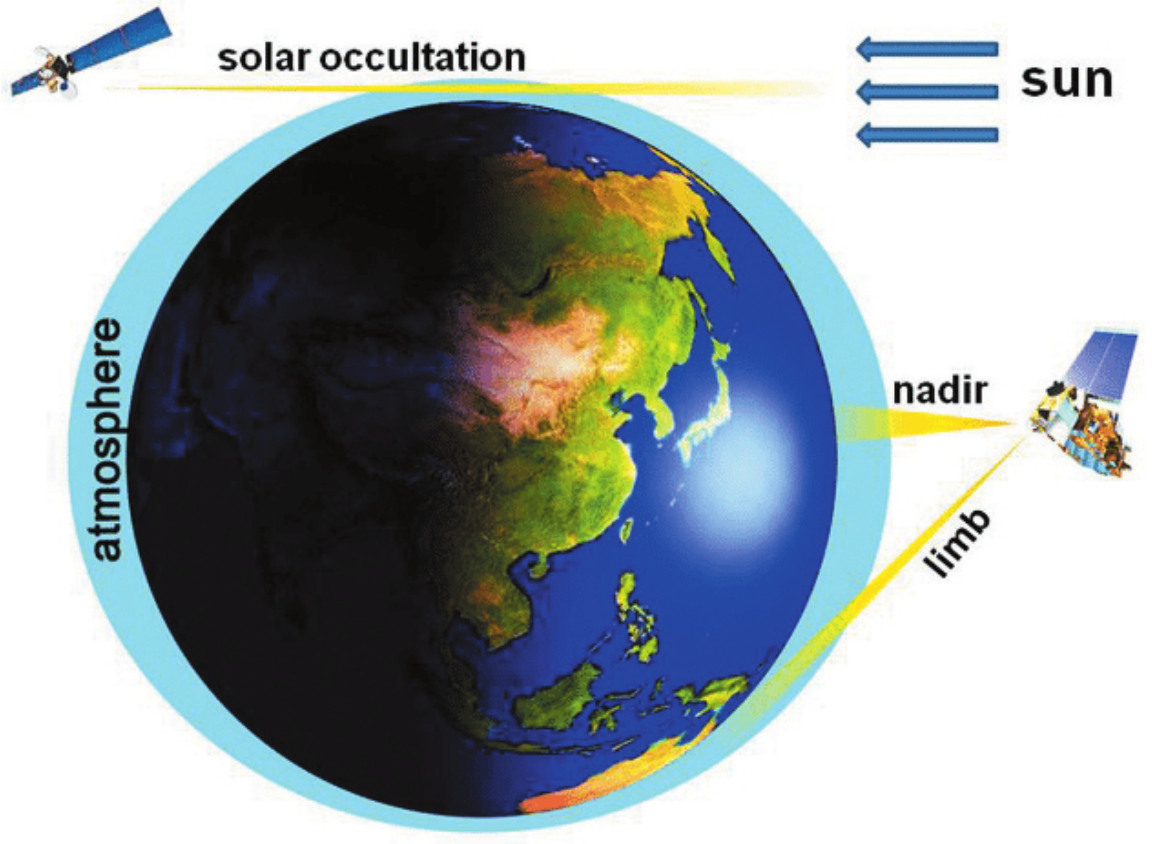

FIG. 2: Satellite remote sensing geometries [82].

ACE (Atmospheric Chemistry Experiment), also known as SCISAT is a Canadian satellite which was launched in August 2003 and is still in operation. The main goal of the ACE mission is to understand the chemical and dynamical processes that affect the ozone distribution in the upper troposphere and the stratosphere. The satellite has a high inclination (74°) relative to the equator and a low circular orbit (650 km) that gives coverage of tropical, mid-latitude and polar regions (about 85°S to 85°N). The ACE satellite is in a precessing orbit and the latitudes of occultations for one year are shown in Figure 4. As shown in Figure 4, there are no occultations of certain periods in December and June because the orbit plane of the satellite is nearly perpendicular to the Earth-Sun vector. There are up to 30 occultations per day, 15 sunrises and 15 sunsets, distributed along two longitude circles about the Earth [11]. ACE satellite contains two instruments, the ACE-FTS and MAESTRO (Measurements of Aerosol Extinction in the Stratosphere and Troposphere Retrieved by Occultation). MAESTRO is a dual optical UV-visible spectrometer,

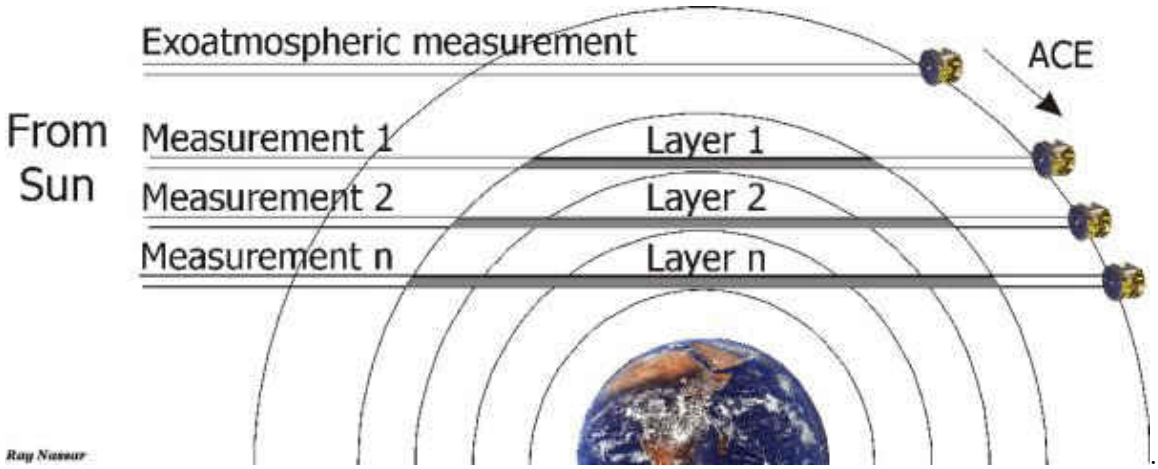

FIG. 3: Solar occultation measurements by the ACE satellite. (Figure is from https://spaceq.ca/as-scisat-approaches-its-15th-anniversary-theres-no-other-satellite-like-it-and-no-funding-to-replace-it/.)

but will not be discussed in detail, since the data from MAESTRO was not used for our calculations. The ACE-FTS is a high-resolution (0.02 cm^{-1}) Fourier transform spectrometer (FTS), operating in the spectral region 2 to 13 microns (750 - 4100 cm^{-1}). The ACE-FTS takes measurements of thin clouds, aerosols, temperature and vertical volume mixing ratios (VMRs) of trace gases. The ACE-FTS records infrared absorption spectra every 2 s, that contain information on atmospheric layers, with solar occultation method during sunset and sunrise (Figure 3). The vertical resolution of measurements is about 3 - 4 km from the cloud tops (> 5 km) to about 150 km [9].

ACE measurements can be used to monitor long-term global trends of atmospheric composition because of high precision and accuracy. The recorded ACE-FTS interferograms are sent to the ground and Fourier transformed into transmission spectra at the University of Waterloo. The sequence of spectra recorded is analyzed using software written by C. Boone (University of Waterloo) that converts data into VMR profiles.

Depending on prior meteorogical information to obtain pressure and temperature profiles for quantitative analysis is not reliable. Therefore, retrieval of pressure and temperature is done as the first step of the ACE-FTS data processing for each occultation. In order to obtain temperature from recorded spectra, fixed CO_2 VMRs are assumed in the altitude range of about 10 to 65 km. Relative CO_2 line intensities

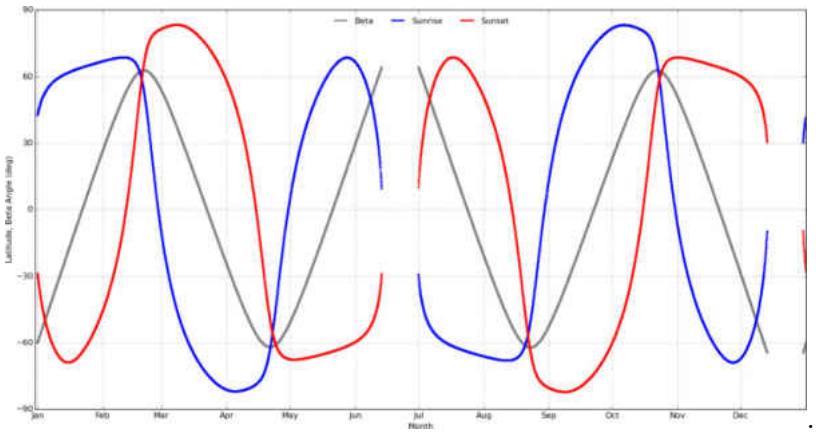

FIG. 4: Latitudes of the occultations of the ACE satellite for 1 year (2015) and the beta angle (angle between the orbital plane and a line drawn from the Sun to the Earth) of the orbit [11].

are used to calculate temperature and absolute line intensities to calculate atmospheric pressure. These pressure values were then converted into altitudes using data from the operational weather analyses of the Canadian Meteorological Center. The temperature and VMR profiles of molecules are finally calculated by comparing the observed and calculated spectra, adjusting the parameters of interest until a certain threshold criteria is achieved. The calculated transmission spectra are analyzed using the Beer-Lambert law to obtain VMR profiles of the molecules [15].

2.6 DYNAMICS AND CHEMISTRY OF THE EARTH'S ATMOSPHERE

2.6.1 THE METEOROLOGICAL SEASONS

It is useful to divide the year into seasons (Summer, Fall, Winter and Spring) when analyzing atmospheric data because of temperature variations. The effect of the seasons becomes clearly visible when moving further to the polar regions from the equator. The Earth has seasons because the rotational axis of the Earth is tilted at an angle of 23.5° relative to the orbital plane. In order to be consistent with accurate climatological statistics, as a convention, it is considered that Summer starts on June 1st and ends on August 31st, Fall runs from September 1st to November 30th, Winter from December 1st to February 28/29 and Spring from March 1st to May 31st. These seasons are called meteorological seasons, even though they are not

directly related to any physical phenomena. On the other hand, the astronomical seasons are defined based on the position of the Earth relative to the Sun. But in this study, for convenience the meteorological seasons are used for data analysis.

2.6.2 TIME SCALES FOR VERTICAL AND HORIZONTAL ATMOSPHERIC TRANSPORT

Atmospheric circulation in the troposphere is governed by turbulence. Turbulence is defined as small-scale irregular motion of air with varying speeds and directions. Tropospheric molecules with longer lifetimes are generally well-mixed due to the turbulent nature of the troposphere. Vertical time scale of the lower part of the Earth's atmosphere (mean time it takes by an air molecule to travel a vertical distance) is given in Figure 5. It takes about one month for air to travel vertically from the surface to the tropopause, 5 - 10 years from the troposphere to the stratosphere and 1 - 2 years from the stratosphere to the troposphere [63].

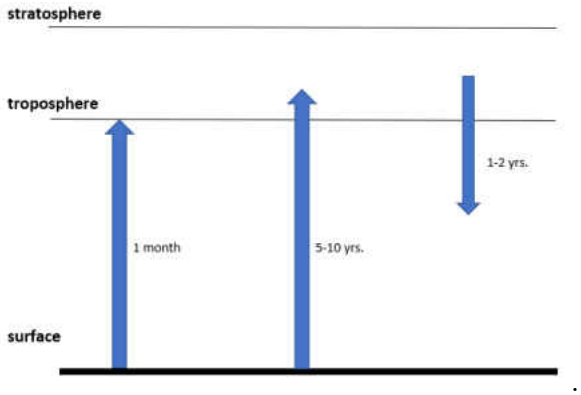

FIG. 5: Characteristic time scale for vertical transport of the Earth's lower atmosphere [63].

Typical time scale for horizontal transport in the troposphere is shown in Figure 6. Due to geostrophic flow by the latitudinal heating gradient, it takes about two weeks for air to circumnavigate the Earth in a given latitudinal band. It takes 1 -2 months for air to travel from mid-latitudes to polar and tropical regions and about a year for hemispheres to exchange air [63].

2.6.3 BREWER-DOBSON CIRCULATION

Brewer-Dobson ciculation is an atmospheric circulation (Figure 7) that explains

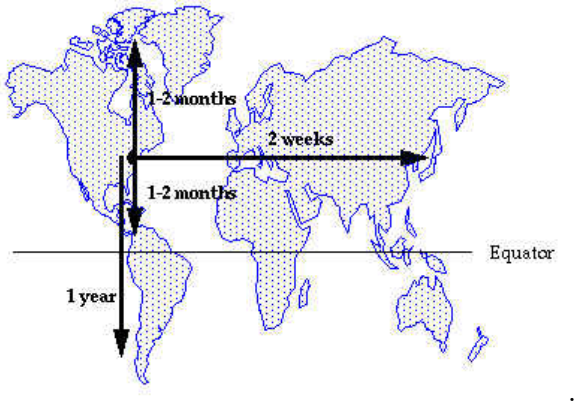

FIG. 6: Characteristic time scale for horizontal transport of the troposphere [63].

why there is high ozone concentrations in the Arctic during spring and low concentrations in the tropics, although, most of ozone is produced in the tropical stratosphere [21]. The basic idea of the Brewer-Dobson model is that tropical air circulates into the stratosphere through the tropical tropopause, moves towards polar regions and sinks into middle and polar latitudes of the stratosphere [128].

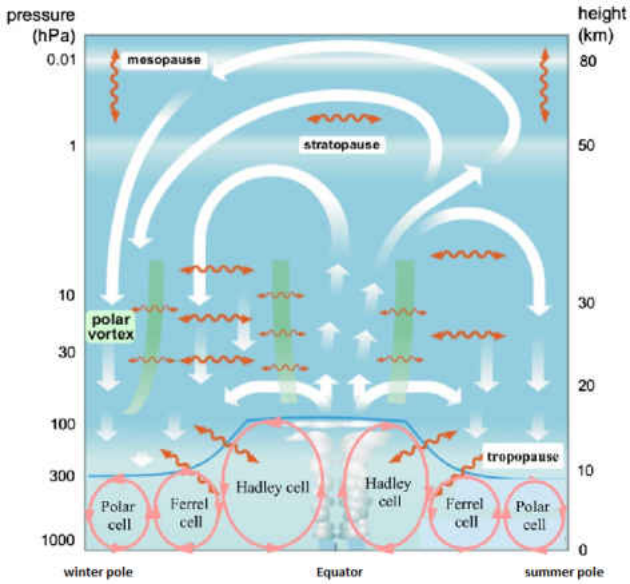

FIG. 7: The Brewer-Dobson circulation in the present day Earth [121].

2.7 CHAPMAN MECHANISM

The existence of the ozone layer in the stratosphere was first explained by a

British scientist, Chapman in 1930, by a set of reactions, known as the *Chapman mechanism* (Figure 8). Chapman suggested that the ozone layer exists because of the photolysis of atmospheric O_2. The bond energy of the O_2 molecule is around 498 kJ mol^{-1} and only photons with wavelengths less than 240 nm can photolyze the molecule. Such high energy photons are present only in high altitudes (ultraviolet radiation). Photolysis of O_2 produces two O atoms (R1) and combine rapidly with O_2 molecules (R2) to produce ozone (where M is a third body). The bonds in the O_3 molecule are weaker than those in the O_2 molecule. Therefore, photolysis of O_3 (R3) occurs with lower energy photons (< 320 nm). Finally, ozone and atomic oxygen recombine to produce oxygen to terminate the reaction cycle (R4).

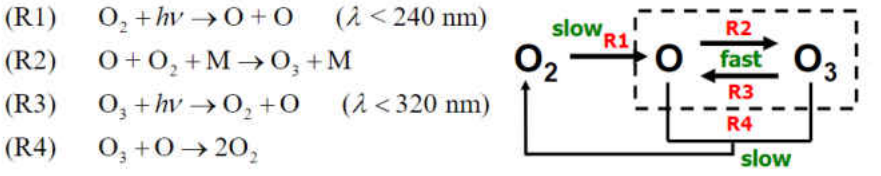

FIG. 8: The Chapman mechanism (Figure is from https://www.slideserve.com/radwan/chapman-mechanism-for-stratospheric-ozone-1930).

CHAPTER 3

SPECTROSCOPIC BACKGROUND

3.1 INTRODUCTION

This chapter covers the basic principles of spectroscopy and Fourier transform measurements utilized for the calculations of the linelist of the $A^3\Pi$ - $X^3\Sigma^-$ transition of the NH free radical (Chapter 4) and cross section calculations for isobutane (Chapter 5). The majority of the text presented in this chapter is adopted from the books Bernath [10], Cramer [24], Hollas [60], Herzberg [56] and Levine [84].

Spectroscopy is a branch of science that studies interaction between EM radiation and matter with electromagnetic spectra. Generally, spectroscopy is used to recognize atoms and molecules, calculate molecular abundances and determine molecular structure. Atomic and molecular spectra result from absorption or emission of photons between quantized energy levels. When molecules absorb radiation, it can cause transitions between electronic, vibrational and rotational energy levels and also can dissociate the molecule. In general, rotational transitions occur when microwave radiation is absorbed, vibrational transitions when infrared radiation is absorbed and electronic transitions when visible/ultraviolet radiation is absorbed.

3.2 ROTATIONAL SPECTROSCOPY

In this section, theories related only to diatomic molecules are discussed to focus on the results presented in this dissertation. Pure rotational transitions of any molecule can be understood through a classical rigid rotor. The moment of inertia of a diatomic rigid rotor is given by

$$I = \sum_{i=1}^{2} m_i {r_i}^2, \tag{1}$$

where I_i represents the moment of inertia about any axis through the center of mass, m_i represents the mass of atom i and r_i is the distance of atom i from the considered axis. The classical energy of a diatomic rigid rotor is given by

$$E_{\mathrm{R}} = I(\omega_{\mathrm{x}}{}^2 + \omega_{\mathrm{y}}{}^2) = \frac{J^2}{2I} \tag{2}$$

where E_{R} is the rotational energy, I is the moment of inertia (moment of inertia in the x and y direction are the same and 0 in the z direction) and ω_{x} and ω_{y} are the angular velocities in the x and y directions. In quantum mechanics, the angular momentum operator is $\hat{J}$. Therefore, the rotational Hamiltonian operator for a rigid rotor (linear molecule) is

$$\hat{H} = \frac{\hat{J}^2}{2I} \qquad \text{for } J = 0, 1, 2... \tag{3}$$

The Schrödinger equation for a diatomic rigid rotor is

$$\frac{\hat{J}^2}{2I}\psi = E\psi, \tag{4}$$

so that

$$\frac{\hat{J}^2}{2I}\psi = \frac{J(J+1)\hbar^2}{2I}\psi = BJ(J+1)\psi = F(J)\psi, \tag{5}$$

in which

$$B = \frac{\hbar^2}{2I}, \tag{6}$$

where B is known as the rotational constant and $F(J)$ is the energy eigenvalue function, given in SI units. Energy transitions between the rotational energy states can occur when $\Delta J{=}\pm 1$ and with frequencies,

$$\begin{aligned} \nu_{J+1\leftarrow J} &= F(J') - F(J'') \\ &= B(J+1)(J+2) - BJ(J+1) \\ &= 2B(J+1). \end{aligned} \tag{7}$$

In general, upper states are indicated by primes (J') and first and lower states are indicated by double primes (J''). The population of a rotational state can be calculated by statistical mechanics as

$$N_J = N(2J+1)\frac{e^{-BJ(J+1)/kT}}{q_r} = NP_J, \tag{8}$$

where

$$q_r = \sum_J (2J+1) e^{-BJ(J+1)/kT}, \tag{9}$$

T is the temperature, k is the Boltzmann constant, N is the total concentration of the molecules and P_J is the population probability of rotational level J (N_J is the concentration of the molecules with the rotational quantum number J and q_r is the partition function).

In general, molecules are not strictly rigid rotors. As a molecule rotates, the nuclei tend to be thrown outward by centrifugal forces. Therefore, as the angular velocity or rotational quantum number (J) of a molecule increases, intermolecular distance (r) between the atoms of that molecule also increases. Therefore, the rotational constant B is J-dependent. In order to account for this centrifugal distortion, the energy eigenvalue function should be modified as

$$F(J) = BJ(J+1) - D(J(J+1))^2 + H(J(J+1))^3 + L(J(J+1))^4..., \tag{10}$$

where D is defined as the centrifugal distortion constant and H and L are higher order distortion constants.

3.3 VIBRATIONAL SPECTROSCOPY

Vibrational energy of a diatomic molecule is obtained with the simple harmonic oscillator approximation. A non-rotating diatomic molecule can be considered as a spring that follows Hooke's law. If the spring constant is K, the Hamiltonian can be written as

$$\hat{H} = \frac{-\hbar^2}{2\mu}\frac{d^2}{dr^2} + \frac{K(r-r_{\mathrm{e}})^2}{2}, \tag{11}$$

where r is the internuclear distance and r_{e} is the equilibrium internuclear distance and $\mu[=m_1 m_2/(m_1+m_2)]$ is the reduced mass. The vibrational energy eigenvalues are obtained by solving the Schrödinger equation as

$$E_v = h\nu(v+\frac{1}{2}) \qquad \text{for } v = 0, 1, 2..., \tag{12}$$

where the pure vibrational energy is E_v, the vibrational frequency is $\nu[=\frac{1}{2\pi}(\frac{K}{\mu})^{1/2}]$ and the vibrational quantum number is $v = 0,\ 1,\ 2...$ The vibrational term value $G(v)$ of a diatomic molecule is given by

$$\frac{E_v}{hc} = G(v) = \omega(v + \frac{1}{2}) \qquad \text{for } v = 0, 1, 2..., \tag{13}$$

where ω is the vibrational wave number.

The potential energy curve of a diatomic molecule (anharmonic oscillator) is commonly represented by the Morse potential to account for anharmonic behavior. The Morse potential is written as

$$V(r) = D(1 - e^{-\beta(r - r_e)})^2. \tag{14}$$

Therefore, anharmonic vibrational terms of the energy expression is modified to

$$G(v) = \omega_e(v + \frac{1}{2}) - \omega_e x_e(v + \frac{1}{2})^2, \tag{15}$$

where ω_e is the vibrational constant and $\omega_e y_e$ is the anharmonic constant. Similarly, the rotational energy function is modified to

$$F(J) = B_e J(J+1) - D_e(J(J+1))^2 - \alpha_e(v + \frac{1}{2})J(J+1), \tag{16}$$

where B_e, D_e and α_e are equilibrium constants.
An anharmonic oscillator can be represented by Dunham potential which is an even more general representation than the Morse potential.

In the Dunham potential, the vibrational energy level expression is written as

$$G(v) = \omega_e(v + \frac{1}{2}) - \omega_e x_e(v + \frac{1}{2})^2 + \omega_e y_e(v + \frac{1}{2})^3 + \omega_e z_e(v + \frac{1}{2})^4..., \tag{17}$$

and the parameterized rotational energy expression is written as

$$F_v(J) = B_v J(J+1) - D_v(J(J+1))^2 + H_v(J(J+1))^3 + ... \tag{18}$$

in which

$$B_v = B_e - \alpha_e(v + \frac{1}{2}) + \gamma_e(v + \frac{1}{2})^2 + ..., \tag{19}$$

and

$$D_v = D_{\mathrm{e}} - \beta_{\mathrm{e}}(v + \frac{1}{2}) + ... \tag{20}$$

where B_v, D_v, H, ω_e, $\omega_e x_e$, $\omega_e y_e$, $\omega_e z_e$, B_e, α_e, γ_e, D_e and β_e are spectroscopic constants.

3.4 ELECTRONIC SPECTROSCOPY

Electronic spectroscopy is the study of transitions between electronic states. In electronic spectroscopy of molecules, vibrational and rotational transitions (Figure 9) must be taken into account.

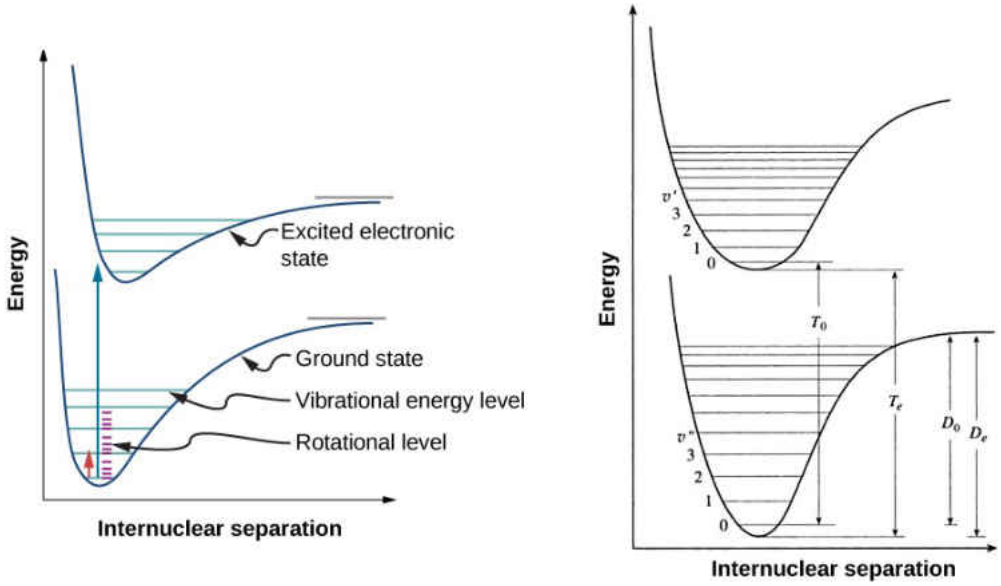

FIG. 9: Two dimensional representation of anharmonic potential energy curve for two electronic states with vibrational-rotational states. (Figure is from https://chem.libretexts.org.)

3.5 BORN-OPPENHEIMER APPROXIMATION

The Born-Oppenheimer approximation is the assumption that is used to separate the motion of the nuclei and the electrons of molecules. This allows the discussion of rotational and vibrational motion of the nuclei of a molecule, ignoring the motion of electrons. In Born-Oppenheimer approximation, it is assumed that the nuclei in a molecule are much heavier than the electrons and the electrons move much faster

than the nuclei. Therefore, the nuclei are considered to be fixed while the electrons are moving relative to them and the nuclear kinetic energy is considered a constant. The equations of the Born-Oppenheimer approximation are

$$(\hat{H}_{el} + V_{NN})\psi_{el} = U\psi_{el} \tag{21}$$

and

$$U = E_{el} + V_{NN}, \tag{22}$$

where ψ_{el} is the electronic wavefunction, V_{NN} is the nuclear-nuclear energy at a fixed geometry, $\hat{H}_{el}$ is the electronic Hamiltonian; and E_{el} is the electronic energy that includes the kinetic energy of the electrons, the potential energy of the attraction between the electrons and the nuclei and the potential energy of the repulsion between the electrons.

3.6 HETERONUCLEAR MOLECULES

Electrons of diatomic heteronuclear molecules like NH (contains 8 electrons; 7 from N and 1 from H) can be filled into MOs (molecular orbitals). N (nitrogen) has 5 valence electrons and H has 1. H has $1s$ (l=0; m_l=0) valence orbital and N has $2s$ (l=0; m_l=0), $2p_1$ (l=1; m_l=1), $2p_{-1}$ (l=1; m_l=-1) and $2p_0$ (l=1; m_l=0). Here, l is the angular momentum quantum number and m_l is the magnetic quantum number of the electrons.

3.7 MOLECULAR-ORBITAL THEORY

In molecular orbital theory, the occupied electrons in a heteronuclear diatomic molecule are considered to be associated with both the nuclei. It is assumed that molecular orbitals are linear combinations of atomic orbitals. These molecular orbitals can be formed by adding and subtracting appropriate atomic orbitals. This method is usually called LCAO-MO (linear combination of atomic orbitals-molecular orbitals).

The approximate wavefunctions of molecular orbitals σ and σ^* are,

$$\psi(\sigma) = C_1 1s_a + C_2 1s_b, \tag{23}$$

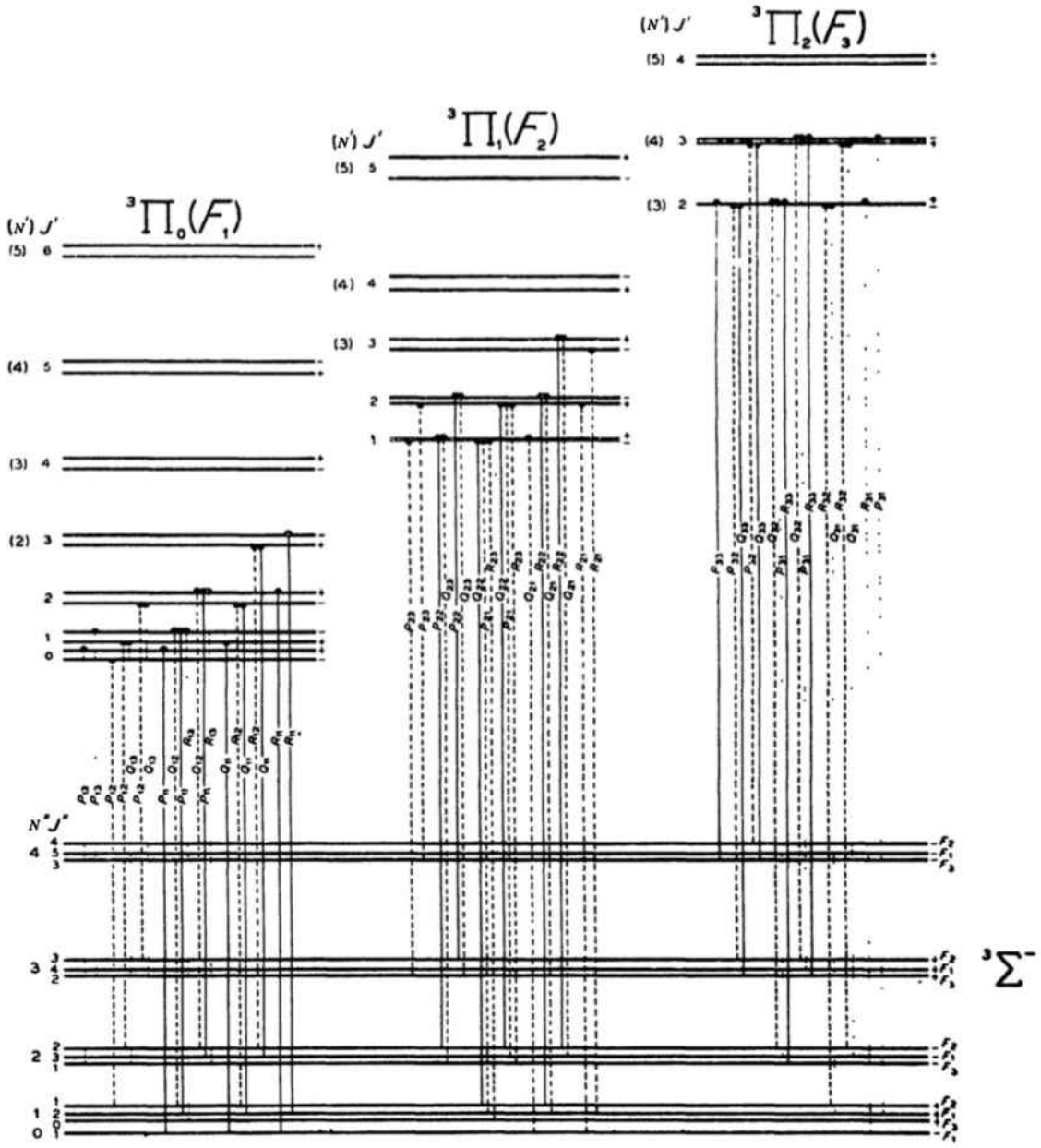

FIG. 10: Energy Level Diagram for the first lines of a $A^3\Pi$ - $X^3\Sigma^-$ Band: The Λ type doubling in the upper state and the spin tripling in the lower state is much exaggerated. The triplet splitting splitting of the upper state is usually much larger. If the upper state is strictly a case (a) state all 27 branches indicated have comparable intensities. In going over to case (b) the branches indicated by dotted lines ($\Delta N{=}\Delta J{\pm}2$) and those indicated by broken lines ($\Delta N{=}\Delta J{\pm}1$) become weaker or disappear altogether. Some of them go over into the satellite branches of case (b) [56].

$$\psi(\sigma^*) = C_3 1s_a - C_4 1s_b, \tag{24}$$

$$\psi(\sigma_z) = C_5 2p_{z_a} + C_6 2p_{z_b}, \tag{25}$$

$$\psi(\sigma^*{}_z) = C_7 2p_{z_a} - C_8 2p_{z_b}, \tag{26}$$

where $C_{1...16}$ are positive constants; and $1s$ and $2p_{x,y,z}$ are atomic orbitals (labels a and b represent different nuclei).
Similarly, the approximate wavefunctions of π type orbitals can be written as

$$\psi(\pi_x) = C_9 2p_{x_a} + C_{10} 2p_{x_b}, \tag{27}$$

$$\psi(\pi_x{}^*) = C_{11} 2p_{x_a} - C_{12} 2p_{x_b}, \tag{28}$$

$$\psi(\pi_y) = C_{13} 2p_{y_a} + C_{14} 2p_{y_b}, \tag{29}$$

$$\psi(\pi_y{}^*) = C_{15} 2p_{y_a} - C_{16} 2p_{y_b}. \tag{30}$$

The ground ($X^3\Sigma^-$) and the first excited ($A^3\Pi$) electronic states are shown in the molecular orbital diagram (Figure 11). The label X is used to indicate the ground electronic state, while A, B and C are used for excited states of the same multiplicity. σ and σ^* molecular orbitals are composed of the $1s$ valence atomic orbital of the H atom and the $2p_z$ valence atomic orbital of the N atom of the NH molecule. The $2s$ valence atomic orbital of the N atom does not bond with the $1s$ valence atomic orbital of the H atom. Therefore, the energy of the non-bonding molecular orbital σ^{nb} is as same as the energy of the $2s$ valence atomic orbital of the N atom. Similarly,

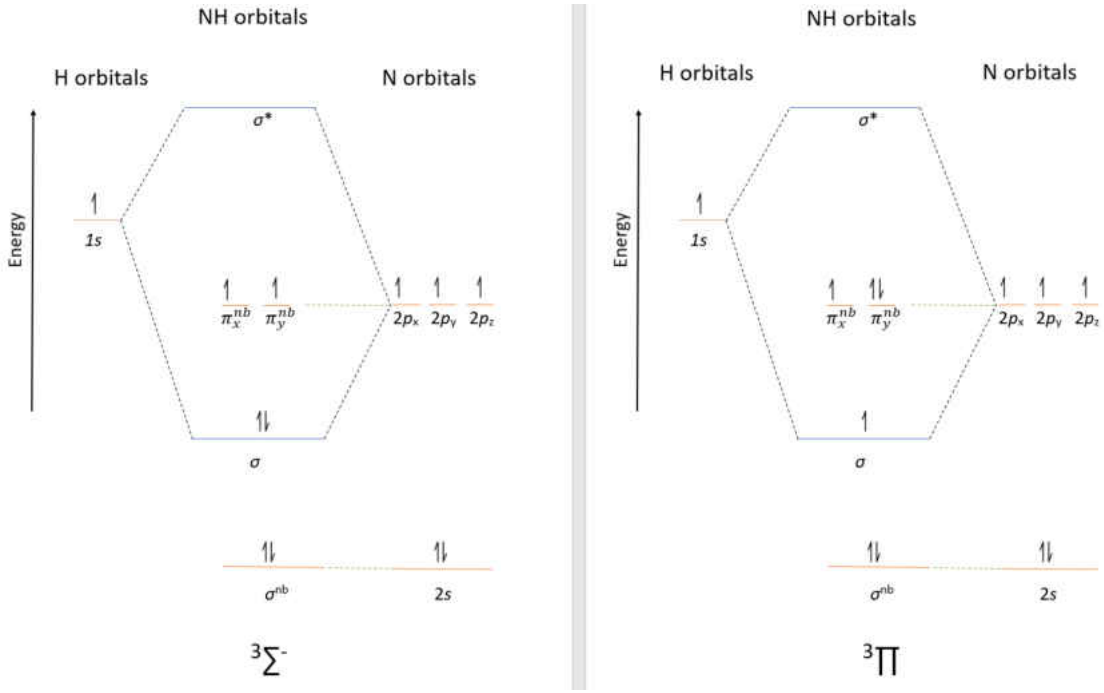

FIG. 11: Orbital diagram of the electronic states $^3\Sigma^-$ and $^3\Pi$ for NH

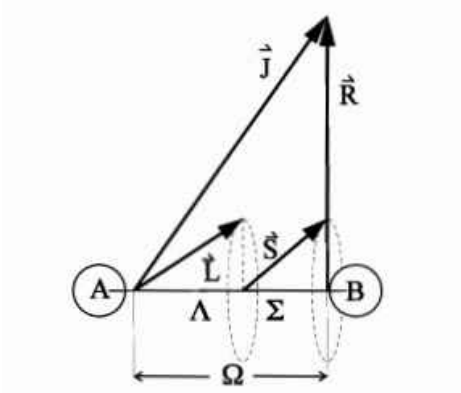

FIG. 12: Angular momenta in a diatomic molecule (Hund's case (a)) [10]

since the H atom has no valence atomic orbitals capable of π-type interaction the energy of the non-bonding molecular orbitals ${\pi_x}^{\rm nb}$ and ${\pi_y}^{\rm nb}$ are as same as the energy of the valence atomic orbitals $2p_x$ and $2p_y$.

3.8 CLASSIFICATION OF ELECTRONIC STATES

TABLE 1: Useful quantum numbers in electronic spectroscopy

Angular momenta	notation	projection on molecular axis (unit $\hbar$)
total	$\boldsymbol{J}$	$\Omega = (\Lambda + \Sigma)$
electronic orbital	$\boldsymbol{L}$	Λ
spin	$\boldsymbol{S}$	Σ
nuclear rotational	$\boldsymbol{R}$	-
angular momentum	$\boldsymbol{N} = \boldsymbol{R} + \boldsymbol{L}$	Λ
nuclear spin	$\boldsymbol{I}$	-

The relevant quantum numbers attributed to rotational and electronic motion of a non-vibrating diatomic molecules are given in the Table 1. The total angular momentum ($\boldsymbol{J} = \boldsymbol{L} + \boldsymbol{S} + \boldsymbol{R}$) is the vector sum of orbital $\boldsymbol{L}$, spin $\boldsymbol{S}$ and nuclear rotation $\boldsymbol{R}$ momenta.

In general, electrons in an atom move in a spherically symmetric force field. Therefore, electronic orbital angular momentum $\boldsymbol{L}$ is a constant of motion as long as spin-orbit coupling is small. In a diatomic molecule, electrons move in a force field that contains axial symmetry about the internuclear axis. Therefore, as a consequence instead of the electronic orbital angular momentum, the projection on the molecular axis (Λ) becomes a constant of motion. Therefore, it is useful to classify electronic states of diatomic molecules with the quantum number Λ that is designated by Σ, Π, Δ, Φ... corresponding to $\Lambda = 0, 1, 2, 3, 4$...

For diatomic molecules, the orbital angular momenta of all electrons are coupled to give a resultant $\boldsymbol{L}$ and all the spin momenta give a resultant $\boldsymbol{S}$. In Hund's case (a) (Figure 12), it is assumed that the electronic motion is coupled very strongly to the electrostatic field produced by the two nuclear charges. Therefore, in Hund's case (a) electronic angular momentum Λ is well defined and $\boldsymbol{L}$ is not considered to be a good quantum number. Λ can take values,

$$\Lambda = 0, 1, 2, 3... \tag{31}$$

and all electronic states with $\Lambda > 0$ are doubly degenerate (In Hund's case (b), the spin vector is not coupled to the internuclear axis at all or weakly coupled and hence Ω is not well defined). In Hund's case (a), the spin angular momentum (Σ) is also

coupled to the internuclear axis as the magnetic field originating from electronic orbital momenta is along the axis. The spin component of $\boldsymbol{S}$ along the internuclear axis is $\Sigma\hbar$. The quantum number Σ can take values;

$$\Sigma = S,\ S\text{-}1,\ldots,\text{-}S.... \tag{32}$$

The total angular momentum along the internuclear axis Ω is sometimes appended as a subscript to label spin components. In spin component representation, although $\Omega > 0$ states are doubly degenerate, $|\Omega|$ is used to represent both values. For states with $\Sigma > 0$, there are spin components and $2S+1$ is designated by a pre-superscript in the electronic state. As an example, $^3\Pi$ has 3 spin components, which are $^3\Pi_0$, $^3\Pi_1$ and $^3\Pi_2$.

Spin-orbit interaction energy in Hund's case (a) is

$$\Delta E = A\Lambda\Sigma, \tag{33}$$

where A is the spin-orbit coupling constant.

When $\Sigma = 0$, there is no resulting magnetic field to couple $\boldsymbol{S}$ to the internuclear axis. As a result, there is only one component for Σ states and it should be treated as Hund's case (b), whatever the multiplicity is.

The energy level diagram of the ground state and the first excited electronic state with the same multiplicity of the diatomic molecule NH is illustrated in the Figure 10.

3.9 SYMMETRY PROPERTIES OF THE WAVEFUNCTION

In a heteronuclear diatomic molecule, the reflection in the plane through the internuclear axis (which is a plane of symmetry) of the electronic eigenfunction of a non-degenerate (e.g. Σ) state may or may not change sign. Depending on its sign the states will be called + or − (e.g. Σ^+ or Σ^-).

Total (+/-)parity: Total parity operator ($\hat{E}^*$) is an important property as it determines the selection rules of transitions between states. Once the symmetry operator is applied to the total wavefunction exclusive of nuclear spin, it inverts all the coordinates of the particles in the molecule as

$$\begin{aligned} \hat{E}^{*}\psi(X_i, Y_i, Z_i) &= \psi(-X_i, -Y_i, -Z_i) \\ &= \pm\psi(X_i, Y_i, Z_i). \end{aligned} \tag{34}$$

Rotationless (e/f) parity: Total parity changes with rotational quantum number J. Therefore, it is useful to define a parity excluding the rotational dependence and it is defined as

$$\begin{aligned} \hat{E}^{*}\psi &= +(-1)^{J}\psi \ \text{ for } \ e \\ &= -(-1)^{J}\psi \ \text{ for } \ f \end{aligned} \tag{35}$$

for integer J. Similarly, for half-integer J,

$$\begin{aligned} \hat{E}^{*}\psi &= +(-1)^{J\text{-}1/2}\psi \ \text{ for } \ e \\ &= -(-1)^{J\text{-}1/2}\psi \ \text{ for } \ f. \end{aligned} \tag{36}$$

3.10 ELECTRONIC DIPOLE SELECTION RULES FOR HETERONUCLEAR DIATOMIC MOLECULES

Rotational:

1) The molecule must have a permanent dipole moment.

2) $\Delta J = 0, \pm 1$

Vibrational:

1) First derivative of the dipole moment of the molecule must be non-zero.

2) $\Delta v = \pm 1$ (± 2, ± 3,... are weak)

Electronic: 1) $\Delta\Lambda = 0, \pm 1$

For example, Σ - Σ, Π - Σ, Δ - Π transitions are allowed and Δ - Σ or Φ - Π are not.

2) $\Delta S = 0$

This selection rule breaks down when the nuclear charge in the molecule increases.

3) $\Delta\Sigma = 0$; $\Delta\Omega = 0, \pm 1$ for transitions between multiplet components.

4) $+ \not\leftrightarrow -$; $+ \leftrightarrow +$; $- \leftrightarrow -$ For Σ - Σ transitions only Σ^{+} - Σ^{+} and Σ^{-} - Σ^{-} transitions are allowed.

5) Between rotational-vibrational-electronic (rovibronic) energy levels, $\Delta J = 0, \pm 1$ transitions are allowed. In rovibronic interactions, $\Delta J = 0$ transitions are called the Q branch, $\Delta J = -1$ the P branch and $\Delta J = +1$ the R branch.

6) The general selection rules of rovibronic transitons can be defined with total parity and e/f parity as

$+ \leftrightarrow$ -; $+ \not\leftrightarrow +$; - $\not\leftrightarrow$ - (for total parity)

$e \leftrightarrow f$; $e \not\leftrightarrow e$; $f \not\leftrightarrow f$ for $\Delta J = 0$

$e \not\leftrightarrow f$; $e \leftrightarrow e$; $f \leftrightarrow f$ for $\Delta J = \pm 1$.

3.11 COMPUTATIONAL SPECTROSCOPY

3.11.1 BASIS FUNCTIONS

Choosing a basis set is an important part of molecular energy calculations. Generally, the chosen basis functions are atomic orbitals (AOs) centered on the two atoms of a diatomic molecule. Traditionally, each of the AOs are represented as a linear combination of Slater Type Orbitals (STOs). An STO centered on an atom has the form

$$N r_a^{n-1} e^{-\zeta r_a} Y_l^m(\theta_{\mathrm{a}}, \phi_{\mathrm{a}}), \tag{37}$$

where n, l and m are quantum numbers, Y are spherical harmonics, N is the normalization constant, r_{a} is the distance to the nucleus a and ζ is the orbital exponent which contains all possible values that form a complete set. A molecular orbital ϕ_i (MO) is expressed as a sum of STO (χ_r) basis functions ($\phi_i = \sum_r c_{ri}\chi_r$).

A minimal basis set consists of one STO for each inner-shell and valence-shell. As an example, for NH, a minimal basis set contains $1s$, $2s$, $2p_x$, $2p_y$, $2p_z$ AOs for N atom and $1s$ AO for H atom (total 6 basis functions). Therefore, this set consists of two s-type STOs and one p-type STO for N and one s-type STO for H; such a set is denoted by $(2s1p/1s)$. For a double-zeta (DZ) basis set, a minimal set is replaced by two STOs with different ζs and for a triple-zeta (TZ) basis set three STOs were used. For valence double-zeta (VDZ) basis set one STO is used for each core-shell AO and two STOs for each valence AO. For valence triple-zeta (TDZ) basis set one STO is used for each core-shell AO and three STOs for each valence AO. Since AOs are polarized around their centers of charges, by adding additional basis-functions can improve the representation of AOs. As an example, double-zeta plus polarization set (DZ + P or DZP) typically includes a double-zeta set that contains five $3d$ functions

for each "second row" atom and a set of three $2p$ functions ($2p_x$, $2p_y$, $2p_z$) for each hydrogen atom.

In order to make calculations faster, Gaussian type functions (GTF) are used instead of STOs for the atomic orbitals in an LCAO wave fucntion. A Cartesian Gaussian centered on an atom is written as

$$g_{ijk} = N x_b^i y_b^j z_b^k e^{-\alpha r_b^2}, \tag{38}$$

where i, j and k are nonnegative integers, α is a positive orbital exponent, $x_b^i y_b^j z_b^k$ are Cartesian coordinates with the origin at the nucleus b of the two nuclei (a and b) in the diatomic molecule, N is the normalization constant and r_b is the distance to nucleus b. When $i + j + k = 0$ or $i = 0, j = 0, k = 0$, the GTF is called s-type orbital, when $i + j + k = 1$, the GTF is a p-type Gaussian, when $i + j + k = 2$, the GTF is a d-type Gaussian and when $i + j + k = 3$, the GTF is a f-type Gaussian etc.

Instead of using individual Gaussian basis functions, using more than one Gaussian function to represent basis functions gives more accurate representation ($\chi_r = \sum_u d_{ur} g_u$). Here, g_u's are normalized Cartesian Gaussians centered on the same atom and have same i, j, k values, but different α's. χ_r's are called contracted Gaussian-type functions (CGTF) and g_u's are called primitive Gaussians. d_u's are the contracted coefficients that are held constant during calculations.

TABLE 2: The cc basis sets

cc-pVDZ	cc-pVTZ	cc-pVQZ	cc-pV5Z	cc-pV6Z
$[3s2p1d]$	$[4s3p2d1f]$	$[5s4p3d2f1g]$	$[6s5p4d3f2g1h]$	$[7s6p5d4f3g2h1i]$
14	30	55	91	140

Most often, CGFT cc-pVnZ basis sets (n = 2, 3, 4, 5, 6) are used for calculation methods (such as Configuration Interaction) that include electron correlation. Here, cc stands for $correlation - consistent$ and pV for $polarized\ valence$. The CGFTs present in the cc basis sets are given in the Table 2 for second row atoms. In cc basis sets the number of d functions vary from set to set. Generally, cc basis sets use five d functions, seven f functions etc. The last row of the Table 2 represents the number of basis functions for a second row atom. Similarly for the H atom, cc-pVDZ set is

$[2s1p]$ or $(6s3p)$, cc-pVTZ set is $[3s2p1d]$ and cc-pVTZ set is $[4s3p2d1f]$ etc. Here [] means a STO is replaced with a CGFT containing three primitive Gaussians.

The diffuse (functions with very small orbital exponent) primitive nonpolarization and polarization functions (2 extra functions each) can be added to the cc basis sets as well and they are called aug-cc basis sets. As an example, second row aug-cc-pVTZ basis function is $[6s5p4d3f]$.

3.11.2 THE HARTREE-FOCK SELF-CONSISTENT-FIELD METHOD

Although the exact wavefunction of the hydrogen atom is known, calculating the exact wavefuntion of multi-electron atoms and molecules is difficult because of the inter-electronic repulsion energy terms in the Hamiltonians. The Hartree-Fock procedure is a method that is used as the initial step to find a wavefuntion for non-hydrogen atoms and for molecules.

3.11.2.1 The Hartree-product wavefunction

Usually, as the initial step of molecular Hartree-Fock calculations, a Hamiltonian is introduced ignoring inter-electronic repulsion energy terms. This is called the Hartree-product Hamiltonian and it is designated by

$$\hat{H} = \sum_{i=1}^{N} \hat{h}_i, \tag{39}$$

where N is the total number of electrons and h_i is the one-electron Hamiltonian.

The one-electron Hamiltonian is

$$\hat{h_i} = -\frac{\hbar^2}{2m_e}\nabla_i^2 - \sum_{k=1}^{M} \frac{Z_k e^2}{4\pi\epsilon_0 r_{ik}}, \tag{40}$$

where the first term represents the kinetic energy of the electron and the second term represents the Coulomb attraction energy (between nuclei and the electron). Here, m_e is the mass of the electron, e is the charge of the electron, M is the total number of nuclei, $Z_k(e)$ is the nuclear charge of the nucleus k and r_{ik} is the distance between the electron i and the nucleus k.

Since the inter-electron repulsion energy terms are not included in the Hartree-Hamiltonian, its many-electron wavefunction can be constructed as a product of one-electron eigenfunctions.

This many-electron wavefunction is called the "Hartree-product wavefunction" and it is written as

$$\Psi_{HP} = \psi_1\psi_1\psi_2.....\psi_N. \tag{41}$$

Since the Hamiltonian operator in Equation 40 is separable, the total energy of the many-electron wavefuntion is the sum of all one-electron energy eigenvalues.

3.11.2.2 Hartree Self-Consistent-Field (SCF) Method

Hartree individual electron operator $h_i{}'$ can be written as

$$h_i{}' = -\frac{\hbar^2}{2m_e}\nabla_i^2 - \sum_{k=1}^{M}\frac{Z_k e^2}{4\pi\epsilon_0 r_{ik}} + V_i\{j\} \tag{42}$$

and the energy eigenvalues (ϵ_i) for each $h_i{}'$ can be written as

$$h_i{}'\psi_i{}' = \epsilon_i{}'\psi_i{}', \tag{43}$$

where $V_i\{j\}$ is

$$V_i\{j\} = \sum_{j\neq 1}\frac{e^2}{4\pi\epsilon_0}\int\frac{\rho_j}{r_{ik}}dr \tag{44}$$

and ρ_j is the charge (probability) density associated with the electron j. The nuclei in the Equation 42 are treated as point charges and the electrons are treated as wavefunctions with spread out charges, where

$$\rho_j = -e \mid \psi_i \mid^2 . \tag{45}$$

However, in order to calculate this average potential $V_i\{j\}$, the individual ψ_is should be determined. In 1928, as a solution to this problem, Hartree proposed an iterative "self-consistent field" (SCF) method. As the first step of the SCF process, ψ_i is guessed for each electron to calculate the potential energy $V_i\{j\}$. Afterwards, a new set of eigenfunctions are calculated using the new potential energy $V_i\{j\}$ for each electron, presumably different from the initially guessed eigenfunctions. These

newly obtained eigenfunctions are used again to calculate energy eigenvalues for each electron until the difference between the previous and the current energy eigenvalues falls below some threshold criterion. This is called the Hartree self-consistent-field method.

3.11.2.3 Hartree-Fock (HF) calculations

Hartree-product Hamiltonian does not include internuclear repulsion and it has to be corrected. In HF calculations, instead of spatial-orbitals, spin-orbitals (a product of spatial orbital (ψ_i) and a spin function (either α or β)) are used for individual electrons and the molecular Hartree-Fock wavefunction is written as an anti-symmetrized product of spin-orbitals to account for the Pauli principle. The Hartree-Fock energy is given by

$$E_{HF} = \langle D|\hat{H}_{el} + V_{NN}|D\rangle. \tag{46}$$

where D is the Slater determinant Hartree-Fock wavefunction. $\hat{H}_{el}$ is the electronic Hamiltonian and V_{NN} is the internuclear repulsion defined in the Equation 22.

3.12 ELECTRON CORRELATION

Hatree-Fock calculations only take the interaction between electrons in an average way. In order to obtain more accurate wavefunctions the instantaneous interactions between electrons must be taken into account. The motion of electrons in the vicinity of nuclei is correlated and the energy calculated by using electron correlated wavefunctions is called the correlation energy. The relationship between the exact energy (E), Hartree-Fock energy and the correlation energy (E_{corr}) in a system is

$$E_{corr} = E - E_{HF}. \tag{47}$$

Actually, since Hartree-Fock wavefunction satisfies the antisymmetry principle under exchange of electrons, it does include some instantaneous electron correlation.

However, there are better ways to include instantaneous electron correlation in energy calculations. One of the most prominent methods of including electron correlation is configuration interaction (CI). Hartree-Fock wavefunction is a Slater determinant that is constructed from one-electron MOs. In CI, multiple determinants

from excited electron configurations were included with the Hartree-Fock Slater determinant as a linear combination and optimized the coefficients of those Slater determinants to find the best representation of the wavefunctions and energies. This electron correlation is called "dynamical correlation" as it refers to the electron-electron dynamical interaction. There are several different methods that are used to include excited electron configurations as a Slater determinant in order to improve electron correlation. MCSCF (Multi-configuration Self Consistent Field), MRCI (Multi-reference Configuration Interaction), CASSCF (Complete Active Space Self Consistent Field) and MRSD-CI (Multi-reference Single and Double Configuration Interaction) are some popular configuration interaction methods that are being used to include electron correlation in molecular and atomic energy calculations.

3.13 FOURIER TRANSFORM SPECTROSCOPY

Isobutane spectra were recorded (Chapter 5) using a Bruker IFS 125HR Fourier transform spectrometer (FTS). The essential part of the Fourier transform spectrometer is the interferometer. Even though the interferometer in the Bruker IFS 125HR has a complex setup, the basis of it is an idealized Michelson interferometer which is shown in the Figure 13.

As shown in the Figure 13 a beam of light emitted from a light source (laser, glow bar) is directed at the beam splitter (the device that splits the light beam ideally into two); it allows one half passes through the splitter (transmitted beam) and the other half reflects (reflected beam). The reflected part of the beam travels a distance L_1 to the mirror M1 and reflects back to the beam splitter. Then the total distance (optical path length) traveled by the reflected beam becomes $2L_1$. The transmitted beam also travels a distance $2L_2$, but the path length of the transmitted beam is not fixed and can vary (back and forth) by a maximum distance of X. Therefore, the total path length of the transmitted beam is accordingly $2(L_2+x)$ and when the two beams recombine on the beam splitter, the path length difference between the two beams become $2x$ ($0 \leq x \leq X$). Since these two beams are spatially coherent they will interfere when they recombine at the beam splitter. The interfered beam will be captured by the detector once the recombined interfered beam leaves the interferometer. The intensity ($I(x)$) of the recombined beam is the signal that receives by the detector as a function of moving mirror displacement which is called the interferogram. The interferometer produces constructive or destructive interference

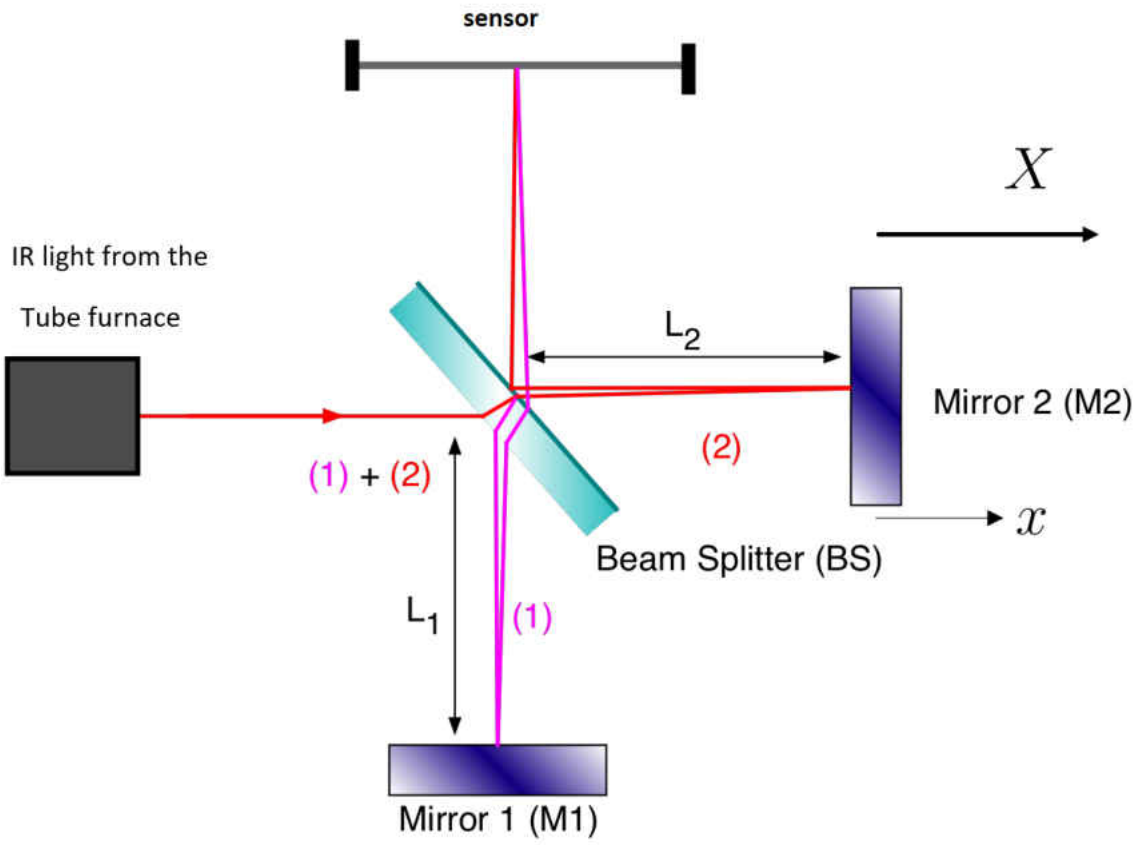

FIG. 13: Schematic of a Michelson interferometer

depending on the path length difference between the two light beams.

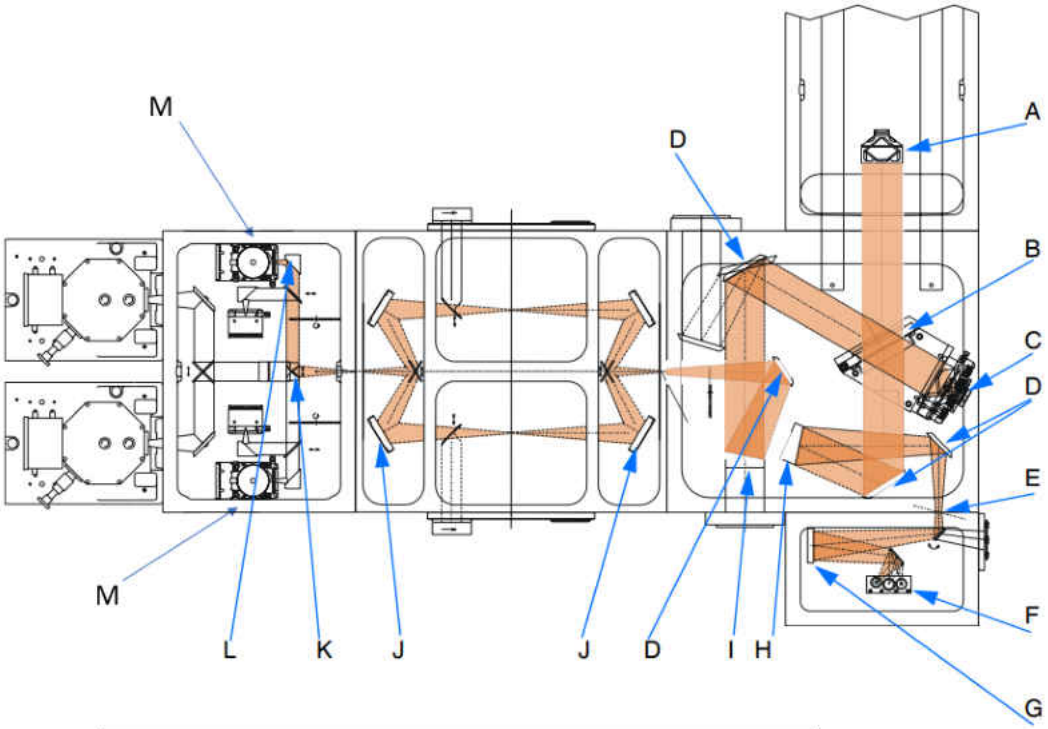

	Definition
A	Scanner with movable retroflecting mirror
B	Beam splitter
C	Fixed retroflecting mirror
D	Folding mirror
E	Input aperture (field stop)
F	Sources
G	Spherical mirror
H	Collimating parabolic mirror
I	Focusing parabolic mirror
J	Toroidal mirror
K	Collimating parabolic mirror
L	Focusing parabolic mirror
M	Detector

FIG. 14: Optical path of the Bruker IFS 125HR Fourier transform spectrometer (Bruker 2016)

The complete dependence of the intensity ($I(x)$) captured by the detector of a monochromatic light beam is given by

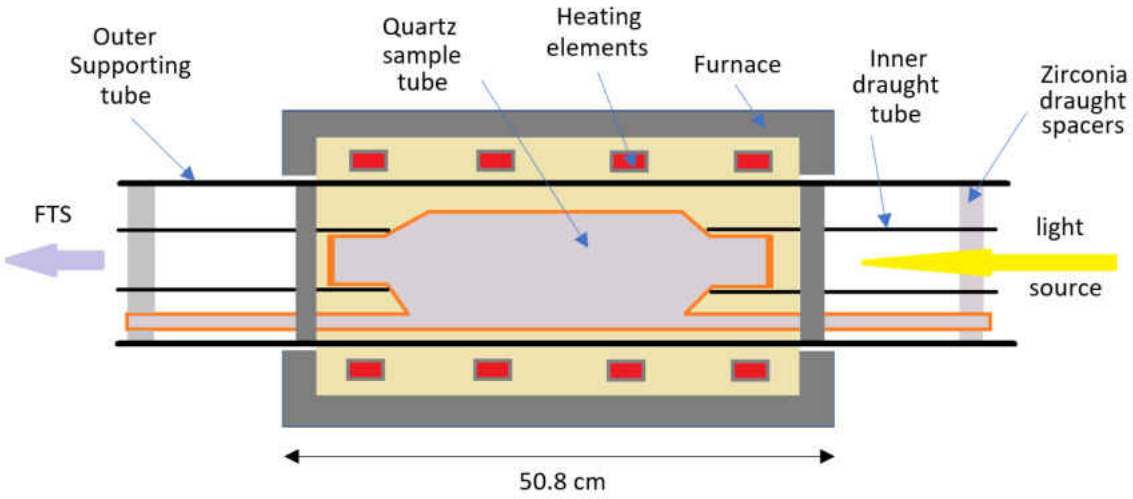

FIG. 15: Schematic of the tube furnace

$$I(x) = s(\tilde{\nu}) \times cos(2\pi\tilde{\nu}X) \tag{48}$$

where $\tilde{\nu}$ is $(1/\lambda)$ is the wavenumber and $s(\tilde{\nu})$ is the intensity of a coherent (monochromatic) line located at the wavenumber $\tilde{\nu}$.

Usually, the light beam entering the spectrometer is incoherent. Therefore, the Equation 48 must be modified accordingly. The intensity of an incoherent light beam is given by

$$I'(x) = \int_{-\infty}^{\infty} S'(\tilde{\nu}') \times cos(2\pi\tilde{\nu}'x)\ d\tilde{\nu}' \tag{49}$$

where

$$S'(\tilde{\nu}) = \int_{-\infty}^{\infty} I'(x') \times cos(2\pi\tilde{\nu}x')\ dx' \tag{50}$$

is the spectral power density,

The interferometer is consisted of N discrete sample points. A mathematical technique called discrete Fourier transformation is used to convert this interferometer to a spectrum. Since the movable mirror M2 can move only a finite distance (X) the spectrum can be obtained only with a limited resolution.

The optical path of the Bruker IFS 125HR Fourier transform spectrometer is shown in the Figure 14. Instead of a simple Michelson interferometer with two mirrors, one fixed (C) and one movable (A), Bruker IFS 125HR has several mirrors that direct the infrared light coming from the tube furnace (Figure 15) that enters though the aperture (E) to the detector (M). The maximum optical path length (MOPD) of the Bruker IFS 125HR Fourier transform spectrometer is 5 m and the corresponding maximum instrumental resolution (1/MOPD) is 0.002 cm^{-1}.

3.14 BEER-LAMBERT LAW

The Beer-Lambert law gives the relationship of the attenuation of light and the properties of a material of which the light is traveling. As shown in the Figure 16 a flux of photons ($F_0 = I_0/h\nu$) travels through a two level (the upper state with population N_1 and the lower/ground state with population N_0) system with dimensions 1 m $\times$ 1 m $\times$ l m that can be absorbed and induced stimulated emission. The intensity of the radiation after traveling distance l through the system is I.

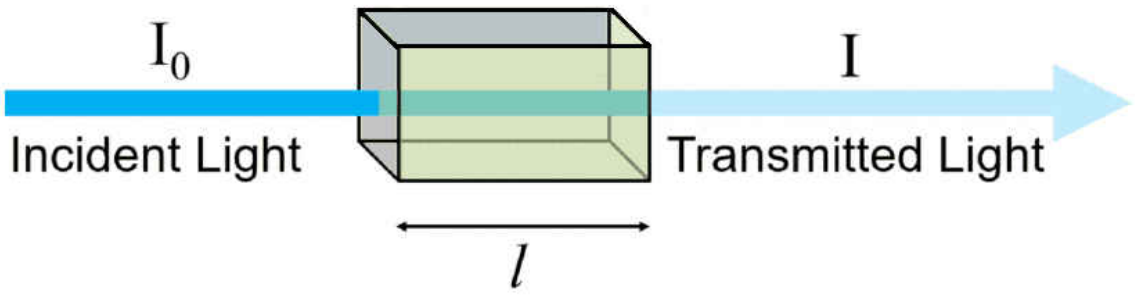

FIG. 16: A two level-system with dimensions 1 m $\times$ 1 m $\times$ l m with molecules

The Beer-Lambert law can be written as

$$I = I_0 e^{-\sigma(N_0 - N_1)l}, \tag{51}$$

where σ is the absorption cross section. The physical interpretation of the absorption cross section is the "effective area" of the molecule that the flux of photons goes through. Also the absorption cross section can be defined as

$$\sigma = \frac{\lambda^2}{8\pi} A_{1\rightarrow 0} g(\nu - \nu_{10}), \tag{52}$$

where $A_{1\rightarrow 0}$ is the Einstein A coefficient and $g(\nu\text{- }\nu_{10})$ is the lineshape function.

3.15 LINE SHAPE FUNCTIONS

In a real spectrum of a molecule, absorption features consist of characteristic line shapes. These line shape functions can be categorized into two groups: homogeneous and inhomogeneous. When molecules are in a high pressure system, it is considered that the system has an identical pressure-broadened lineshape for a particular transition. Pressure broadening in a transition belongs to homogeneous broadening. On the other hand, gas phase Doppler broadening of molecular velocities due to Maxwell-Boltzmann distribution is an example for inhomogeneous broadening, where different molecular velocities give the incident radiation a frequency shift $\nu = (1 \pm \nu/\mathrm{c})\nu_0$ in the molecular frame of reference. In general, homogeneous line shape functions represent by Lorentzian functions and inhomogeneous line shape functions by Gaussian functions. The convolution of a Lorentzian and Gaussian function is called a Voigt line shape function.

CHAPTER 4

A NEW LINELIST FOR THE $A^3\Pi$ - $X^3\Sigma^-$ TRANSITION OF THE NH FREE RADICAL

The results and the majority of the material presented in this chapter are published in the Journal of Quantitative Spectroscopy & Radiative Transfer (Fernando et al. [36]). The co-authors of this publication are: P. Bernath (Old Dominion University), J. Hodges (Old Dominion University) and T. Masseron (Universidad de La Laguna). T. Masseron calculated the synthetic spectra of the solar photosphere and the metal poor star HD196944 using the linelist prepared by us to validate our results. Figures 20 and 21 were also prepared by him. A computer program was written by J. Hodges to convert Hund's case (b) transition dipole moment matrix elements to Hund's case (a) elements. P. Bernath is the advisor of this project. As the first author of this publication, carrying out computational calculations to prepare the linelist, preparation of figures (except the figures prepared by T. Masseron) and writing the text were done by me. This work is original and has not published anywhere prior to the publication in the Journal of Quantitative Spectroscopy & Radiative Transfer.

4.1 INTRODUCTION

The NH radical plays an important role in astrophysics. The bands of the $A^3\Pi - X^3\Sigma^-$ transition were first detected in a laboratory spectrum in 1893 [32]. The first astronomical observation of the NH $A - X$ system was made in the spectrum of the Sun [40]. In 1940, the $A - X$ system of NH was detected in the Comet Cunningham [147]. The $A^3\Pi - X^3\Sigma^-$ transition of NH was first recorded in the interstellar medium in 1991, towards the stars HD 27778 and HD 24398 and again in 1997 towards the star HD 149757 [100, 25]. In 2009, interstellar NH abundances were calculated using the lines of the $A - X$ system recorded towards the stars HD 149757, HD 170740, HD 154368 and HD 169454 [162].

NH is also frequently detected in the infrared spectra of cool stars. The infrared vibration-rotation lines of NH in oxygen-rich M giant stars, including α Orionis, were

analyzed in order to obtain nitrogen abundances [78, 5]. In 1986, nitrogen abundances for six additional stars were calculated using the observed infrared spectra [138].

In stellar atmospheres, although the formation of N-bearing molecules is strongly dominated by N_2 [151], molecular transitions are an excellent indicator of N abundances. Despite its dependence on carbon abundance, the CN molecule in the red and near infrared spectral regions is preferentially used by stellar spectroscopists because a higher stellar signal is obtained.

With the advent of a new generation of spectrographs such as UVES mounted on the VLT [28], the observation of the short wavelength region of the spectrum has become accessible. Indeed, the $A-X$ transition of NH has been observed in stars and notably in metal-poor stars [141, 143]. Spite et al. [143] noticed a systematic discrepancy in the N abundance derived from NH compared to the value derived from CN. They suspected that the NH $A-X$ linelist needed revision, which we provide in this chapter.

The assignment of the $0-0$ and $1-1$ bands of the $A-X$ system was carried out in the 1930s from emission spectra by Funke [42]. In 1959, the $0-0$ and $1-0$ bands were recorded in absorption [29] and in 1966 and 1970 several additional bands were analyzed [105, 93]. In 1986, the $A-X$ system of NH was measured with a precision of ± 0.0002 cm^{-1} for the $0-0$, $1-1$, $2-2$, $0-1$, $1-2$, $1-0$ and $2-1$ bands [16]. These measurements improved on the previously available line positions by more than two orders of magnitude. The vibration-rotation lines in the infrared region were re-analyzed using solar spectra as well as IR laboratory spectra [123, 122].

The $A^3\Pi - X^3\Sigma^-$ system recorded by Brazier et al. [16] used a copper hollow cathode discharge of helium with added nitrogen and hydrogen. The $A-X$ spectrum was recorded with the Fourier transform spectrometer associated with the McMath-Pierce Solar Telescope of the National Solar Observatory at Kitt Peak [16].

4.2 METHOD

4.2.1 EXPERIMENTAL DATA

The spectroscopic constants for $A^3\Pi$ and $X^3\Sigma^-$ states were obtained from Ram and Bernath [122] based on Brazier et al. [16] for the $A-X$ transition and Ram et al. [123] for the infrared vibration-rotation and pure rotation lines. The X state constants from Ram and Bernath [122] were also used by Brooke et al. [19] for the

vibration-rotation line intensity analysis. The Brazier et al. $A-X$ spectrum [16] will be used for comparison with our new linelist. Linelist is a compilation of positions (transition frequencies), line intensities or Einstein A coefficients, relevant quantum numbers of the upper and the lower states and the lower state energies of energy transitions. Linelists are used to recognize molecules and atoms in observed spectra and predict molecular concentrations in atmospheric models. ^{15}NH was not included in this analysis because it was not detected in the spectrum of Brazier et al. [16].

4.2.2 TRANSITION DIPOLE MOMENT FUNCTION CALCULATIONS

`MOLPRO 2012` [161] was used to perform *ab initio* calculations (solve non-relativistic Schrödinger equation) of the transition dipole moment function of the $A^3\Pi - X^3\Sigma^-$ transition. To calculate the transition moment, the multireference configuration interaction (MRCI) method was used with the aug-cc-pwCV5Z basis set. The wavefunctions utilized for the MRCI calculations were obtained from state-averaged (same set of molecular orbitals is used for both the states in a given spatial and spin symmetry) CASSCF calculations with the $A^3\Pi$ and $X^3\Sigma^-$ states having equal weights. All the electrons were included in the correlation treatment. The active space included the 2-5a_1, 1-2b_1, 1-2b_2 and 1a_2 orbitals in the C_{2v} point symmetry group used by `MOLPRO`. The TDMF (transition dipole moment function) points were calculated for internuclear distances between 0.7 Å to 2 Å in steps of 0.02 Å as expectation values.

4.2.3 POTENTIAL FUNCTIONS

The potential energy curves of the $A^3\Pi$ and $X^3\Sigma^-$ states were calculated employing Le Roy's `RKR1` program [80]. The `RKR1` program produces classical turning points of the potential energy curves using the first order semi-classical Rydberg-Klein-Rees procedure. The `RKR1` program requires vibrational and rotational constants as the input in order to perform the calculations. The molecular constants required for the $X^3\Sigma^-$ state were obtained from [123] and for the $A^3\Pi$ state from [16] (Table 3). The dissociation energy for the ground state (D_0=27, 409 ±13 cm^{-1}) was obtained using the enthalpy of formation of N, H and NH at 0 K from the Active Thermochemical Tables [131] and for the excited state using a thermochemical cycle (D_0=16, 874 ±13 cm^{-1}). The error in the dissociation energy was calculated by propagation of the errors in the enthalpies given in the tables.

TABLE 3: Equilibrium constants for $A^3\Pi$ and $X^3\Sigma^-$ States of NH (cm^{-1})

Constant	$X^3\Sigma^-$	$A^3\Pi$
D_e	29,030	18,465.5
T_e	-	29,790.5
ω_e	3282.220(15)	3231.70
$\omega_e x_e$	78.513(15)	98.48
$\omega_e y_e$	0.1341(61)	-
$\omega_e z_e$	-0.0066(11)	-
B_e	16.667704(29)	16.681963(8)
α_e	0.649670(91)	0.712880(35)
γ_e	-0.001674(71)	-0.016160
δ_e	-0.000067(25)	-
ϵ_e	-0.0000633(24)	-

4.2.4 TRANSITION DIPOLE MOMENT MATRIX ELEMENTS AND THE "HERMAN-WALLIS EFFECT"

The calculated potential energy curves (Figure 17) were used as input for Le Roy's `LEVEL` program [81]. The `LEVEL` program generates vibrational wavefunctions by solving the 1-D Schrödinger equation and then uses them with a specified transition dipole moment function (TDMF) to calculate transition dipole moment matrix elements (TDMMEs). `LEVEL` does not include electron spin in its calculations which corresponds to Hund's case (b). In `LEVEL` the total angular momentum quantum number J ($\overrightarrow{J} = \overrightarrow{N} + \overrightarrow{S}$) is actually the quantum number N (total angular momentum except electron spin) [81]. The matrix elements provided by `LEVEL` include the rotational dependence that originates from the J-dependent centrifugal term in the 1-D vibrational Schrödinger equation (i.e. the vibrational wavefunctions depend on J). These TDMMEs are transformed into Hund's case (a) using the method of [19] and then input into Western's `PGOPHER` [163] to calculate the linelist.

When a diatomic molecule is rotating, it increases its bond length as a result of the centrifugal force [55]. Therefore the vibrational wavefunctions of the molecule change due to rotation and this affects the molecular properties. In particular, infrared line

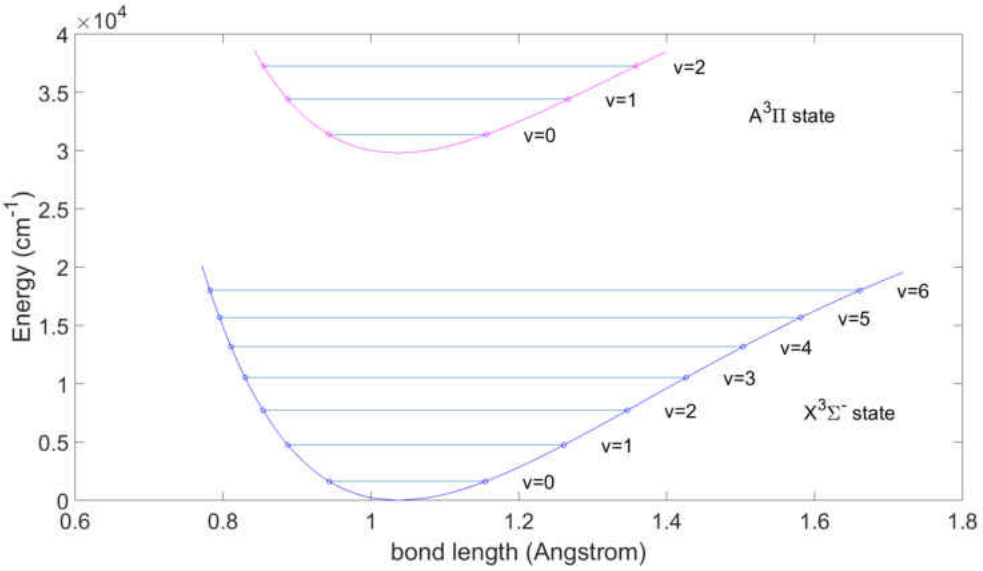

FIG. 17: Calculated RKR potential curves of the $A^3\Pi$ and $X^3\Sigma^-$ states for NH.

intensities can no longer be separated into a vibrational part times a Hönl-London factor (nuclear angular momentum dependence)[10]. This mechanical effect of the vibration-rotation interaction on line intensities is called the "Herman-Wallis effect" [55]. Einstein A calculations were done using `PGOPHER` including the J-dependent TDMMEs. `PGOPHER` calculates line intensities using the equations [10]:

$$A_{\eta' J' \longrightarrow \eta J} = \frac{16\pi^3 \nu^3 S_{\eta' J' \eta J}}{3\epsilon_0 h c^3 (2J'+1)} \quad \text{(SI Units)} \tag{53}$$

$$A_{\eta' J' \longrightarrow \eta J} = 3.13618932 \times 10^{-7} \frac{\widetilde{\nu}^3 S_{\eta' J' \eta J}}{(2J'+1)}. \tag{54}$$

Line strength $S_{\eta' J' \eta J}$ in the equation (54) is in debye squared, $A_{\eta' J' \longrightarrow \eta J}$ is in s^{-1} and $\widetilde{\nu}$ is in cm^{-1}.

All of the bands for $v' = 0-2$ and $v'' = 0-6$ are included for $\Delta v \leq 4$; $0-5$, $0-6$, $1-6$ bands were not included as the Einstein A values are probably not reliable because of numerical problems in the `LEVEL` calculations. For each band, J was limited to about 5 J values beyond the highest observed value. Full linelist calculation method is shown in the Figure 18.

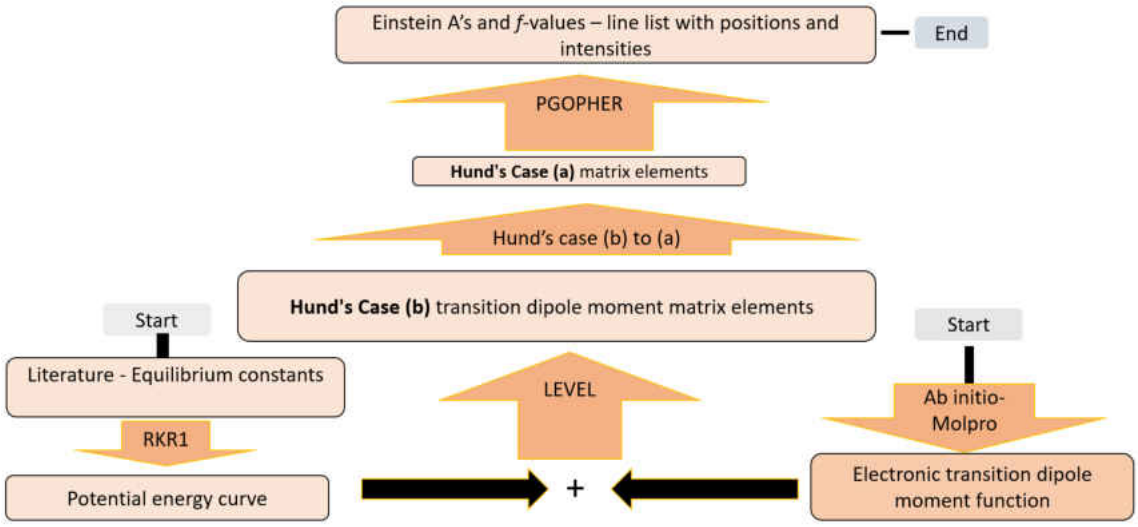

FIG. 18: Full calculation method.

4.3 RESULTS AND DISCUSSION

4.3.1 TRANSITION DIPOLE MOMENT FUNCTION

The transition dipole moment function (TDMF) calculated in this study was compared with the TDMF available in the literature calculated by Owono et al. [113]. Owono et al. [113] carried out the calculations by using the aVTZ basis set and the orbitals needed for the configuration interaction (CI) were obtained by the CASSCF method. The CASSCF wavefunctions were then used for the MRSD-CI (multireference single and double excitation configuration interaction) routine to include electron correlation [113]. Our calculations used a larger basis set (aug-cc-pwCV5Z) and more extensive electron correlation than Owono et al. [113]. Our transition dipole moment function deviates from that of Owono et al. [113] for values greater than 1.5 Å, but in general, our TDMF agrees with the Owono et al. [113] TDMF (Figure 19). (The polarity of the Owono et al. [113] TDMF was changed in order to compare with our TDMF.)

Our TDMF was also compared with the TDMF calculated by Song et al. [142] and they are in good agreement. (Since Song et al. [142] does not provide numerical points for the TDMF, the comparison was done with the published figure.)

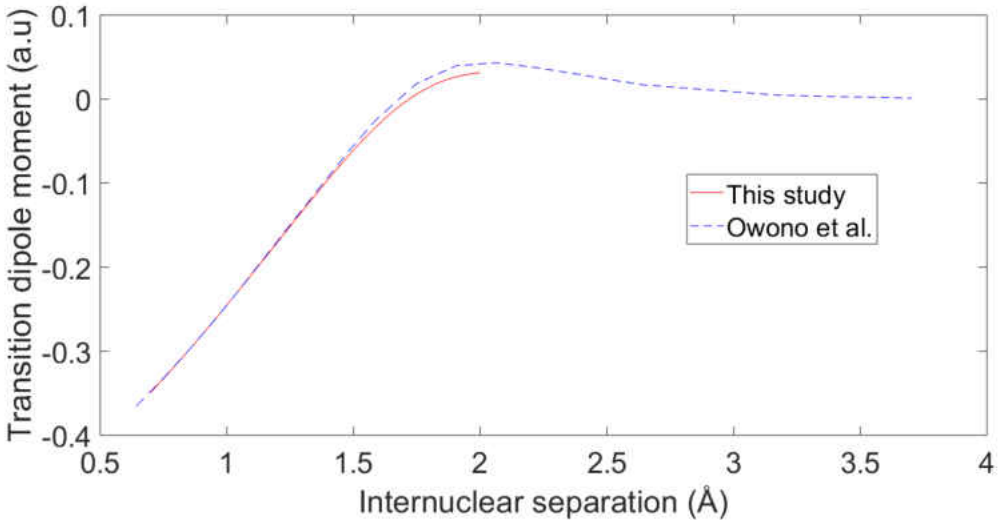

FIG. 19: Calculated transition dipole moment function for NH $A^3\Pi - X^3\Sigma^-$ compared with the TDMF calculated by Owono et al. [113].

TABLE 4: Comparison of the radiative lifetimes of the vibrational levels of the A state.

v'	τ (ns)	Ref.
0	388	This study
	449	[142] (Calc)
	453±10	[47] (Exp)
	440±15	[33] (Exp)
	390±40	[54] (Exp)
1	436	This study
	484	[142] (Calc)
	488±10	[47] (Exp)
	414±6	[140] (Exp)
	390±40	[54] (Exp)
	420±35	[33] (Exp)
2	511	This study
	520	[142] (Calc)

TABLE 5: Einstein A coefficient comparison.

Band $(A-X)$	$A_{v'v''}$ $(\times 10^7 s^{-1})$	Ref.
0-0	0.254	This study
	0.260	[113] (Calc)
	0.2522	[170] (Calc)
	0.226	[33] (Calc)
1-0	0.005870	This study
	0.005781	[113] (Calc)
	0.006425	[170] (Calc)
	0.007484	[136] (Calc)
1-1	0.218	This study
	0.226	[113] (Calc)
	0.2169	[170] (Calc)
	0.291	[83] (Calc)
2-0	0.00003	This study
	0.0001	[113] (Calc)
2-1	0.0139	This study
	0.0116	[113] (Calc)
2-2	0.181	This study
	0.193	[113] (Calc)
	0.220	[139] (Calc)

TABLE 6: A portion of the linelist.

v'	J'	N'	Sym'	v''	J''	N''	Sym''	Position (cm^{-1})	f-value	$A_{v'v''}$ (s^{-1})	Line
0	0	1	e	0	1	0	e	29826.9444	0.0009454	1683060	$^{r}P_{31}(1)$
2	11	11	f	2	10	10	f	29826.6657	0.0016010	867477	$^{r}R_{2}(10)$
1	5	5	f	1	5	4	e	29826.1839	0.0003161	187576	$^{r}Q_{21}(5)$
1	5	5	f	1	4	4	f	29825.0871	0.0020780	1008750	$^{r}R_{2}(4)$
2	12	11	e	2	11	10	e	29822.8867	0.0016190	883903	$^{r}R_{1}(11)$
2	3	4	e	2	2	1	e	29816.1540	0.0000003	137	$^{t}R_{31}(2)$
1	6	5	e	1	5	4	e	29814.7189	0.0023200	1163823	$^{r}R_{1}(5)$
2	4	5	f	2	4	3	e	29811.6183	0.0000045	2662	$^{s}Q_{31}(4)$
2	4	5	f	2	3	3	f	29810.6036	0.0000435	20045	$^{s}R_{32}(3)$
2	9	10	e	2	10	9	e	29809.9762	0.0000005	295	$^{r}P_{31}(10)$
0	3	2	e	0	2	1	e	29809.8176	0.0034430	1457625	$^{r}R_{1}(2)$
2	9	10	e	2	8	9	e	29809.1619	0.0016770	889531	$^{r}R_{3}(8)$
2	9	10	e	2	9	9	f	29808.6222	0.0000695	41212	$^{r}Q_{32}(9)$
0	1	1	f	0	1	0	e	29807.2843	0.0027230	1613856	$^{r}Q_{21}(1)$
2	10	10	f	2	10	9	e	29806.4612	0.0000719	42585	$^{r}Q_{21}(10)$
1	3	4	e	1	4	3	e	29805.1718	0.0000176	13388	$^{r}P_{31}(4)$
2	10	10	f	2	9	9	f	29805.1072	0.0016290	873561	$^{r}R_{2}(9)$
1	3	4	e	1	2	3	e	29805.0871	0.0022630	958018	$^{r}R_{3}(2)$
1	3	4	e	1	3	3	f	29804.1443	0.0004592	272098	$^{r}Q_{32}(3)$

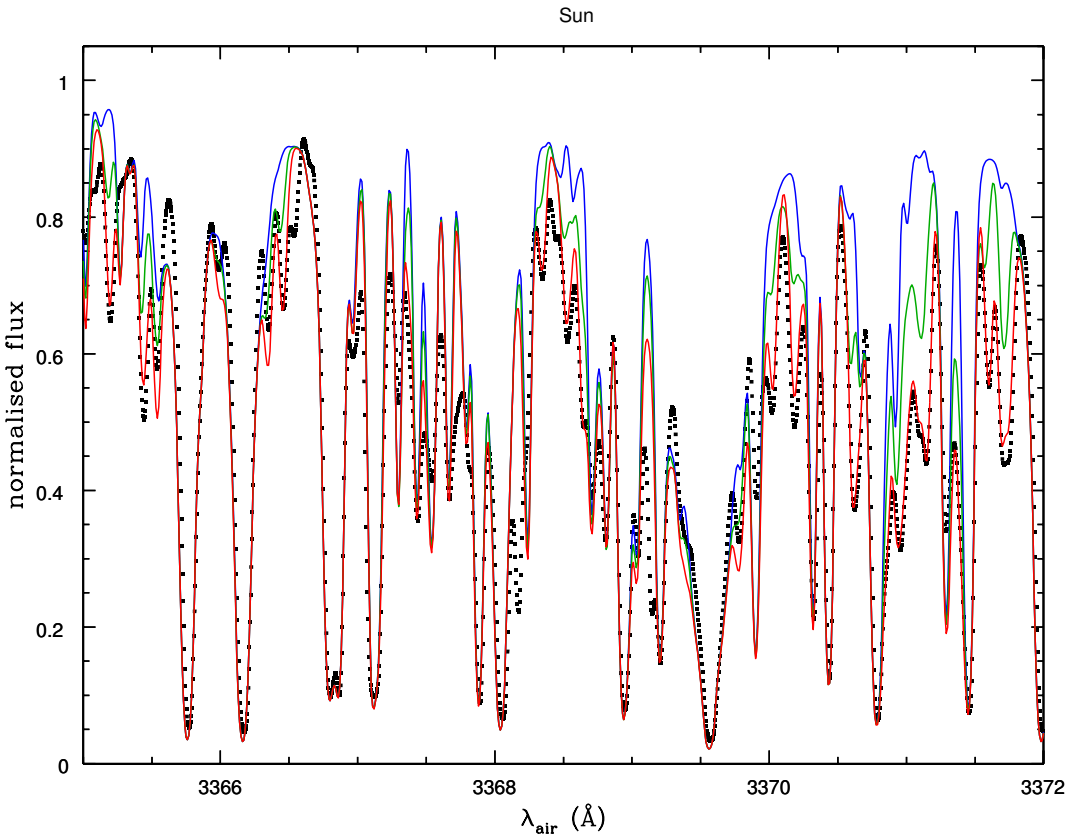

FIG. 20: Comparison between the observed spectrum of the Sun (black dotted line) and their respective syntheses with (red) and without (blue) the linelist presented in this work as well as the former linelist from Kurucz (`http://kurucz.harvard.edu/molecules/`) (green).

4.3.2 EINSTEIN A COEFFICIENTS AND LIFETIMES

The calculated lifetimes and Einstein A coefficients in this study were compared with experimental and theoretical values available in the literature as listed in Tables 4 and 5. A large Herman-Wallis effect was observed in the ground state as calculated by Brooke et al. [19]. In order to estimate the Herman-Wallis effect in the $A - X$ transition, two sets of line strengths were calculated with and without including the Herman-Wallis effect. The line strengths without the Herman-Wallis effect were calculated with `PGOPHER` by using a single band strength (P(2) from the output of `LEVEL`) and the line strengths with the Herman-Wallis effect were calculated by using the J-dependent TDMMEs.

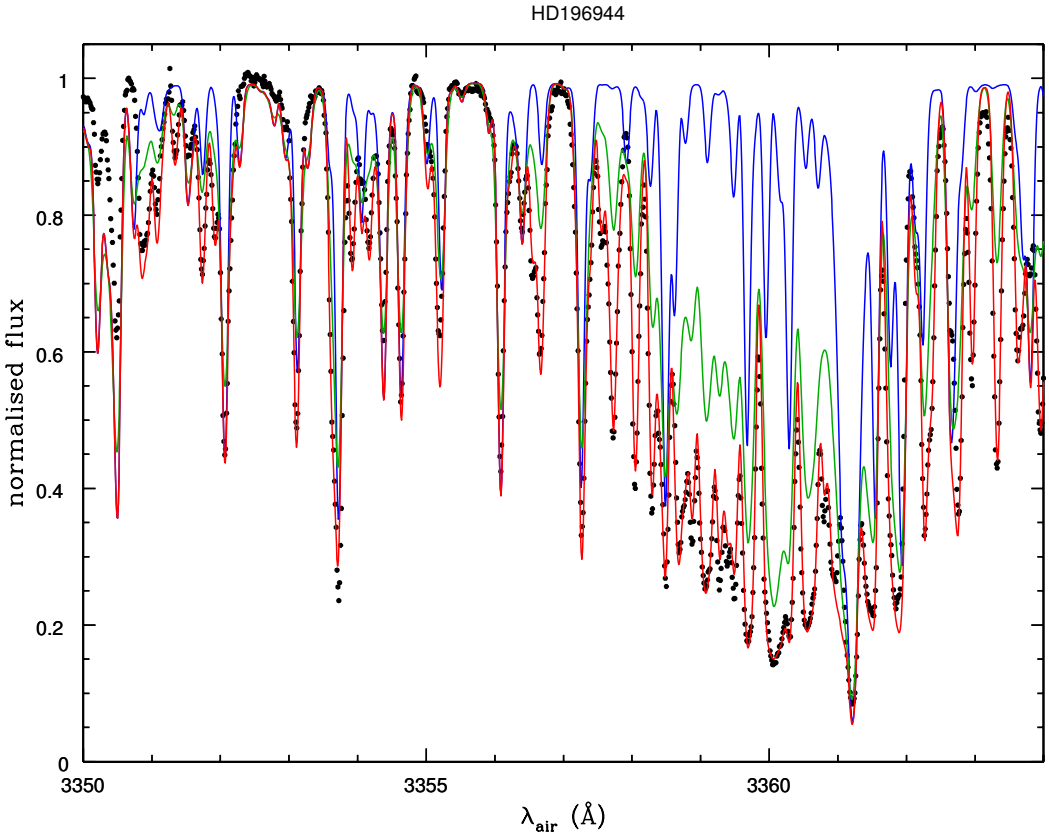

FIG. 21: Comparison between the observed stellar spectrum of the metal-poor star HD196944 (black dotted line) and their respective syntheses with (red) and without (blue) the linelist presented in this work as well as the former linelist from Kurucz (http://kurucz.harvard.edu/molecules/) (green).

Since the experimental emission spectrum [16] does not have a well defined temperature, our line strengths cannot be compared directly with the observations. For comparison purposes, the ratio of ${}^{r}\mathrm{R}_3(J'')$ and ${}^{p}\mathrm{P}_3(J''+2)$ lines of the same upper state J' values were calculated, in order to cancel the effect of the excited state population in line intensities. These two sets of ratios were then compared with each other and then also with the ratios calculated from the experimental spectrum of Brazier et al. [16].

The ${}^{r}\mathrm{R}_3(J'')/{}^{p}\mathrm{P}_3(J''+2)$ ratios of the 0-0 vibrational band were calculated up to J'=25. For the lower J' values, the percentage difference between the ${}^{r}\mathrm{R}_3(J'')/{}^{p}\mathrm{P}_3(J''+2)$ ratios calculated with and without including the Herman-Wallis effect is about 0.5% and for the higher J' values, the ratios are between 1% and 2.5%.

In general, the percentage ratios measured from the observed [16] and the calculated spectra are also in good agreement (about 15% discrepancy) and the Herman-Wallis effect in the electronic transition is small.

4.3.3 SPECTRAL VALIDATION

In order to validate the results, two observed astronomical spectra were used. Figure 20, the observed spectrum of the solar photosphere is compared to a synthetic spectrum calculated with the new linelist. The spectra are from high resolution and high signal-to noise observations by Neckel [109]. There is a very good agreement with the solar spectrum testifying to the high quality of our linelist.

While a solar N abundance of 7.78, as employed in this 1D-LTE synthesis, appears consistent with other N indicators [6], a comprehensive 3D model of the solar photosphere is required to confirm this value using our linelist.

In Figure 21, a spectrum of the nitrogen-rich metal-poor star HD196944 obtained with the blue arm of the UVES spectrograph is presented. Concerning the overlaid synthesis, the parameters for this metal-poor star have been adopted from Masseron et al. [96]. In particular, the N abundance has been obtained by Masseron et al. [96] by using CN transitions. Figure 21 demonstrates that there is now very good agreement with the N abundance obtained from the CN lines in contrast to the value obtained with the previous NH linelist. Therefore, we conclude that the problem of the N abundance discrepancy between CN and NH indicators as raised by Spite et al. [143] is now solved with our new NH linelist.

4.3.4 LIFETIMES AND EINSTEIN A COMPARISON

The lifetime of an excited rovibronic level depends on the radiative emission to all lower states and the non-radiative decay due to predissociation [142]. In this study, the lifetimes in the $A^3\Pi$ excited state were calculated without taking predissociation into account. But, in general, our lifetimes are in good agreement with the values available in the literature (Table 4). Einstein A values were calculated for several vibrational bands and compared with values available in the literature, and they are in agreement (Table 5).

It is difficult to estimate the error in the NH Einstein A values obtained by *ab initio* calculations except by analogy with similar calculations for a system such as OH^+ with more information. An error analysis was carried out by Hodges et al. [59]

for the $A^3\Pi - X^3\Sigma^-$ system of isoelectronic OH^+ and, based in part on astronomical observations, and the error was estimated to be about 10%. We can expect a similar error for the NH $A - X$ system as well.

The experimental lifetimes in the literature for $v' = 0$ and 1 differ by significant amounts (Table 5). It is not clear which values should be used to calibrate the line intensities so we recommend that our values, based on theory alone, be used.

4.4 CONCLUSION

A new linelist for the NH $A-X$ transition has been generated. The line intensities were obtained with a dipole moment function calculated *ab initio* with a large basis set and with extensive electron correlation. The calculated line intensities included the Herman-Wallis effect. In contrast to the infrared bands, the Herman-Wallis effect is small for the $A - X$ transition. Two astronomical spectra were used for the validation of the results and the calculated spectra are in good agreement with the observed spectra. The Einstein A values and lifetimes were compared with values available in the literature and they are generally in good agreement.

(A portion of the linelist is given in the Table 6. The linelist includes e/f parity, the quantum numbers J, N and v for each state, line positions, oscillator strengths and Einstein A values.)

CHAPTER 5

INFRARED ABSORPTION CROSS SECTIONS OF HOT ISOBUTANE

Preparation of the experimental setup to record isobutane and CO_2 spectra was done by M. Dulick (Old Dominion University). Recording of isobutane and CO_2 spectra was also done by M. Dulick collaborating with me. All the cross section calculations in this chapter were done by me. P. Bernath (Old Dominion University) is the supervisor of this project.

5.1 INTRODUCTION

Hydrocarbons are found in planetary and exoplanetary atmospheres [124, 89]. Butane is a hydrocarbon that exists in the Earth's atmosphere mainly from anthropogenic emissions [117, 45]. Titan is a moon of Saturn with a dense atmosphere of N_2 and CH_4 capable of forming hydrocarbons including potentially butane through photochemical formation [30]. Propane has already been detected on Titan [110] and also on Saturn [46]. Dobrijevic et al. [30] predicted with a photochemical model that butane should also exist on Titan with a similar abundance as propane. A one-dimensional coupled ion-neutral photochemical kinetics and diffusion model of Titan predicts the production of isobutane [157]. However, most of these photochemical model studies of Titan do not distinguish between the abundances of *n*-butane and isobutane [172, 30]. The detection of methane, propane and ethane in the atmospheres of Jupiter and Saturn and the detection of methane in brown dwarfs and exoplanets suggests that hydrocarbons such as butane might also be found in hot Jupiter exoplanets. Hot hydrocarbons have also been detected in aural regions of Jupiter [7, 48, 87, 146].

Butane (C_4H_{10}) has two isomers, *n*-butane with C_{2h} symmetry and isobutane with C_{3v} symmetry at equillibrium [31, 154]. Isobutane has 24 fundamental vibrational frequencies, 8 with a_1 symmetry, 4 optically forbidden a_2 modes (ν_9 - ν_{12}) and 12 doubly degenerate e modes (ν_{13} - ν_{24}). We have recorded high resolution spectra of pure isobutane at four temperatures in the spectral region 2500 - 3500 cm^{-1} to

provide absorption cross sections to aid the detection of isobutane in hot Jupiters, brown dwarfs and exoplanets.

Isobutane was initially studied in Raman and infrared spectroscopy in liquid and gaseous form in 1950s. In 1960, Lide [86] showed that isobutane molecule belongs to C_{3v} point group by measuring and analyzing microwave spectra. In 1969, Weiss and Leroi [160] derived torsional frequencies from a number of combination bands of isobutane in the spectral region 200 - 800 cm^1 from recorded infrared spectra under high pressure conditions. In 1994, Manzanares et al. [94] measured spectra of the fundamental and overtones of C-H stretches of $(CH_3)_3CH$ (isobutane) at 90 K and at 135 K with liquid samples. Manzanares et al. [94] also performed *ab initio* calculations to obtain geometry parameters for bond lengths, bond angles and vibrational frequencies. Theoretical calculations for infrared intensities of all vibrations and frequencies were carried out by Schrader et al. [133] in 1984. In 1999, Mirkin and Krimm [101] performed *ab initio* calculations for normal mode frequencies. A local mode analysis and partial rotational assignments were carried out in 2019 by Bernath et al. [13] with the help of *ab initio* calculations and high-resolution infrared spectra of the symmetric top isobutane. In 1972, Hilderbrandt and Wieser [58] determined the molecular structure of isobutane in the gas phase with electron diffraction data and rotational constants from microwave spectroscopy. In 1997, ground state rotational spectrum of isobutane was measured in microwave, millimeter-wave and submillimeter wave regions by Priem et al. [118]. The infrared absorptions cross sections in the region 2500 - 3500 cm^{-1} were determined by Hewett et al. [57] from recorded infrared spectra of isobutane in 2019.

5.2 CALCULATIONS

In order to obtain a transmission spectrum, three steps were followed. The first step is to record an interferogram without the sample (in this case, isobutane) in the cell and calculate the Fourier transformed emission spectrum A_{ref} (Figure 22a). The second step is to obtain the Fourier transformed absorption spectrum A_{abs} with the sample in the cell (Figure 22b). As the final step the transmission spectrum τ is obtained taking the ratio of A_{abs} and A_{ref} (Figure 22c). Background emission corrections are needed if the tube furnace is heated above 373 K. The calculations of transmission spectra are done using the software OPUS provided by Bruker. OPUS allows you to control and manipulate spectral parameters and convert transmission

spectra into absorption cross sections.

5.3 EXPERIMENT

Transmission spectra of isobutane were recorded for six different temperatures, 295 K, 373 K, 473 K, 573 K, 673 K and 723 K using a sealed quartz cell, a furnace (accurate within ±10°C) and a Bruker IFS 125HR Fourier transform spectrometer. For each temperature (except for 295 K) two transmission spectra were recorded with the glower. The spectrum was recorded with isobutane in the cell (A_{tr}) at pressure 1 Torr and the other without isobutane in the cell (A_{ref}). In order to correct these transmission spectra for background emission, another two spectra were recorded with the lamp turned off; one without isobutane in the cell (B_{ref}) and the other with isobutane in the cell (B_{em}). All transmission spectra were recorded in the spectral region 2400 - 5500 cm^{-1}. A pressure gauge was not used to measure pressure inside the cell. Instead, isobutane was pumped into the cell after the pressure was measured inside the cell at room temperature with a Baratron pressure gauge that was calculated for the relevant experimental temperatures inside the cell using the ideal gas law. The other parameters used for the experiment are listed in the Table 7. For room temperature (295 K), background emission spectra were not recorded and the emission spectrum was calculated by taking the ratio between A_{abs} and A_{ref} (uncorrected emission spectrum). For the temperatures 373 K, 473 K, 573 K, 673 K and 723 K spectra were corrected using the Equation 57 (corrected emission spectrum). Cross sections were calculated for all the temperatures using corrected (except 295 K) and uncorrected emission spectra; and the values are given in the Table 8.

$$\tau = \frac{A_{\text{abs}} - B_{\text{em}}}{A_{\text{ref}} - B_{\text{ref}}} \tag{55}$$

The six transmission spectra were converted to cross sections using Equation 56 provided by Harrison and Bernath [51],

$$\sigma(\nu, T) = -\frac{10^4 \text{k}_\text{B} T}{Pl} \ln \tau(\nu, T). \tag{56}$$

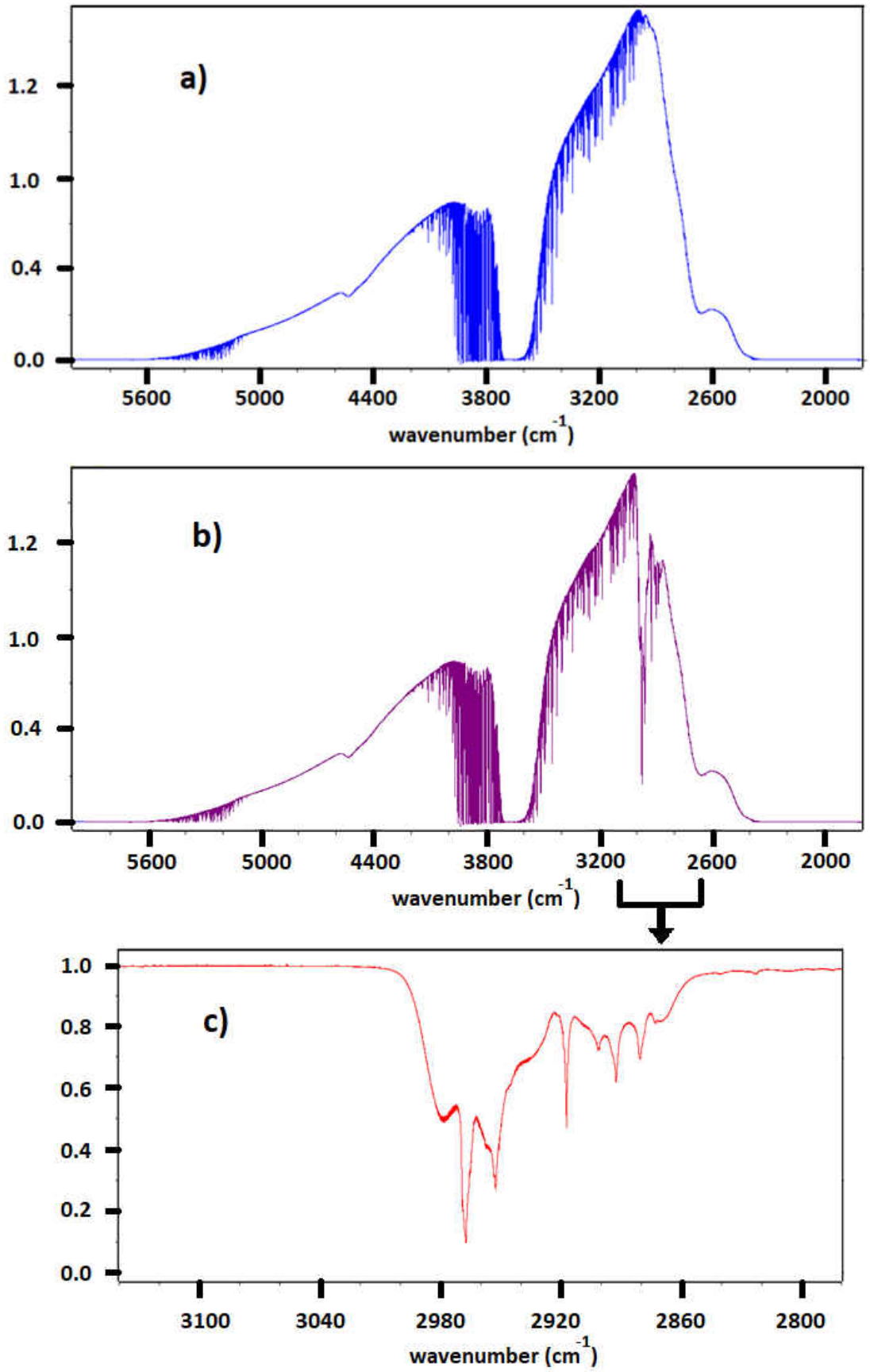

FIG. 22: a) Absorption, b) emission and c) transmission spectra of isobutane recorded at room temperature (295 K).

TABLE 7: Experimental conditions

Parameter	Value
Detector	InSb
Beamsplitter	CaF_2
Spectrometer Windows	CaF_2
Lens	CaF_2
Filters	Ge
Scans	128 coadds
Resolution (cm^{-1})	0.01
Zero filling factor	$\times$ 16
Path length	50.8 cm

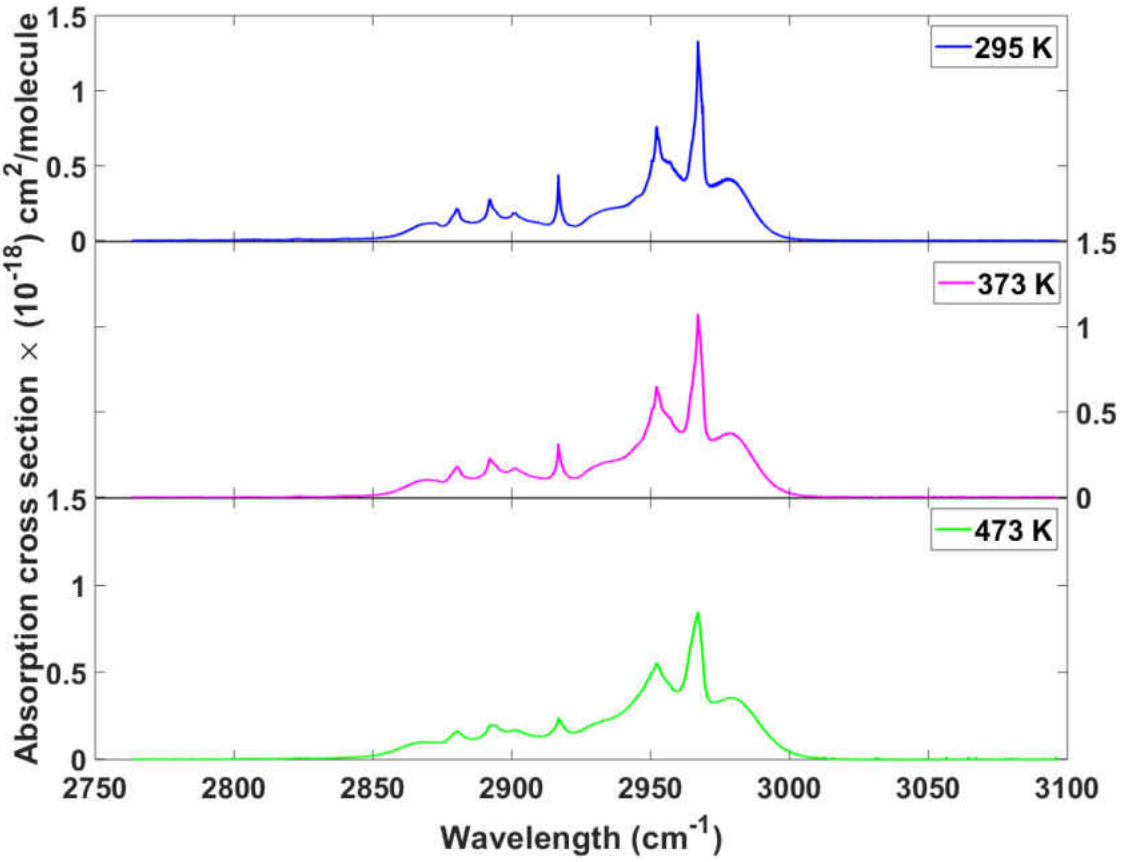

FIG. 23: Integrated absorption cross sections of isobutane for temperatures 295 K, 373 K and 473 K

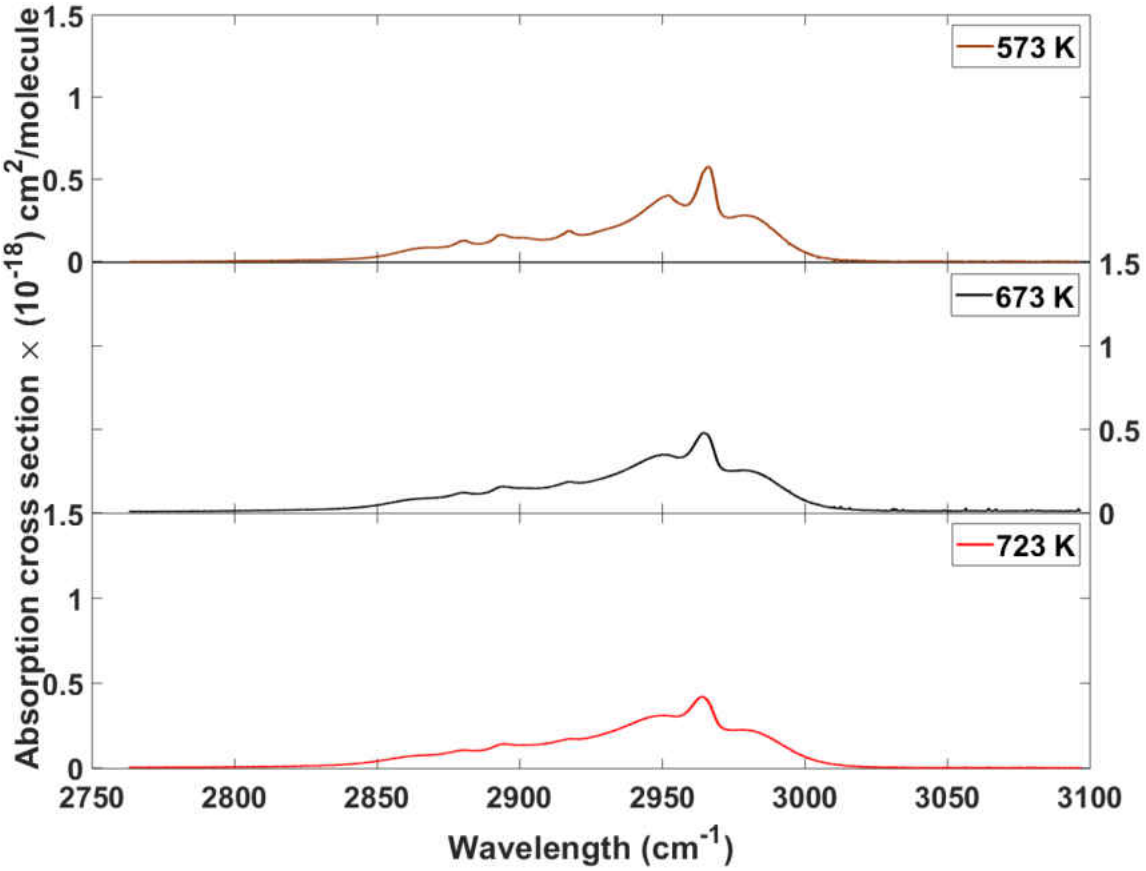

FIG. 24: Integrated absorption cross sections of isobutane for temperatures 573 K, 673 K and 723 K

TABLE 8: Temperature calibrated absorption cross sections of isobutane

Experimental Temperature (K)	Calibrated Temperature (K)	Emission uncorrected $\times 10^{-17}$ (cm/molecule)	Emission corrected $\times 10^{-17}$ (cm/molecule)
295	295	3.4365	-
373	354.8	3.3045	3.3665
473	463.4	3.4796	3.5502
573	573	3.0810	3.1465
673	685	2.7312	2.9303
723	738.5	2.5063	2.7819

Here, the transmittance at wavenumber ν cm^{-1} represents by $\tau(\nu, T)$, temperature by T in K, pressure of the absorbing gas by P in Pa, path length of the cell by l in m and Boltzmann constant by k_B in J/K.

5.4 CALIBRATION

Although the integrated cross sections for an isolated band should not depend on temperature, our calculated cross sections of isobutane show a temperature dependence.

The Pacific Northwest National Laboratory (PNNL) database provides infrared spectra of isobutane for 3 temperatures (278 K, 298K and 323 K) with 1 atm of N_2 broadening gas [134]. We integrated the cross sections of isobutane of PNNL and our spectra for all the available temperatures (from 2770.3610 cm^{-1} to 3070.1000 cm^{-1}). Our integrated cross sections (temperature calibrated) are presented in the Table 8. PNNL integrated cross sections are 4.7953×10^{-17} cm/molecule, 4.7916×10^{-17} cm/molecule and 4.8214×10^{-17} cm/molecule for the temperatures 278 K, 288 K and 323 K (PNNL cross section values and our values have a discrepency), respectively. Since the y-axis of the PNNL spectrum was in ppm m, to convert it to standard units in which our spectrum was calculated, the PNNL spectrum was multiplied by 9.28697×10^{-16}. Integrated cross sections of spectra recorded at six temperatures and are shown in the Figure 23 and 24. Temperature was not constant through out the cell. Therefore, the average temperature along the cell was given for each temperature as the calibrated temperature in the Table 8. A separate experiment was carried out using a thermocouple to measure the temperature along the cell. The measured value in the center of the cell is used as the calibrated value.

5.5 CONCLUSION

High resolution pure isobutane spectra were recorded at Old Dominion University. The spectra were recorded in the 3 μm region for temperatures 295 K, 373 K, 473 K, 573 K, 673 K and 723 K. Recorded spectra were converted to integrated cross sections by correcting for background emissions using Bruker's OPUS software. These cross section values can be used to simulate atmospheric spectra of exoplanets, hot Jupiters and brown dwarfs which might contain isobutane. Integrated cross sections show a temperature dependence (decreasing with increasing temperature). Also, our integrated cross sections were compared with the data from the Pacific Northwest

National Laboratory (PNNL) and they show a discrepancy.

CHAPTER 6

OZONE ISOTOPOLOGUE MEASUREMENTS FROM THE ATMOSPHERIC CHEMISTRY EXPERIMENT (ACE)

The results and the majority of the material presented in this chapter are published in the Journal of Quantitative Spectroscopy & Radiative Transfer (Fernando et al. [37]). The co-authors of this publication are: P. Bernath (Old Dominion University) and C. Boone (Univeristy of Waterloo). C. Boone is the ACE project scientist who carried out retrievals from ACE-FTS, using resources at the University of Waterloo. Calculation of the atmospheric "forward model" to prepare volume mixing ratio profiles for normal ozone and ozone isotopolgues were also done by him. P. Bernath is the mission scientist for ACE and the advisor of this project. As the first author of this publication, analysis of ozone data, preparation of figures and writing the text were carried out by me. This work is original and has not published anywhere prior to the publication in the Journal of Quantitative Spectroscopy & Radiative Transfer.

6.1 INTRODUCTION

In general, elements exist as a mixture of isotopes or isotopologues. The existence of isotopes/isotopologues in a system with different compositions is called isotopic/isotopologue fractionation. There are two different fractionation types that are recognized: mass dependent and mass independent [95, 91]. Mass dependent fractionation occurs due to mass differences of isotopes/isotopologues that affect physical properties of isotopes/isotopologues. Hence, vibrational and rotational frequencies, thermodynamic energies and photochemical cross sections cause different isotopes/isotopologues to react at different rates and partition unequally between reactants and products. As a result, several mass dependent processes in isotopic systems give predictable fractionations. As an example, mass dependent fractionation of oxygen reflects the mass difference between ^{18}O and ^{16}O. The mass difference

between ^{18}O and ^{16}O is 2 atomic mass units and there is 1 atomic mass unit difference between ^{16}O and ^{17}O, so the fractionation of ^{18}O is twice that of ^{17}O [70, 95]. Mass independent fractionation occurs when isotopes/isotopologues are associated with biogeochemical, photochemical, exchange, association and dissociation reactions; and does not relate to the mass differences of relevant isotopes/isotopologues [8, 114, 132]. As an example, the ratio between the mass independent fractionation of the isotopolgues $^{16}O^{16}O^{18}O$ and $^{16}O^{17}O^{16}O$ in the Earth's stratosphere is around 1 i.e., their fractionation is about the same.

Ozone isotopologues show high fractionations in the Earth's stratosphere compared to normal mass dependent ozone fractionations observed elsewhere. This isotopic signature can be transferred to other trace gases in the atmosphere (CO_2, CO and N_2O). Therefore, information on atmospheric transport and chemical reactions can be obtained by monitoring this atmospheric feature.

Mass spectrometers cannot determine the symmetry of isotopomers. An isotopologue is any isotopically substituted molecule and an isotopomer is an isotopic isomer such as $^{16}O^{16}O^{18}O$ and $^{16}O^{18}O^{16}O$ where both species are isotopologues [37]. The notation $^{50}O_3$ represents both isotopomers $^{16}O^{16}O^{18}O$ and $^{16}O^{18}O^{16}O$ where it distinguishes only the mass number (in this case mass number is 50). Generally, in an ozone sample, 1/3 of $^{50}O_3$ consists of the symmetric molecule $^{16}O^{18}O^{16}O$ and 2/3 of the asymmetric molecule $^{16}O^{16}O^{18}O$ (similar for $^{49}O_3$).

In 1980, Cicerone and McCrumb [23] showed that high ozone fractionations should be expected 40 km above the Earth's surface in the stratosphere. In 1981, balloon based mass spectroscopic measurements by Mauersberger [97] found that the stratosphere was highly fractionated with $^{16}O^{18}O^{16}O$ and $^{16}O^{16}O^{18}O$ enhanced in abundance relative to $^{16}O^{16}O^{16}O$. In 2001, mass spectrometric observations made by Mauersberger et al. [99] in the mid-stratosphere of $^{50}O_3$ showed fractionations () between 7-9% and of $^{49}O_3$ (represents the isotopomers $^{16}O^{16}O^{17}O$ and $^{16}O^{17}O^{16}O$) showed values between 7-11%. Mass spectrometer data measured by Krankowsky et al. [73] showed that $^{50}O_3$ fractionations at 22-33 km is 7-11% and $^{49}O_3$ fractionations slightly lower compared to $^{50}O_3$. In 2007, Krankowsky et al. [74] again determined the altitude dependence of ozone fractionations with balloon measurements. Far-infrared spectrometer data obtained with balloon measurements by Johnson et al. [66] showed that $^{50}O_3$ fractionated by 12.3% and $^{49}O_3$ by 10.7%. Similarly, Irion et al. [62] confirmed previously observed high isotopic fractionations in the

stratosphere with in-orbit ATMOS (Atmospheric Trace Molecule Spectroscopy) measurements. Atmospheric data obtained from MIPAS (Michelson Interferometer for Passive Atmospheric Sounding) instrument by Jonkheid et al. [67], shows fractionations ∼8% with an increasing vertical profile up to 33 km, with decreasing values at higher altitudes, and $^{16}O^{18}O^{16}O$ shows values around 3%. Similar fractionations for heavy isotopes were observed in laboratory measurements as well, supporting the atmospheric observations [98, 64, 149].

6.1.1 OZONE FRACTIONATION

Ozone fractionation process in the stratosphere is mass independent since it does not reflect the mass difference between ozone isotopologues. The main process responsible for stratospheric ozone fractionation is the reaction of ozone formation by recombination (XY + Z + M → XYZ + M; X, Y, Z represent different oxygen isotopes). During this recombination process, a vibrationally excited ozone complex is formed and is stabilized to form normal ozone (XY + Z ⇌ XYZ^* → XYZ), to complete the process.

This intermediate ozone complex can also dissociate into different oxygen atoms and molecules as well (X + YZ ← XYZ^* → XY + Z). This process is called the exchange reaction (X + YZ ⇌ XY + Z). This process also plays a major role in ozone fractionation [132, 17]. Ozone fractionation occurs due to different reaction rates of the recombination reaction and of the ozone exchange reaction with different atomic isotopes, molecular isotopologues and isotopomers [43, 132, 44].

O_3 can photolyze and produce oxygen atoms and molecules. Photolysis of O_3 provides a minor contribution to ozone fractionation. In this process, O atoms are generated by O_3 photolysis and react with stratospheric O_2 to re-form ozone. Ozone photolysis produces singlet and triplet oxygen atoms ($O_3 + h\nu \rightarrow O(^1D) + O_2(^1\Delta_g)$ and $O_3 + h\nu \rightarrow O(^3P) + O_2(^3\Sigma_g^-)$). $O(^1D)$ atoms produced in this process can be quenched by N_2 and O_2. These excited $O(^1D)$ atoms produce more $O(^3P)$ atoms which recombine with O_2 to produce ozone. In order to keep the ozone budget balanced in the stratosphere, odd oxygen reacts with ozone to re-form molecular oxygen ($O + O_3 \rightarrow 2O_2$). This odd oxygen cycling reaction is faster than source and sink reactions and limits the ozone fractionation significantly [18]. It should be noted that ozone photolysis only provides a minor contribution to ozone fractionation compared to ozone formation and it was not recognized as important until recently

[53].

Observations and retrievals: Ozone and its isotopologue VMR profiles ($^{16}O^{16}O^{16}O$, $^{16}O^{16}O^{18}O$, $^{16}O^{18}O^{16}O$, $^{16}O^{17}O^{16}O$) are provided on a vertical grid of 1 km from about 5 km (or the cloud tops) up to ∼50 km (for the minor isotopologues) covering latitudes 85°N to 85°S [11]. For this work version 3.5/3.6 of ACE-FTS processing is used for 2014-2018. Version 3.5/3.6 uses spectroscopic line parameters for ozone from the HITRAN 2004 database [129].

6.1.2 FRACTIONATION PROCESS

Isotopic fractionation is defined as:

$$\delta(\%) = 100 \left(\frac{R}{R_0} - 1 \right) \tag{57}$$

in which R = $[O_3]_{\text{isotopologue}}/[O_3]$ is the observed ratio of ozone isotopologue and normal ozone VMRs (volume mixing ratios). The convention is that the VMR of the most abundant isotopologue (in this case $^{16}O^{16}O^{16}O$) should be in the denominator and the VMR of the less abundant isotopologue in the numerator. R_0 is a reference ratio used to obtain a meaningful number for fractionation. For this study, in order to calculate the reference ratio, VSMOW (Vienna Standard Mean Ocean Water) is used with $R_0(^{18}O) = 0.00200520$ and $R_0(^{17}O) = 0.000373$ [137]. These reference ratios are only available for atomic oxygen. The likelihood of randomly finding non-symmetric ozone (QOO) in a sample is twice as large as the symmetric ozone (OQO) (with heavy oxygen atom is denoted by Q). Therefore the reference VMRs were multiplied by 2 to obtain δ values for non-symmetric isotopologue [37].

6.2 DATA SET

We used ozone fractionations derived from isotopologue measurements available in the literature to compare with ACE-FTS values. We used fractionation data from the space-based solar absorption spectra recorded by the ATMOS (Atmospheric Trace Molecule Spectroscopy Experiment) Fourier transform spectrometer [62]; data from the balloon-borne solar absorption spectra by the MkIV FTIR (Fourier Transform Infrared Interferometer) spectrometer [53]; data from mass spectrometer measurements

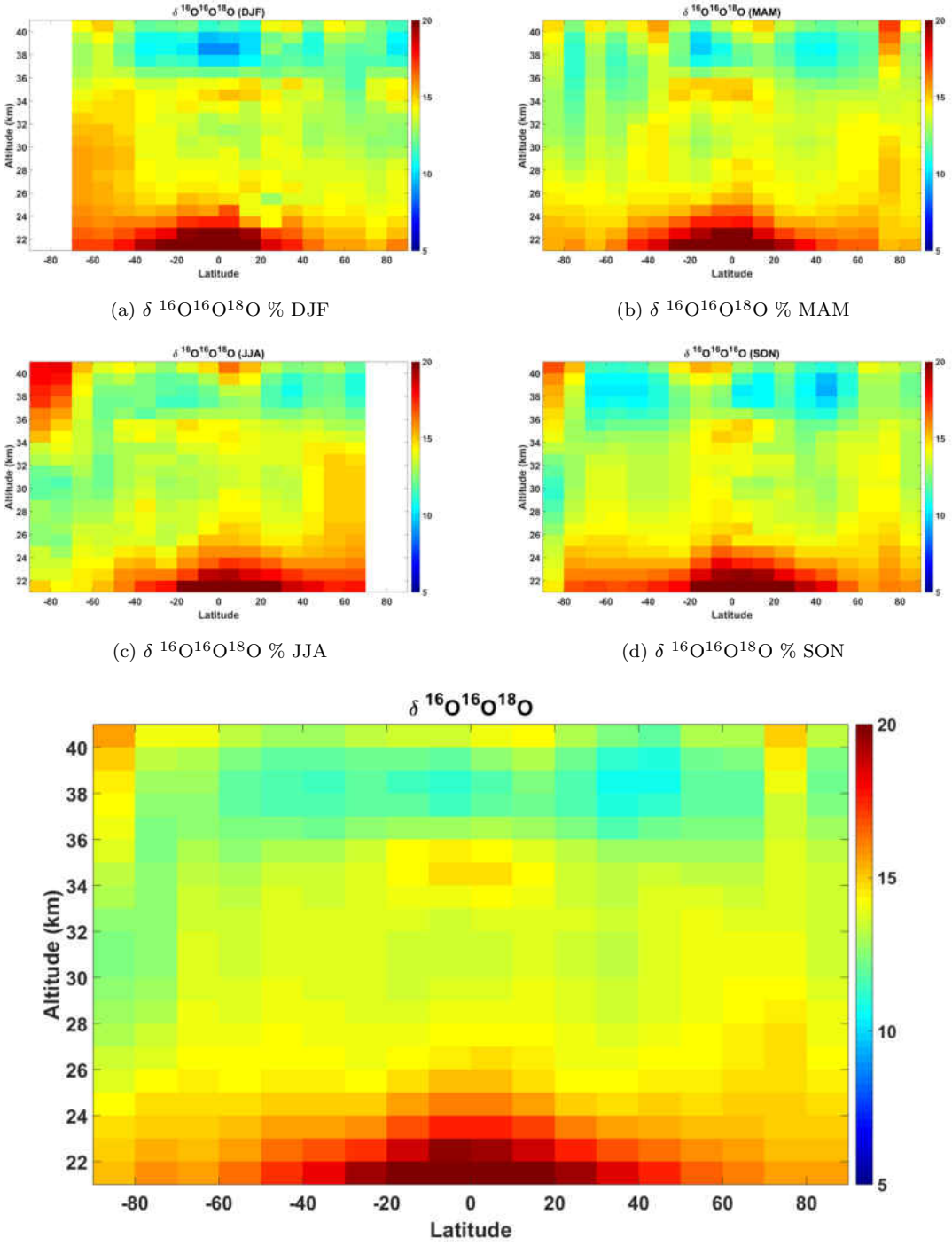

(a) δ $^{16}O^{16}O^{18}O$ % DJF

(b) δ $^{16}O^{16}O^{18}O$ % MAM

(c) δ $^{16}O^{16}O^{18}O$ % JJA

(d) δ $^{16}O^{16}O^{18}O$ % SON

(e) δ $^{16}O^{16}O^{18}O$ % mission average

FIG. 25: δ $^{16}O^{16}O^{18}O$ % (latitude distribution).

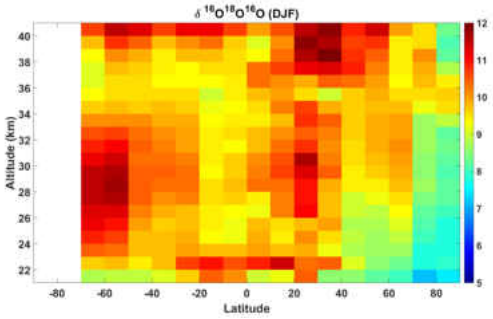

(a) δ $^{16}O^{18}O^{16}O$ % DJF

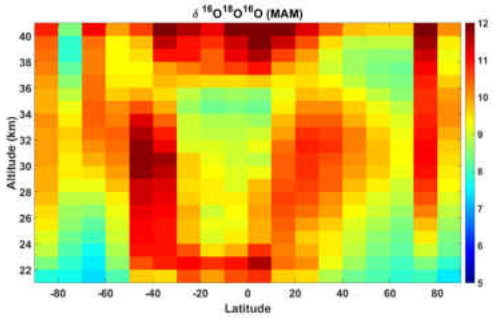

(b) δ $^{16}O^{18}O^{16}O$ % MAM

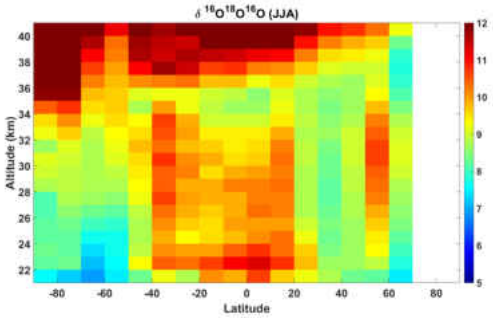

(c) δ $^{16}O^{18}O^{16}O$ % JJA

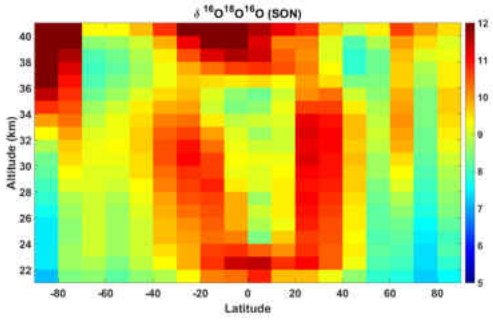

(d) δ $^{16}O^{18}O^{16}O$ % SON

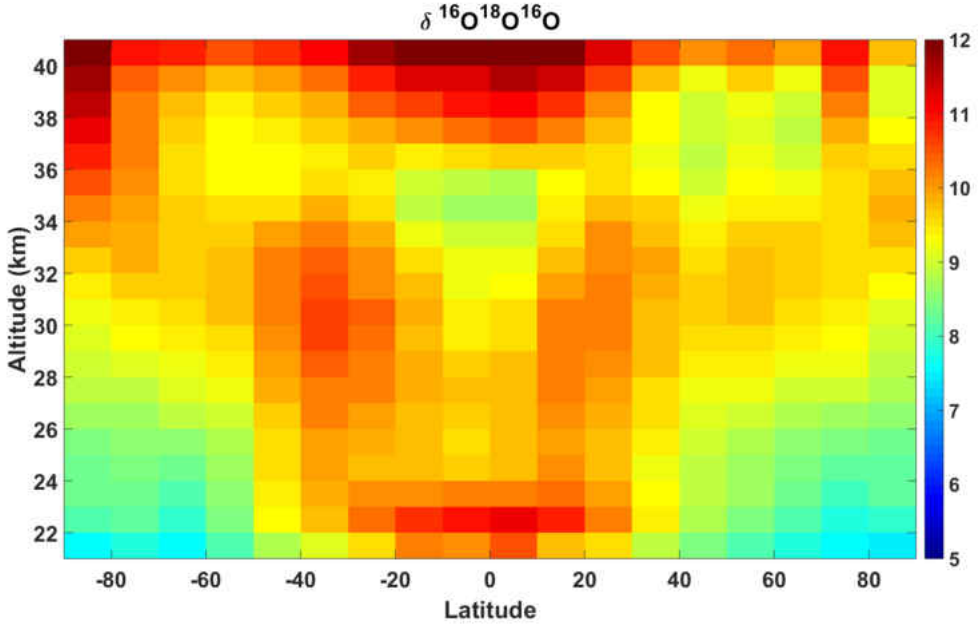

(e) δ $^{16}O^{18}O^{16}O$ % mission average

FIG. 26: δ $^{16}O^{18}O^{16}O$ % (latitude distribution).

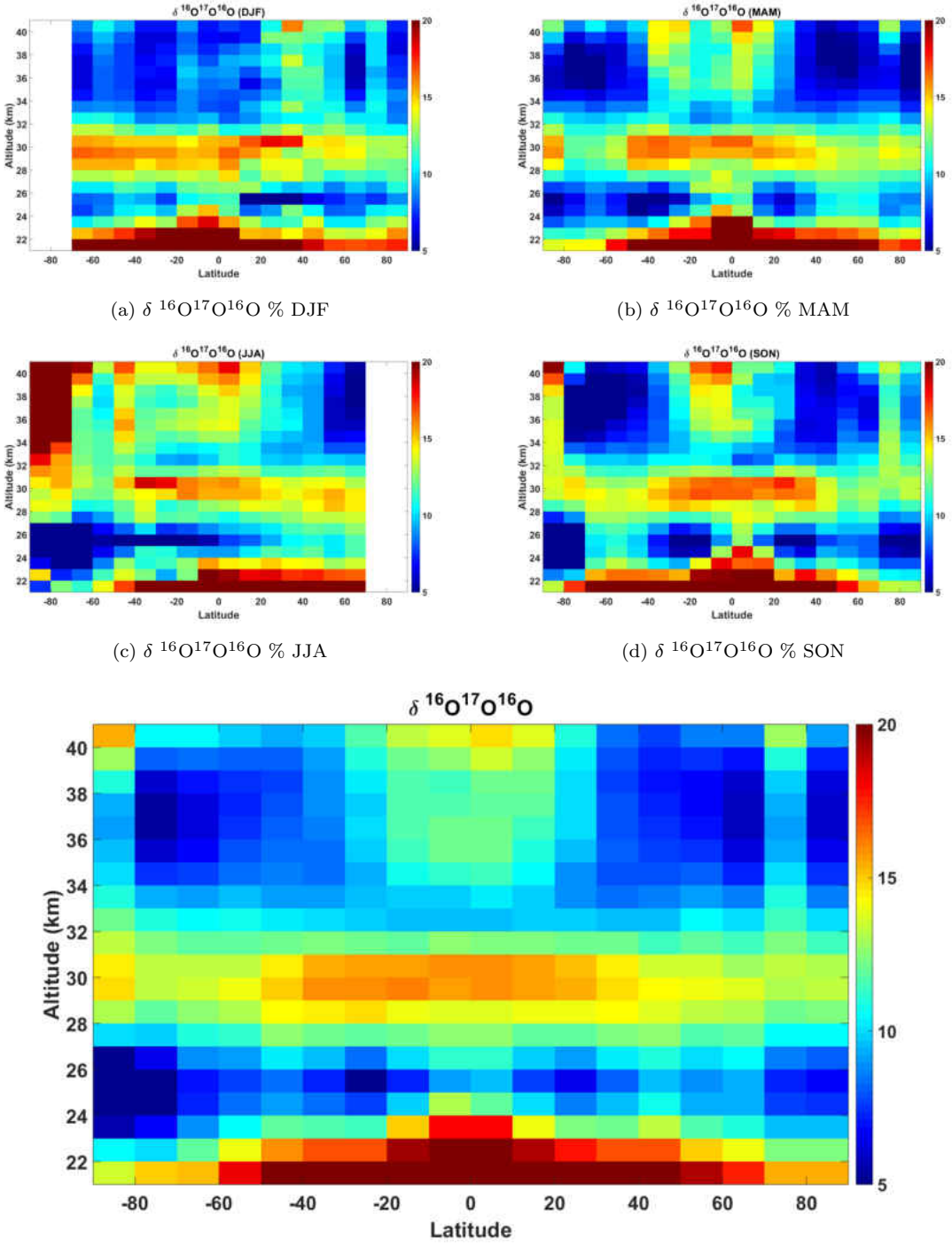

(a) δ $^{16}O^{17}O^{16}O$ % DJF

(b) δ $^{16}O^{17}O^{16}O$ % MAM

(c) δ $^{16}O^{17}O^{16}O$ % JJA

(d) δ $^{16}O^{17}O^{16}O$ % SON

(e) δ $^{16}O^{17}O^{16}O$ % mission average

FIG. 27: δ $^{16}O^{17}O^{16}O$ % (latitude distribution).

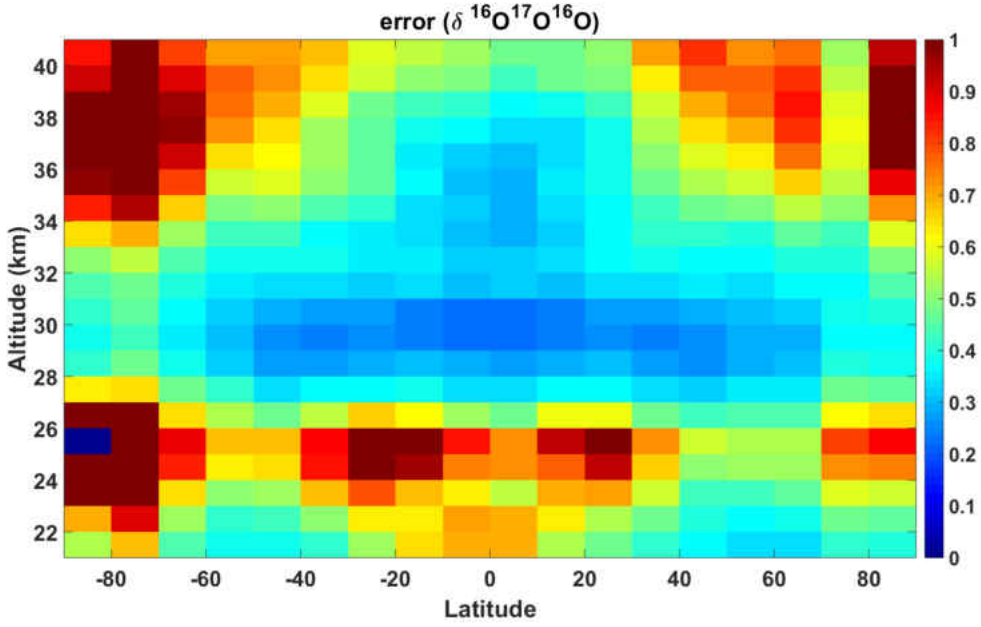

FIG. 28: Standard deviation of δ $^{16}O^{17}O^{16}O$ % altitude-latitude bins.

of samples collected with high altitude balloons [74]; data from the Michelson Interferometer for Passive Atmospheric Sounding (MIPAS) [67]; data from the balloon-borne thermal emission spectra by the FIRS-2 Fourier transform spectrometer [66] and MIPAS-Balloon measurements [116] to validate ACE-FTS data [37].

Jonkheid et al. [67] derived altitude profiles of δ values of $^{50}O_3$ from the above mentioned datasets for five latitude bins (polar, mid-latitude and tropics). Also, altitude profiles of δ values of $^{16}O^{16}O^{18}O$ and δ $^{16}O^{18}O^{16}O$ were derived from MIPAS-Balloon data by Piccolo et al. [116] and from MkIV FTIR data by Haverd et al. [53]. These altitude profiles were extracted from the figures provided in the respective journal papers and were used for comparison with ACE-FTS data [37].

The ATMOS data were derived from the missions Spacelab-3 (April-May 1985), Atlas-1 (March 1992), Atlas-2 (April 1993) and Atlas-3 (November 1994) [62, 67]. The FIRS-2 data were obtained from seven balloon flights launched from Fort Sumner (35°N), Daggett (45°N) and Fort Wainwright (65°N) between 1989 and 1997. The mass spectrometer data were taken from 11 balloon flights launched from Kiruna (68°N), Aire sur l'Adour, and Teresina (5°S) between 1998 and 2005 [66, 67]. The MkIV FTIR data were obtained from seven balloon flights launched from Fort Sumner (35°N), Esrange (68°N) and Fort Wainwright (65°N) between 1997 and 2003

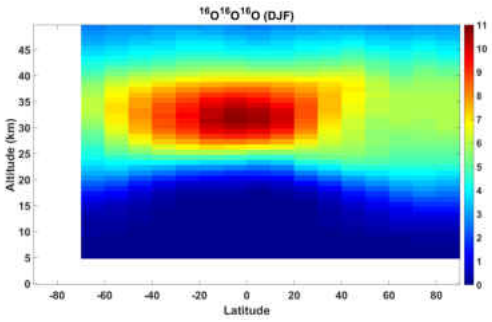

(a) $^{16}O^{16}O^{16}O$ (ppm) DJF

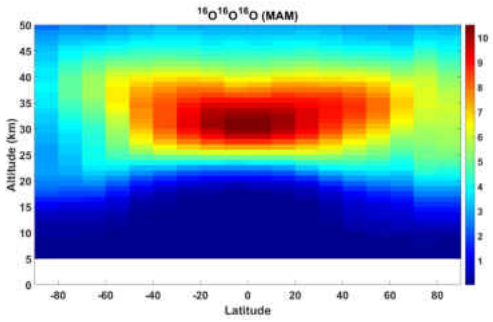

(b) $^{16}O^{16}O^{16}O$ (ppm) MAM

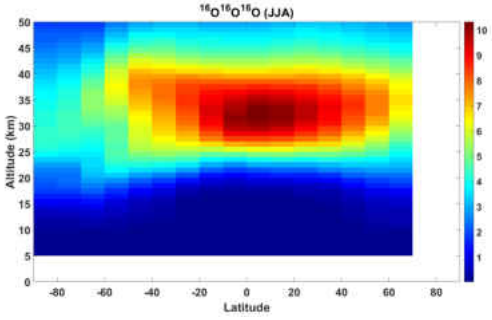

(c) $^{16}O^{16}O^{16}O$ (ppm) JJA

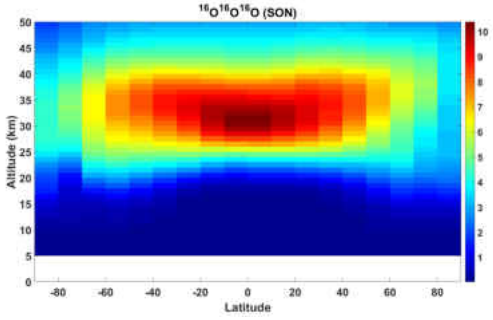

(d) $^{16}O^{16}O^{16}O$ (ppm) SON

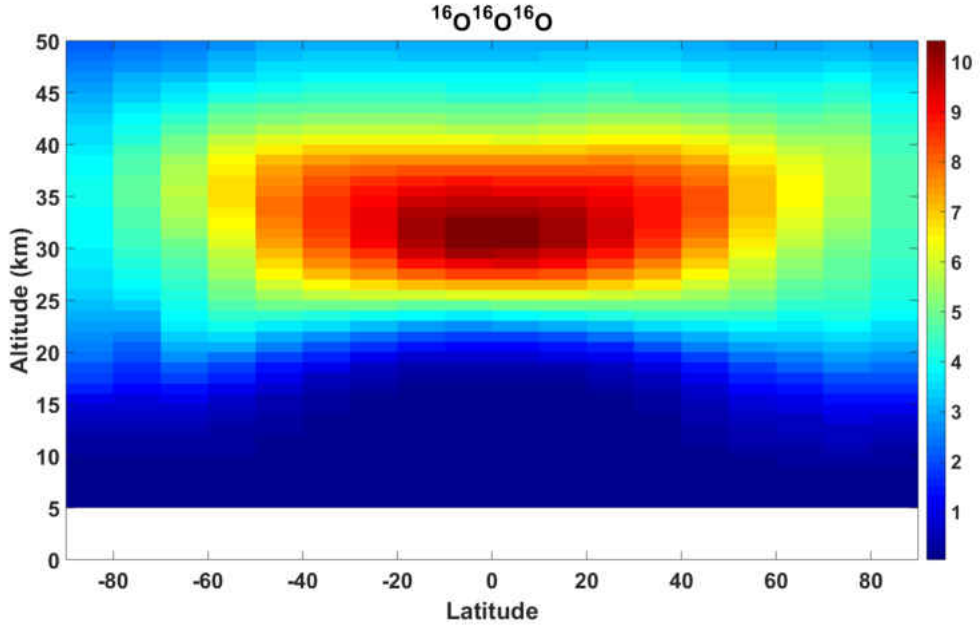

(e) $^{16}O^{16}O^{16}O$ mission average (ppm)

FIG. 29: $^{16}O^{16}O^{16}O$ VMRs in ppm.

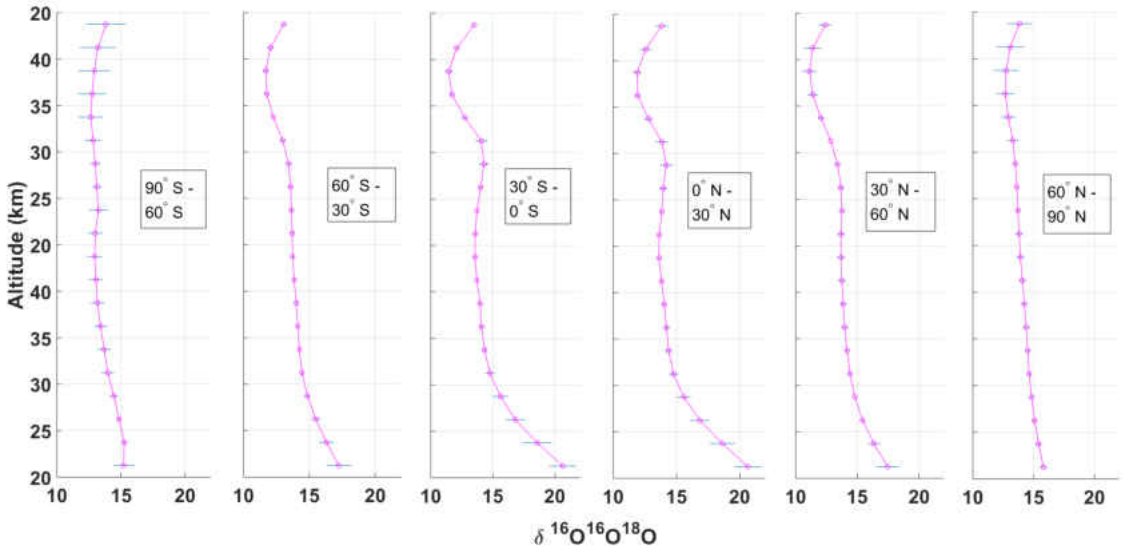

FIG. 30: Altitude profiles of δ% values of $^{16}O^{16}O^{18}O$ for different latitude bins.

[53, 67]. MIPAS-Balloon measurements [116] (balloon-borne version of the MIPAS satellite instrument) were recorded in Aire sur l'Adour, France (43.7°N) on 24 September 2002 and in Kiruna, Sweden (67.5°N) on 20/21 March 2003 [37].

6.3 RESULTS AND DISCUSSION

The ACE-FTS isotopologue VMR data of normal ozone ($^{16}O^{16}O^{16}O$) and three isotopologues ($^{16}O^{16}O^{18}O$, $^{16}O^{18}O^{16}O$ and $^{16}O^{17}O^{16}O$) are available for 6.5 km to 49.5 km in 1 km grid and each altitude level contains around 70,000 occultations. This analysis is restricted to the altitude 20.5 km - 40.5 due to high statistical errors outside the range. δ values of the isotopologues were calculated using the equation 57 after discarding large negative and positive values of isotopologue VMRs (VMR values greater than about 100 ppm and less than 0.1 ppm). The calculated δ values were put into 10° latitude bins for each altitude level and values that were more than two standard deviations from the bin average were discarded. Then the quarterly mission averages for Dec−Feb (DJF), Mar−May (MAM), Jun−Aug (JJA), Sep−Nov (SON) and the mission average latitudinal distributions of δ values were obtained (Figures 25, 26, 27) for each isotopologue. One standard deviation error bars are also displayed in the calculated altitude figures of δ values [37].

The mission average (2004 - 2018) latitudinal distribution of $^{16}O^{16}O^{18}O$ shows

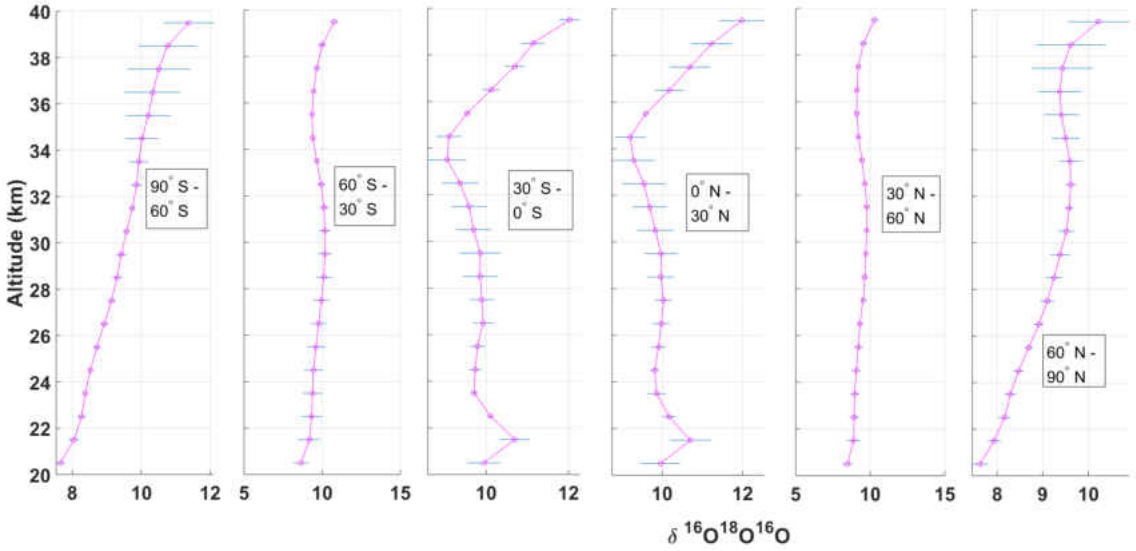

FIG. 31: Altitude profiles of δ% values of $^{16}O^{18}O^{16}O$ for different latitude bins.

fractionations ∼20% between the altitudes 21.5 km - 26.5 km, ∼15% between the altitudes 27.5 km - 35.5 km and ∼12% between the altitudes 36.5 km - 40.5 km in the latitude region 45°S - 45°N. The polar region in the Southern Hemisphere (70°S - 90°S) shows less fractionation (∼12%) compared to the Northern Hemisphere (∼15%) (70°N - 90°N). The seasonal latitudinal distributions of $^{16}O^{16}O^{18}O$ show that there is higher fractionation in the polar regions during summer, JJA in the Northern Hemisphere and DJF in the Southern Hemisphere. These enhancements in the tropics and in the summer at high latitudes are consistent with the contribution of photolysis to fractionation. The δ value standard deviations of the altitude-latitude bins of the mission average latitudinal distribution of the isotopologue $^{16}O^{16}O^{18}O$ are around ∼0.15 [37].

The δ values mission average latitudinal distribution of the isotopologue $^{16}O^{18}O^{16}O$ shows high fractionations 10 - 12% between the altitudes 21.5 km - 26.5 km and in the latitude region 45°S - 45°N and smaller fractionations (8 - 9%) in the regions 50° - 90°S,N and between the altitudes 21.5 km - 26.5 km. Above 30.5 km, fractionations start to increase to 10 - 11% in the regions 50° - 90°S,N. Similar to $^{16}O^{16}O^{18}O$ the $^{16}O^{16}O^{18}O$ mission average latitudinal distribution also shows higher fractionations in the Northern Hemisphere during JJA compared to Southern Hemisphere and in Southern Hemisphere compared to Northern Hemisphere during

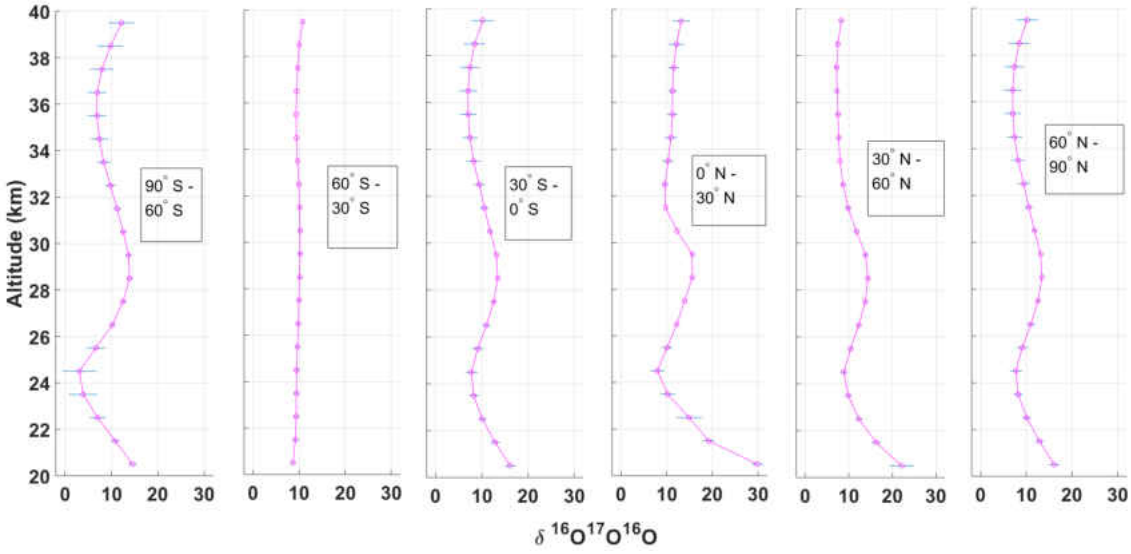

FIG. 32: Altitude profiles of δ% values of $^{16}O^{17}O^{16}O$ for different latitude bins.

DJF when more sunlight is available. The effect of photolysis is also evident in the enhanced fractionation for $^{16}O^{18}O^{16}O$ at high altitudes (above 35 km) in the tropics. Ndengué et al. [108] predict that $^{16}O^{18}O^{16}O$ is preferentially fractionated by ozone photolysis in the Hartley bands at this altitude. The absolute standard deviations of the altitude-latitude bins of the mission average latitudinal distribution of the isotopologue $^{16}O^{18}O^{16}O$ are ∼0.2 [37].

The mission average latitudinal distributions of the isotopologues $^{16}O^{18}O^{16}O$ and $^{16}O^{16}O^{18}O$ of MIPAS data were provided by Jonkheid et al. [67] for 1st of July, 2003. The MIPAS latitudinal distribution of $^{16}O^{16}O^{18}O$ shows a peak around 30 - 35 km for latitudes 90°N - 50°S, but the ACE-FTS latitudinal distribution of $^{16}O^{16}O^{18}O$ does not show such a peak. The MIPAS latitudinal distribution [67] of $^{16}O^{18}O^{16}O$ does not show any features that appear in the ACE-FTS latitudinal distribution [37].

The mission average latitudinal distribution of the isotopologue $^{16}O^{17}O^{16}O$ shows a high fractionation (∼15%) band in the latitudes 27.5 km - 30.5 km. It should be noted that the δ value standard deviations for the $^{16}O^{17}O^{16}O$ latitudinal distribution (Figure 27e) were relatively high. Nevertheless, similar to the latitude distributions of $^{16}O^{18}O^{16}O$ (Figure 26e) and $^{16}O^{16}O^{18}O$ (Figure 25e), the latitude distribution of $^{16}O^{17}O^{16}O$ also shows higher fractionation where more sunlight is available (high values in the Northern Hemisphere during JJA and in Southern Hemisphere during

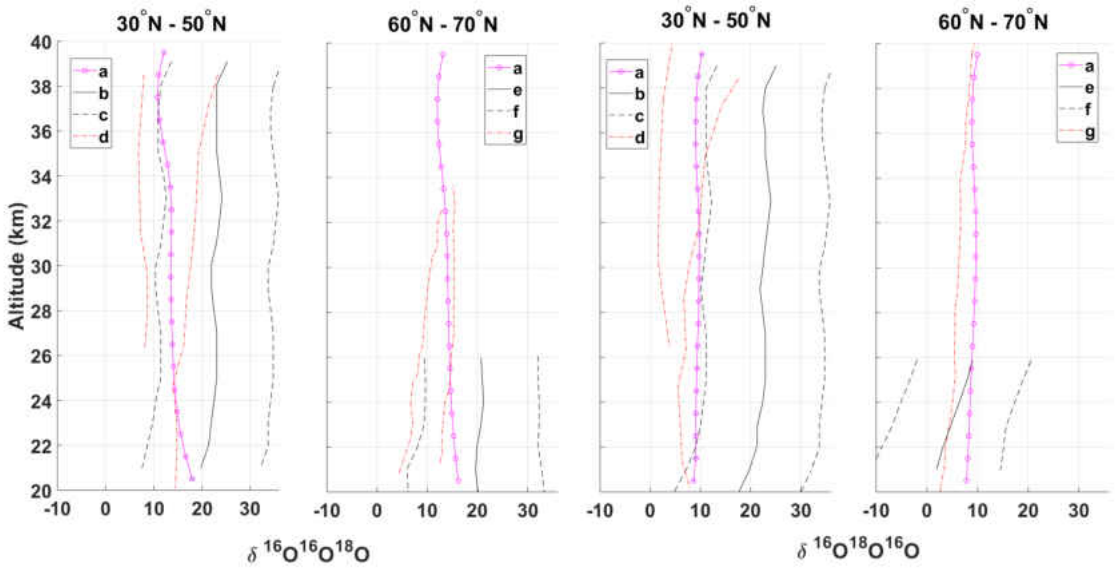

FIG. 33: Comparison of altitude profiles of δ% values of ozone isotopologues. a: This study, b: MIPAS-Balloon measurements at 43.7°N on September 2002 (Piccolo et al. [116]), c: Uncertainty of MIPAS-Balloon measurements at 43.7°N for September 2002 (Piccolo et al. [116]), d: MkIV FTIR data from Fort Sumner (35°N) flights (Haverd et al. [53]), e: Balloon-borne MIPAS-Balloon measurements at 67.5°N in March 2003 (Piccolo et al. [116]), f: Uncertainty of MIPAS-Balloon measurements at 67.5°N for March 2003 (Piccolo et al. [116]), g: MkIV FTIR data from Fairbanks (65°N) flights (Haverd et al. [53]).

DJF) [37].

Standard deviations of all the isotopologues are more than 1 below 20.5 km (down to 6.5 km). Therefore the fractionations below 20.5 km in altitude were not considered in this study. There is a band of high fractionation values above 41.5 km for all the latitudinal distributions (>0.2 for $^{16}O^{16}O^{18}O$, >0.15 for $^{16}O^{18}O^{16}O$, >0.25 for $^{16}O^{17}O^{16}O$). The standard deviation of the observations are also increasing and this band may be an artifact; we have not considered these data. It is also possible that these high fractionation values are due to photolysis in the Hartley bands of ozone (e.g., Ndengué et al. [108]) [37].

For comparison with the heavy ozone isotopologues, the parent ozone molecule was analyzed in the same way and the VMR distributions are presented in Figure 29 [37].

The ACE-FTS mission average altitude profiles of δ values $^{16}O^{16}O^{18}O$, $^{16}O^{18}O^{16}O$ and $^{16}O^{17}O^{16}O$ for 6 latitude bins were presented in the Figures 30, 31 and 32.

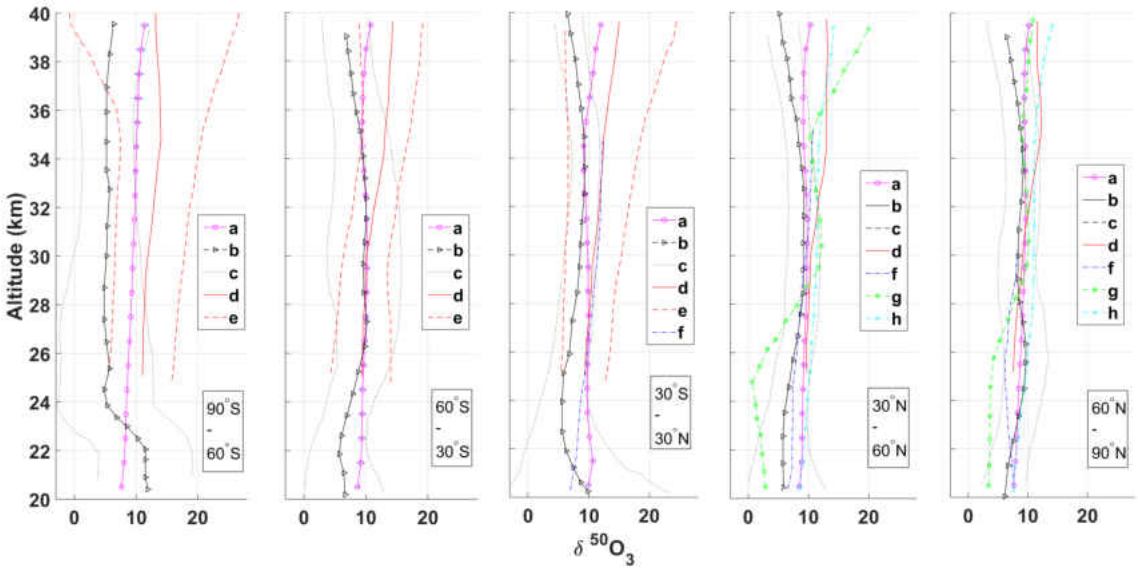

FIG. 34: Comparison of altitude profiles of δ% values of $^{50}O_3$. a: This study, b: MIPAS data of Jonkheid et al. [67], c: Uncertainty in MIPAS data [67], d: ATMOS IR measurements (Irion et al. [62]), e: Uncertainty in ATMOS data [62], f: Mass spectrometer data of Krankowsky et al. [74], g: FIRS-2 measurements (Johnson et al. [66]), h: MkIV FTIR data (Haverd et al. [53]).

Northern polar (90°N - 60°N), northern mid-latitudes (60°N - 30°N), southern tropics (30°S - 0°S), northern tropics (0°N - 30°N), southern mid-latitudes (30°S - 60°S) and southern polar (60°S - 90°S) are the 6 latitude regions that were considered in the analysis [37].

The ACE-FTS average altitude profiles of δ values of $^{16}O^{16}O^{18}O$ (Figure 30) show a local minimum around 35 - 40 km in every latitude region. Typical fractionation values are 13-15% in the mid-stratosphere [37].

The ACE-FTS average altitude profiles of $^{16}O^{18}O^{16}O$ (Figure 31) have typical δ values of about 10% in the mid stratosphere and increase above 35 km. The δ values are relatively constant in the tropics but increase with altitude at high latitudes [37].

δ values of the average altitude profiles of $^{16}O^{17}O^{16}O$ (Figure 32) generally show a local minimum (8%) around 25 km and a local maximum (13%) around 29 km. These observations do not agree, for example, with the predicitions of Liang et al. [85], which have an increasing VMR with altitude [37].

The δ value profiles of $^{16}O^{16}O^{18}O$ and $^{16}O^{18}O^{16}O$ compared with MIPAS-Balloon measurements of Piccolo et al. [116] and FTIR profiles of Haverd et al. [53]. MIPAS-Balloon measurements were taken in Aire-sur-l'Adour, France (43.7°N) and

in Kiruna, Sweden (67.5°N); and MkIV FTIR data in Fort Sumner (35°N) and in Fairbanks (65°N). There are several altitude profiles of δ values of $^{16}O^{16}O^{18}O$ and $^{16}O^{18}O^{16}O$ provided in Haverd et al. [53] that were obtained at Fort Sumner and Fairbanks. In order to compare these profiles with ACE-FTS data, two altitude profiles were selected that represent maximum and minimum δ values of Fort Sumner and Fairbanks profiles (Since δ value of $^{16}O^{18}O^{16}O$ profiles obtained at Fairbanks do not show much deviation from each other only one profile was selected). The ACE-FTS δ value profiles were obtained in the latitude regions 30°N - 50°N and 60°N - 70°N for comparison purposes (Figure 33) [37].

The ACE-FTS profile of $^{16}O^{16}O^{18}O$ in the region 30°N - 50°N lies between the two altitude profiles obtained at Fort Sumner that were selected and within the error bars of the MIPAS-Balloon flight profile obtained at Aire-sur-l'Adour, France (43.7°N). The ACE-FTS profile of $^{16}O^{18}O^{16}O$ in the region 30°N - 50°N generally agrees with the altitude profile of Haverd et al. [53] and lies slightly outside the error bars of the MIPAS-Balloon flight profile obtained at Aire-sur-l'Adour, France (43.7°N) (Figure 33). The MIPAS-Balloon flight profile obtained at Kiruna, Sweden (67.5°N) of $^{16}O^{16}O^{18}O$ and $^{16}O^{18}O^{16}O$ are available only up to ~25 km. Both ACE-FTS $^{16}O^{16}O^{18}O$ and $^{16}O^{18}O^{16}O$ δ value profiles between 20.5 km to 25.5 km lie within the error bars of MIPAS-Balloon flight profile obtained at Kiruna, Sweden [37].

δ $^{50}O_3$ values reported in the Figure 34 were obtained by using δ values calculated from $^{16}O^{18}O^{16}O$ and δ $^{16}O^{16}O^{18}O$ VMRs with the equation δ $^{50}O_3 = (2 \times \delta$ $^{16}O^{16}O^{18}O + \delta$ $^{16}O^{18}O^{16}O)/3$ in order to compare with mass spectrometric measurements. The ACE-FTS altitude profiles of δ $^{50}O_3$ values were calculated for 5 latitude regions. The ACE-FTS mission δ average altitude profiles of $^{50}O_3$ of 5 latitude regions were presented in the Figures 34. Southern polar (90°S - 60°S), Southern mid-latitudes (60°S - 30°S), tropics (30°S - 30°N), northern mid-latitudes (30°N - 60°N) and northern polar (60°N - 90°N) are the 5 latitude regions considered in this analysis. The FIRS measurements are in the far infrared and the line parameters for these rotational transitions may be more reliable than the vibration-rotation line parameters used by the other remote sensing instruments. This type of systematic error has not been included in the quoted error bars. Overall, however, there is good agreement between ACE-FTS values and those of other instruments (Figure 34) [37].

Liang et al. [85] provide predictions of altitude dependent fractionation from their 1-dimentional semi-empirical model. As observed by ACE-FTS and predicted by

Liang et al. [85] the fractionation of the symmetric isotopomers is substantially less than the asymmetric isotopomers. However, Liang et al. [85] predict that fractionation increases with altitude from 20 km to a peak near 35 km for all isotopologues. ACE-FTS altitude profiles vary with latitude but tend to be relatively flat (except for $^{16}O^{17}O^{16}O$) with an increase in fractionation near the top of the observed range above 35 km [37].

6.4 CONCLUSION

The ACE mission has a large ozone isotopologue data set for comparison with atmospheric chemical transport models that include isotopic fractionation. The fractionation with altitude is in general agreement with previous observations, although these observations are quite variable and often do not include error bars. Global distributions of isotopic ozone fractionations are observed for the first time. As expected the largest enrichments are observed in the tropical stratosphere in agreement with ballon-borne measurements. The contribution of photolysis to this fractionation can be seen in the tropics and at high latitudes in the summer. The upper stratosphere of the Antarctic polar vortex also shows enhanced fractionation possibly due to dynamics from descent of air enriched in heavy isotopologues.

CHAPTER 7

TRENDS IN LOW ALTITUDE CO_2 ABUNDANCES

The results and the majority of the material presented in this chapter are published in the Journal of Quantitative Spectroscopy & Radiative Transfer (Bernath et al. [14]). As the first author, P. Bernath wrote the text in the publication, carried out the data analysis collaborating with me and supervised the project. The co-authors of this publication are: me (Old Dominion University), C. Boone (University of Waterloo) and S. Jones (University of Waterloo). C. Boone is the ACE project scientist who carried out retrievals from ACE-FTS, using resources at the University of Waterloo. Calculation of the atmospheric "forward model" to prepare volume mixing ratio profiles for CO_2 was also done by Boone with the help of S. Jones. As a co-author of this publication, preparation of the figures and the data analysis was done by me. This work is original and has not published anywhere prior to the publication in the Journal of Quantitative Spectroscopy & Radiative Transfer.

7.1 INTRODUCTION

CO_2 is a well mixed gas in the Earth's atmosphere that does not precitipate and condense at current atmospheric temperatures. Therefore, CO_2 is the single most important climate-relevant greenhouse gas in the Earth's atmosphere, although the strongest greenhouse gas in the terrestrial atmosphere is water vapor. CO_2 is responsible for 20% of the total terrestrial greenhouse effect with water vapor contributing 50%, clouds 25% and other noncondensible greenhouse gases (CH_4, O_3, N_2O and chlorofluorocarbons) 5% [77]. Water vapor and stratiform clouds provide a strong positive feedback to global warming, initiated by the perturbation of other greenhouse gases. Consider a situation where the Earth's surface temperature increases due to a small increase of CO_2. This rise of temperature will exacerbate water vapor evaporation from oceans and other surface water sources. This added water vapor to the atmosphere will again increase the surface temperature and cause more evaporation from surface water reservoirs. This process can continue until oceans completely evaporate and the surface temperature reaches extremely high values.

Such a runaway greenhouse effect could have happened in ancient Venus, although it is not possible on Earth because evaporated vapor will eventually form clouds and precitipate, making water return to the surface [69]. Since a small increase of CO_2 can result in higher surface temperatures, monitoring anthropogenic CO_2 emissions is important.

Various measurements of atmospheric CO_2 have been made in order to understand Earth's carbon cycle and to improve our knowledge on the global carbon budget. NOAA (National Oceanic and Atmospheric Administration) provides regular CO_2 observations from flask samples, aircraft and tall tower measurements and from *in situ* observations (from observatories like Mauna Loa, Hawaii) [79]. Seasonal upper of tropospheric CO_2 data in the Asia-Pacific region were obtained with high-frequency CONTRAIL (Comprehensive Observation Network for TRace gases by AIrLiner) commercial in-flight measurements [152], general monthly altitude CO_2 measurements were obtained with aircraft projects like CARIBIC (Global Atmospheric Composition and Climate Change Research) [18] and CO_2 vertical profiles were measured with HIAPER (HIAPER Pole-to-Pole observations) aircraft program covering the Pacific region (altitudes 85°N to 67°S) [167]. High-altitude aircraft such as NASA ER-2 observe up to about 21 km and high altitude balloons up to 30 km, using atmospheric sample systems such as AirCore [68].

One of the methods that can be used to monitor global CO_2 is remote sensing from the ground and from orbit. Total Carbon Column Observing Network (TCCON), a global network of ground-based Fourier transform spectrometers was set up to obtain column measurements of important greenhouse gases including CO_2 in the near-infrared region [168]. Global CO_2 column measurements were obtained with an on-orbit grating spectrometer from reflected sunlight known as Orbiting Carbon Observatory-2 (OCO-2) and with a Fourier transform spectrometer known as Greenhouse Gases Observing Satellite (GOSAT) [76].

CO_2 observations were obtained from the instruments, TES (Tropospheric Emission Spectrometer) on the Aura satellite [75], AIRS on the Aqua satellite [22] and IASI on the MetOP three polar-orbiting meteorological satellite system [26]. Similarly, limb sounding instruments such as ACE-FTS (Atmospheric Chemistry Experiment Fourier Transform Spectrometer) [148], MIPAS (Michelson Interferometer for Passive Atmospheric Sounding) and SABER (Sounding of the Atmosphere using Broadband Emission Radiometry) [88] also provide global and vertically resolved

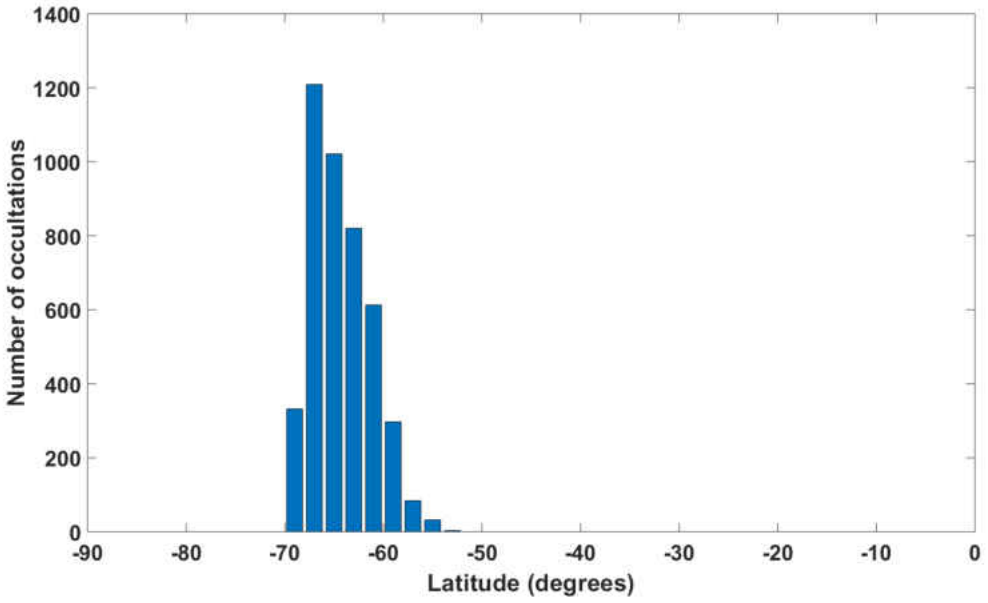

FIG. 35: Latitude distribution of May occulations in the Southern Hemisphere for 2004-2017 (Figure was taken from Bernath et al. [14])

CO_2 data.

CO_2 measurements are widely used to validate transport models and to determine the stratospheric age-of-air [126, 79, 65]. CO_2 is an excellent tracer of atmospheric dynamics since it is a well-mixed gas in the atmosphere and has a long atmospheric lifetime.

7.2 RESULTS AND ANALYSIS

ACE-FTS V.4.0 processing product provided CO_2 VMR altitude profiles (from 5.5 km to 17.5 km) for the month of May and for the period 2004 - 2017 that covers a compact region in the Southern Hemisphere. The latitudes that cover the occultations of this data product were shown in the Figure 35 using 2° latitude bins. Since 14 years worth of data are available for the month of May, a study is permitted to explore CO_2 trends in the latitude region 55°S - 70°S, in a period where the polar vortex has not formed. The polar vortex forms during the winter and during that time period tropospheric and lower stratsopheric air can be subjected to extremely cold temperatures. Cold temperatures can sink high altitude air to lower altitudes and hence it would be difficult to spatially resolve the atmosphere [14].

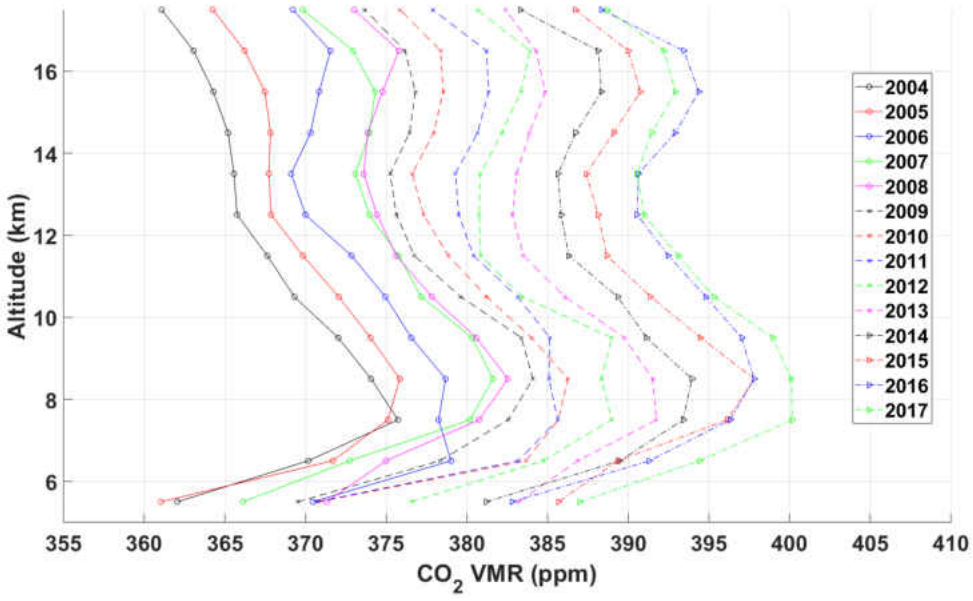

FIG. 36: Average altitude profiles for CO_2 VMRs for each May from 2004-2017 for 55°S - 70°S (Figure was taken from Bernath et al. [14])

ACE-FTS V.4.0 data were used to calculate individual annual altitude profiles for the month of May and time series of the altitudes 7.5 km, 9.5 km, 10.5 km and 12.5 km representing the troposphere and the lower stratosphere. Large altitude gaps are the result of data loss when downloading data from the satellite to produce the ACE-FTS V.4.0 data product. Therefore, ACE-FTS V.4.0 contains unphysical values for several occultations. In order to filter out these unphysical data from the analysis, large positive and negative values were removed from the data set. To further remove outliers from data, before calculating time series for each altitude level, values that were more than 2 standard deviations away from the altitude mission averages were discarded. Similarly, to calculate annual altitude profiles, data that were more than 2 standard deviations away from the annual altitude mission averages were also discarded (4% of data were lost during the filtering process) [14].

Average annual altitude profiles of CO_2 are presented in the Figure 36 for each May and for 2004 - 2017 at 55°S - 70°S. The average annual altitude profile of CO_2 VMRs (with one standard deviation) of May 2017 is presented in the Figure 37 along with an average temperature profile (with one standard deviation). The standard deviation at each altitude of these profiles is about 1.5% (∼6ppm) and the typical

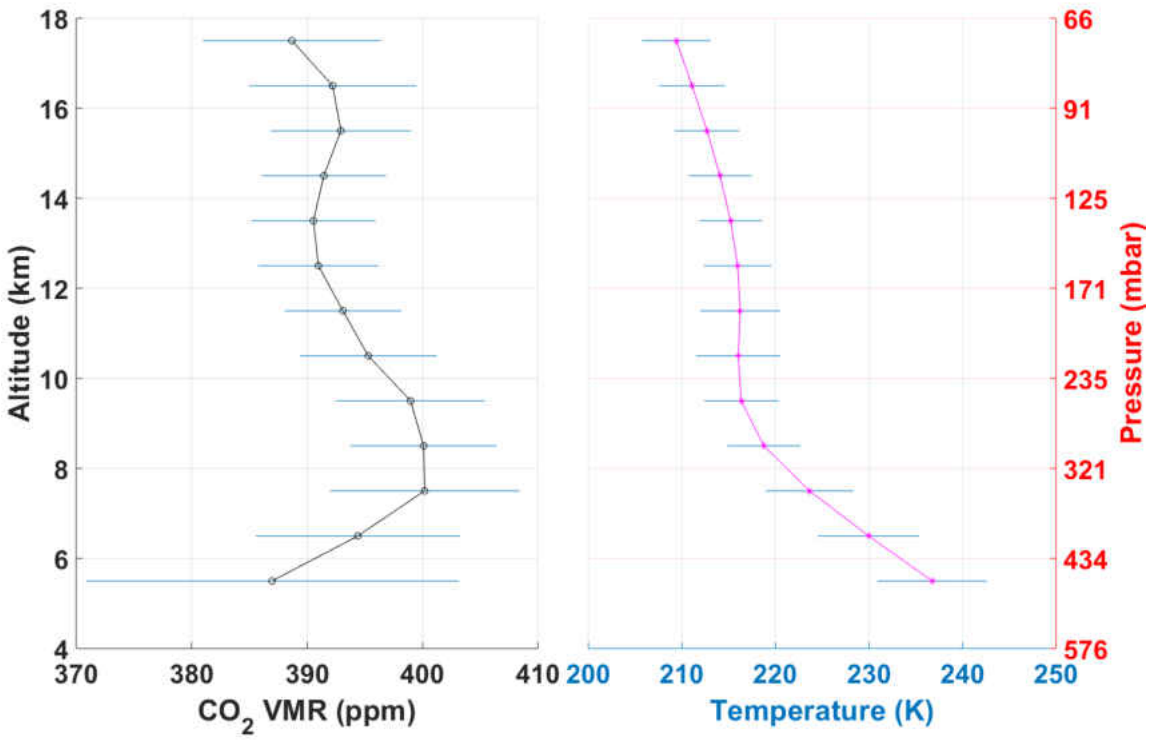

FIG. 37: CO_2 altitude profile (left panel) and temperature (right panel) for May 2017 with one standard deviation error bars for the 55°S - 70°S region. The average atmospheric pressure is given on the far right in mbar (hPa) (Figure was taken from Bernath et al. [14])

statistical error estimated from least squares analysis for a calculated individual average is about 2.5% (∼10 ppm). ACE-FTS annual altitude CO_2 profiles were compared with corresponding altitude profiles from an *a priori* empirical model provided by G. Toon. The *a priori* empirical model covers the troposphere and stratosphere; and has currently been used to generate *a priori* CO_2 profiles for the TCCON (Total Carbon Column Observing Network) of ground-based Fourier transform spectrometers. Average annual altitude CO_2 profiles calculated from the model were presented in Figure 38. These *a priori* values were calculated for each ACE-FTS occultation and for this study, the data of the month of May were averaged to obtain Figure 38 [14].

CarbonTracker [115] (CT2017; http://carbontracker.noaa.gov) is a global CO_2 model that uses observations from hundreds of sites around the world and performs calculations by forecasting CO_2 mole fractions from CO_2 surface exchange

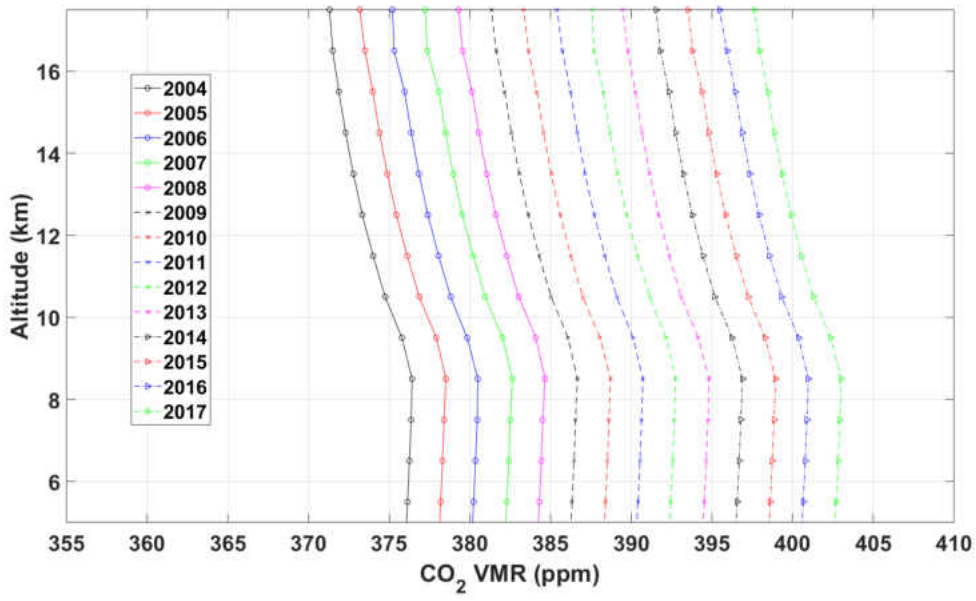

FIG. 38: CO_2 altitude profiles for each May 2004 - 2017 for 55°S - 70°S from Toon's empirical model, assuming a 9 km tropopause altitude. (Figure was taken from Bernath et al. [14])

models driven by meteorological fields from the European Centre for Medium-Range Weather Forecasts (ECMWF). The calculated 3-D CO_2 distribution is compared with the available observations and the difference is minimized to get optimal values. CarbonTracker utilizes CO_2 measurements provided by NOAA, tall towers, aircraft campaigns, shipboard measurements, CONTRAIL [152] and AirCore [68] as the GLOBALVIEW + data product. In order to validate ACE-FTS CO_2 observations, CT2017 predictions at the altitudes 5.3 km, 6.5 km, 7.7 km, 9.1 km, 10.6 km, 12.2 km, 13.9 km and 15.8 km within the 5-18 km range have been used for the month of May (2004–2016) from the CT2017 website (`http://carbontracker.noaa.gov`). CO_2 VMR averages were calculated for all the longitudes and the latitudes between 55°S - 70°S for 9 altitude levels (5.3 km to 18 km range); and the calculated average altitude profiles are presented in the Figure 39 [14].

7.3 DISCUSSION

CO_2 average altitude profiles of ACE-FTS (Figure 36), Toon's model (Figure 38) and CarbonTracker (Figure 39) are in general agreement within the error bars of the CO_2 annual altitude profile of year 2017, presented in the Figure 37. Tropopause is

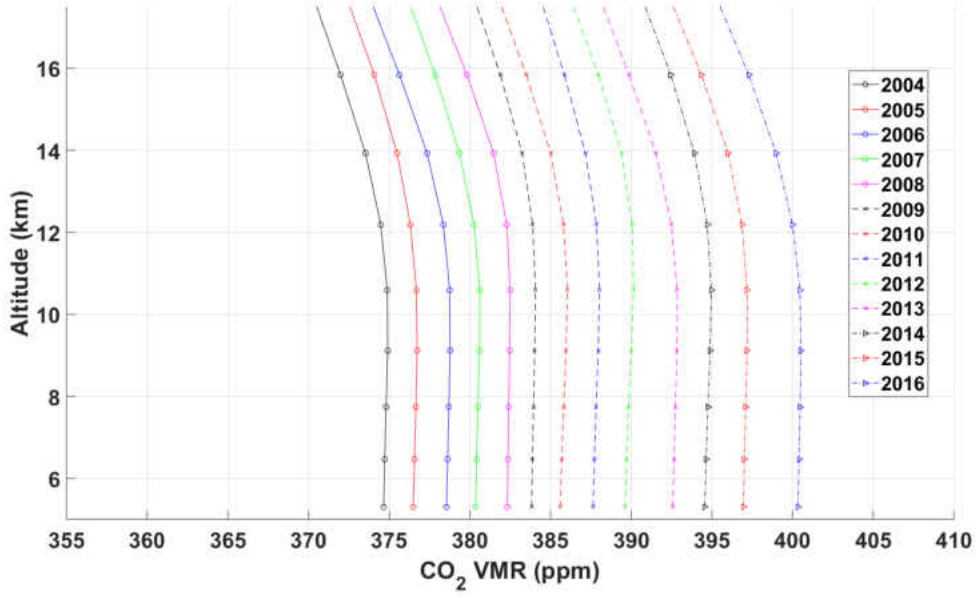

FIG. 39: CO_2 altitude profiles from CarbonTracker 2017. (Figure was taken from Bernath et al. [14])

the boundary that separates the stratosphere and troposphere; and the tropopause height between the latitudes 55°S - 70°S is about 9.5 km. The ACE-FTS CO_2 VMR average values at 5.5 km and 6.5 km has a clear low bias compared to the CarbonTracker and Toon's model values. The technical errors occurred when tangent heights were determined using N_2 continuum and when retrieving CO_2 VMRs with chosen microwindows might have caused this low bias. The ACE-FTS CO_2 VMRs in the stratosphere decrease rapidly compared to CarbonTracker and Toon's model values. There is a peak near 15.5 km in the ACE-FTS VMR profiles and to verify whether it is an artifact or real, the behavior of other molecules around the altitude 15.5 km should be investigated [14].

Macquarie Island is an uninhabited and small island located between New Zealand and Antarctica (54°37′ S, 158°52′ E) and the location of the island falls within the altitude range considered in this study. Continuous CO_2 measurements obtained from 2005 to 2016 and 13 m above sea level by Australia's Commonwealth Scientific and Industrial Research Organisation (CSIRO) with a well calibrated non-dispersive infrared spectrometer were used to compare with ACE-FTS data. Since numerical data of the CO_2 time series obtained at Macquarie Island were not provided, data

TABLE 9: Linear trends of ACE-FTS CO_2 for altitude levels (Table was taken from Bernath et al. [14])

Altitude (km)	Linear trend (ppm/yr)	σ (ppm/yr)
5.5	1.9	0.2
6.5	1.8	0.1
7.5	1.93	0.07
8.5	1.96	0.08
9.5	1.98	0.06
10.5	1.91	0.06
11.5	1.89	0.08
12.5	1.95	0.05
13.5	1.97	0.05
14.5	2.09	0.06
15.5	2.27	0.07
16.5	2.23	0.09
17.5	2.13	0.08

were extracted from the Figure 10a in Stavert et al. [144]. NOAA also provided ground based CO_2 VMR measurements at South Pole and at the altitude 2.84 km for each May from 2005 to 2016 (data received through private communication). The ACE-FTS time series for 13 altitude levels (5 km to 18 km) on a 1 km grid were fitted using weighted linear regression and calculated trend values with standard errors for 2004 - 2017 were given in Table 9. The CO_2 trend values seem to slowly increase with the altitude and standard errors generally show constant values after 6.5 km (systematic errors were not estimated) [14].

ACE-FTS time series (with one standard deviation error bars) were compared with CarbonTracker data at the altitudes 7.5 km, 9.5 km, 10.5 km and 12.5 km and CT2017 time series were calculated with one standard deviation error bars at 7.7 km, 9.1 km, 10.6 km, 13.9 km (Figures 40, 41, 42, 43). Toon's model data and data obtained at Macquarie Island by Stavert et al. [144] were also plotted with error bars at relevant altitudes. Trend values of each particular time series is given in the

TABLE 10: Linear trends of ACE-FTS CO_2 for altitude levels (values are from Bernath et al. [14])

Data	Linear trend (ppm/yr)	σ (ppm/yr)
Macquarie Island	2.06	0.05
Carbon Tracker	1.8	0.1
Toon's model	2.04	0.05
South Pole (NOAA)	2.2	0.1

Table 10. In general, ACE-FTS trend values agree with trends calculated by NOAA (South Pole), from Toon's model, with CT2017 and at Macquarie Island within two standard deviations. Note that although Toon's model and CT2017 provide time series for the altitudes 7.5 km, 9.5 km, 10.5 km and 12.5 km their trend values are the same (Table 10) [14].

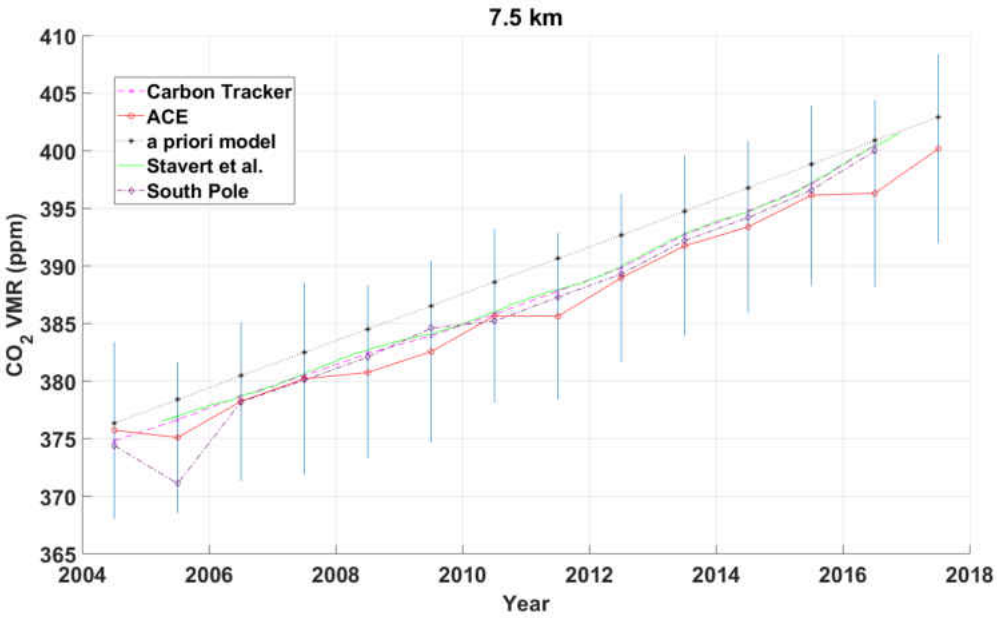

FIG. 40: Trend comparisons at 7.5 km. (Figure was taken from Bernath et al. [14])

7.4 CONCLUSION

Since ACE-FTS measurements cover many parts of the Earth's atmosphere

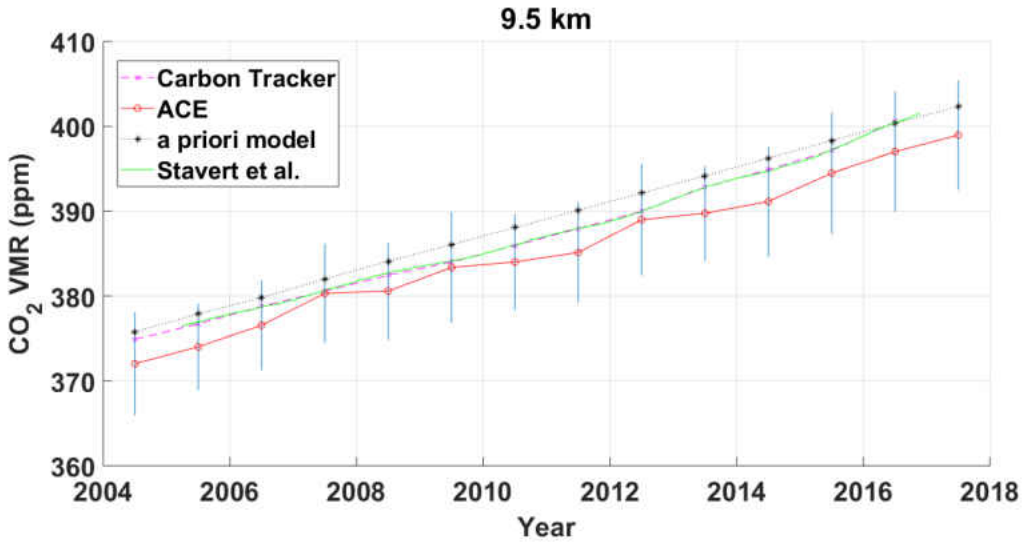

FIG. 41: Trend comparisons at 9.5 km. (Figure was taken from Bernath et al. [14])

(Southern Ocean, upper troposphere and lower stratosphere), they can be useful for carbon cycle science. Although ACE-FTS CO_2 trend values are in good agreement with CarbonTracker, Toon's empirical model and South Pole data from NOAA, at the altitudes 5.5 km and 6.5 km ACE-FTS CO_2 VMRs are lower and decrease rapidly compared to the CarbonTracker and Toon's empirical model values. This study was done with a preliminary ACE-FTS product and data were only available in the latitude region 55°S - 70°S. Since the data product looks promising in its initial evaluation, a global evaluation is needed to see if it can be assimilated into models such as CarbonTracker.

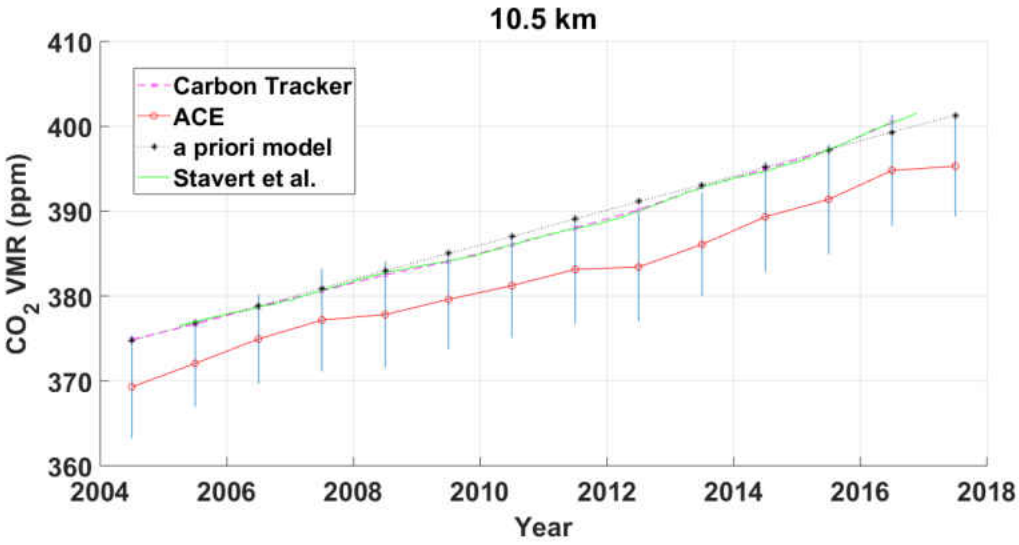

FIG. 42: Trend comparisons at 10.5 km. (Figure was taken from Bernath et al. [14])

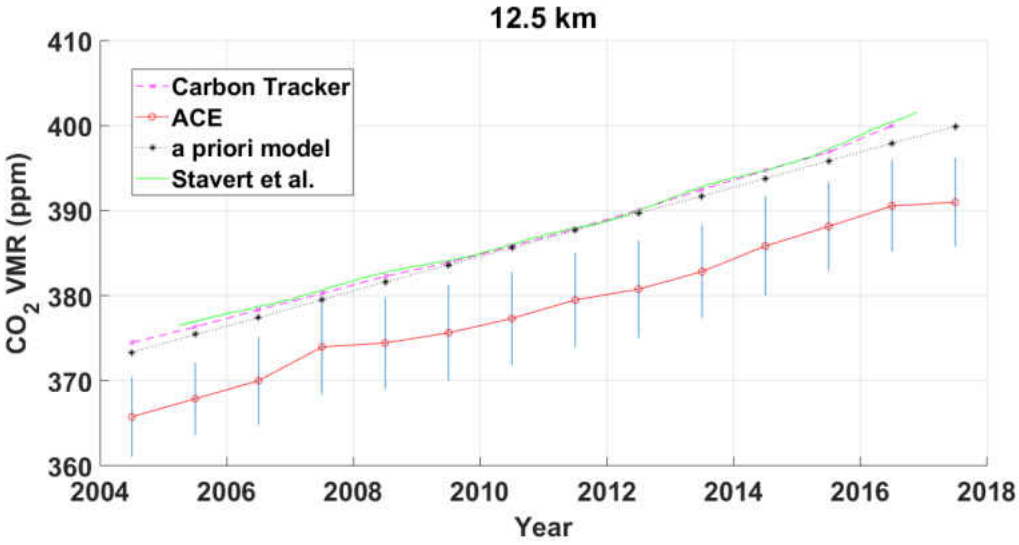

FIG. 43: Trend comparisons at 12.5 km. (Figure was taken from Bernath et al. [14])

CHAPTER 8

TRENDS IN ATMOSPHERIC HCl, HFC-23 (CHF_3) AND HFC-134A ABUNDANCES

The results and the majority of the material presented in this chapter are published in the Journal of Quantitative Spectroscopy & Radiative Transfer (Bernath and Fernando [12] and Fernando et al. [38]). The trend results of the atmospheric molecules HFC-23 and HFC-134a are included in the publication Fernando et al. [38]. As the first author of Fernando et al. [38] analysis of HFC-23 (CHF_3) and HFC-134a data, preparation of figures and writing the text were carried out by me. The co-authors of Fernando et al. [38] are: P. Bernath (Old Dominion University) and C. Boone (University of Waterloo). C. Boone is the ACE project scientist who carried out retrievals from ACE-FTS, using resources at the University of Waterloo. Calculation of the atmospheric "forward model" to prepare volume mixing ratio profiles for HFC-23 (CHF_3) and HFC-134a was also done by Boone. P. Bernath is the mission scientist for ACE and the advisor of this project.

The trend results of atmospheric HCl are included in the publication Bernath and Fernando [12]. As the first author of Bernath and Fernando [12], P. Bernath wrote the text, carried out the data analysis collaborating with me and supervised the project. As the only co-author of the publication, preparation of the figures was done by me.

This work is original and was not published anywhere prior to the publication in the Journal of Quantitative Spectroscopy & Radiative Transfer.

8.1 INTRODUCTION

In 1974, Rowland and Molina [130] discovered that long-lived chlorofluorocarbons (CFCs) released by humans destroy stratospheric ozone. Anthropogenic chlorofluorocarbons and halons known as ozone depleting substances (ODSs), are non-reactive in the troposphere and photolyzed in the stratosphere to release chlorine and bromine atoms [130]. These chlorine (and bromine) atoms trigger a catalytic loss mechanism (Reaction 58) with the ClO free radical to deplete stratospheric ozone that prevents

harmful ultra-violet radiation (200 - 300 nm) reaching the surface of the Earth. Antarctic ozone depletion depends on the inorganic chlorine (Cl_y) produced by these ODSs and cold temperatures in the Antarctic vortex. Short-lived species such as Cl, ClO, and HOCl and long-lived species like HCl and $ClONO_2$ are called inorganic chlorine. Ultimately, CFCs are oxidized to CO_2, HF and HCl [12]. Therefore, emissions of Cl containing ozone depleting substances can be monitored by measuring stratospheric HCl concentrations [63].

$$Cl + O_3 \longrightarrow ClO + O_2 \tag{58a}$$

$$ClO + O_3 \longrightarrow Cl + O_2 \tag{58b}$$

$$\text{net: } O_3 + O \longrightarrow 2O_2 \tag{58c}$$

This catalytic cycle (Reaction 58) is terminated with the conversion of ClO and Cl (ClO_x) to non-reactive HCl and $ClNO_3$ reservoirs (Reaction 59). The sum of ClO_x, HCl and $ClNO_3$ reservoirs are defined as Cl_y)

$$Cl + CH_4 \longrightarrow HCl + CH_3 \tag{59a}$$

$$ClO + NO_2 + M \longrightarrow ClNO_3 + M \tag{59b}$$

The lifetime of HCl is a few weeks and the lifetime of $ClNO_3$ is typically a day; and utimately these reservoirs return to ClO_x,

$$HCl + OH \longrightarrow Cl + H_2O \tag{60a}$$

$$ClNO_3 + h\nu \longrightarrow Cl + NO_3 \tag{60b}$$

In situ balloonborne measurements provide altitude information on HCl concentrations with SPIRALE (a French acronym for infrared absorption spectroscopy by tunable diode lasers) spectrometer [104]. HCl vertical profiles were measured remotely with the solar occultation method by the Jet Propulsion lab MkIV interferometer [150]. Near-global HCl time series were calculated from the observations made with the HALOE (Halogen Occultation Experiment) instrument on the NASA's Upper Atmosphere Research Satellite (UARS) from 1991 to 2005 [4]. Most

recent HCl extensive observations were made by the Canadian Atmospheric Chemistry Experiment Fourier Transform Spectrometer (ACE-FTS) [11] on SCISAT and the Microwave Limb Sounder (MLS) on the NASA's Aura satellite [158].

Froidevaux et al. [41] provide a data product called GOZCARDS (Global OZone Chemistry And Related trace gas Data records for the Stratosphere), merging stratospheric data from the instruments HALOE, MLS (Microwave Limb Sounder) and ACE-FTS for 1997 - 2010. Brown et al. [20] used tropical ACE-FTS measurements to provide time series (2004 - 2010) and vertical profiles of HCl VMRs. HCl trends values were also reported in WMO ozone assessments every 4 years as well [2].

ACE-FTS HCl trend values are affected by dynamical variability. As an example ground-based and satellite data showed a significant increase of the HCl reservoir in the lower stratosphere of the Northern Hemisphere since 2007 [92]; this is in contrast with the monotonic decrease of HCl source gases mainly due to the success of Montreal Protocol. Model simulations attributed this increase to the slowdown in the Northern Hemisphere atmospheric circulation that transports aged-air to the lower atmosphere [92]. This dynamical variability on HCl trends can be removed by using the correlation with N_2O which is a long-lived tracer [145, 12].

8.1.1 ANTARCTIC OZONE HOLE

In 1985, the British Antarctic Survey discovered that ozone columns over Halley Bay, Antarctica had decreased precipitously by more than 40% between 1977 and 1984, during Spring months (September-November) [127] and no depletion was observed in other seasons. Later, global satellite data confirmed this discovery and also showed that the ozone depletion extended roughly 12 to 24 km in altitude, covering much of the lower stratosphere. This was later identified as the ozone "hole" in the Southern polar atmosphere [127]. The ozone columns had declined since 1985 (Figure 44a) and the measured ozone partial pressure altitude profile obtained by British Antarctic Survey station at Halley Bay, Antarctica 76° in October, between 1957-1992 is shown in Figure 44b.

8.1.2 MECHANISM OF OZONE LOSS

The discovery of the ozone hole shocked the world because the atmospheric ozone absorbs ultraviolet radiation that is harmful for humans and the Earth's biosphere. In 1980s, measurements taken from several aircraft missions discovered that ozone

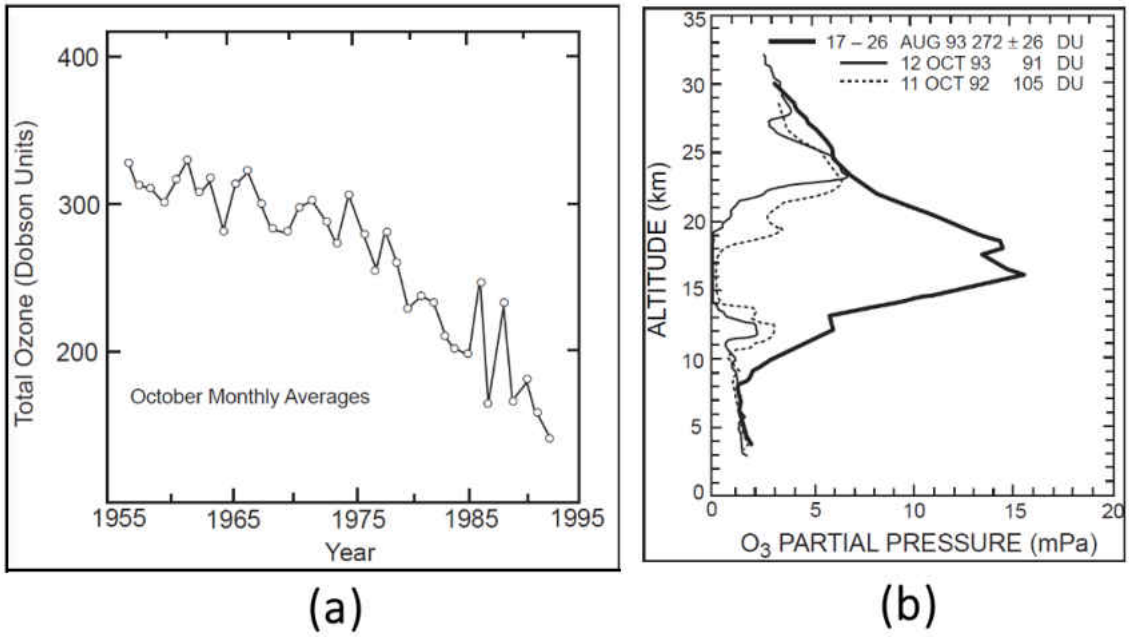

FIG. 44: (a) Historical trend in the total ozone column measured spectroscopically over Halley Bay, Antarctica in October, 1957-1992. One Dobson unit (DU) represents a 0.01 mm thick layer of ozone under standard conditions of temperature and pressure; 1 DU = 2.69×10^{16} molecules cm^{-2} [164]. (b) Vertical profiles of ozone over Antarctica measured by chemical sondes. In August the ozone hole has not developed yet, while in October it is fully developed [165].

depletion is associated with high ClO concentrations. In the meantime, laboratory experiments also confirmed that O_3 depletion occurs due to a catalytic reaction cycle involving ClO (Reaction 61) [63].

$$ClO + ClO + M \longrightarrow ClOOCl + M \tag{61a}$$

$$ClOOCl + h\nu \longrightarrow ClOO + Cl \tag{61b}$$

$$ClOO + M \longrightarrow Cl + O_2 \tag{61c}$$

$$2\times(Cl + O_3 \longrightarrow ClO + O_2) \tag{61d}$$

$$\text{net: } 2O_3 \longrightarrow 3O_2 \tag{61e}$$

The reaction of Br radicals with ozone also contributes to the ozone depletion (Reaction 62) [63]. According to model calculations, the ClO reaction cycle accounts for

70% of the Antarctic ozone depletion and the BrO + ClO radical cycle is responsible for the remaining 30% [63].

$$Cl + O_3 \longrightarrow ClO + O_2 \tag{62a}$$

$$Br + O_3 \longrightarrow BrO + O_2 \tag{62b}$$

$$BrO + ClO \longrightarrow Br + Cl + O_2 \tag{62c}$$

8.1.3 HFCS AND HCFCS

The Montreal Protocol is an international treaty signed to regulate the production and use of substances such as chlorofluorocarbons (CFCs) and halons that were mainly used for refrigeration, air-conditioning applications and aerosol propellants. These gases cause the depletion stratospheric ozone, and that are potent greenhouse gases [34, 130]. Initially, this agreement was signed by 46 countries and currently around 200 nations have been joined the agreement to protect the ozone layer. At first, the production of several CFCs and halons were phased out [3] that effectively destroy large numbers of stratospheric ozone molecules [38].

As a temporary substitute for CFCs, hydrochlorofluorocarbons such as $CHClF_2$ (HCFC-22) were introduced because they have shorter atmospheric lifetimes and hence smaller ozone depleting potentials (ODPs) than CFCs [125]. Later, hydrochlorofluorocarbons (HCFCs) were also phased out, since HCFCs also contain chlorine and can still destroy stratospheric ozone. HCFCs for dispersive use are now essentially phased out in developed countries but are still produced in developing countries [38].

Hydrofluorocarbons (HFCs) such as CF_3CFH_2 (HFC-134a) have been introduced to replace CFCs and HCFCs because they contain no chlorine and have very small ODPs [2, 107]. Although the HFCs do not directly contribute to the depletion of stratospheric ozone they are potent greenhouse gases. These HFCs have relatively long atmospheric lifetimes and are rapidly accumulating in the atmosphere [155]. HFCs are projected to make a significant contribution to global warming [156, 38].

The Montreal Protocol was amended in Kigali, Rwanda in 2016 to phase out long-lived HFCs. The goal of the Kigali amendment is to gradually decrease global HFC use by 80 - 85% by the late 2040s. First HFC reductions will come into effect in

developed countries in 2019, and by 2024 most of the developing countries will also start to freeze HFC consumption [3, 61, 153, 38].

HFC-134a is a CFC-12 replacement in domestic, commercial and automotive air conditioning applications [169, 112]. HFC-134a contributes more than half of all HFC emissions associated with CFC replacements and has a Global Warming Potential (GWP) of 1430 (100-yr) [106]. The main atmospheric sink for HFC-134a is the reaction with tropospheric OH and as a result the lifetime of HFC-134a is 13.4 years [107, 106]. Photolysis in the stratosphere is typically not an important sink for HFCs as their absorption cross sections are negligible in the range of stratospheric UV radiation [71]. Since 2000, HFC-134a has been the most abundant HFC in the atmosphere [52, 38].

The HFC-23 (CHF_3) is not directly produced as a CFC replacement, but as a byproduct of HCFC-22 production, by over-fluorinating $CHCl_3$ (chloroform). Small amounts of HFC-23 are also used as a raw material for Halon-1301 ($CBrF_3$), as a low temperature refrigerant, in fire extinguishers and in the semiconductor industry [111]. The atmospheric lifetime of HFC-23 is 222 years and the GWP is 12,400 (100-yr) [106, 38].

Measuring HFC-23 and HFC-134a abundances and trends is useful for monitoring the Kigali amendment. The global distributions and trends of HFC-134a and HFC-23 based on ACE-FTS satellite measurements were determined in this study [38].

8.2 METHOD AND DISCUSSION OF HCl CALCULATIONS

The ACE-FTS HCl data is available for altitudes 6.5 km to 67.5 km on a 1 km grid with a vertical resolution about 3 km. In order to stay consistent with a trend analysis done by Stolarski et al. [145] on HCl with GOZCARDS [41], ACE-FTS VMRs for 60°S - 60°N were interpolated onto a pressure grid spaced at $p_i = 1000\times10^{-i/6}$ (hPa). Initially large positive and negative values and VMRs that were 2.5 standard deviations away from the median at each pressure level were removed from the data set. In order to make a time series for Mar-May 2004 to Sep-Nov 2017 quarterly averages were computed for Dec–Feb (DJF), Mar–May (MAM), Jun–Aug (JJA) and Sep–Nov (SON) at each pressure level. These time series calculated for each pressure level were affected by seasonal fluctuations (quarterly) and it is useful to remove them (de-seasonalize) before performing a statistical analysis. The time series at each pressure level were de-seasonalized by calculating quarterly averages

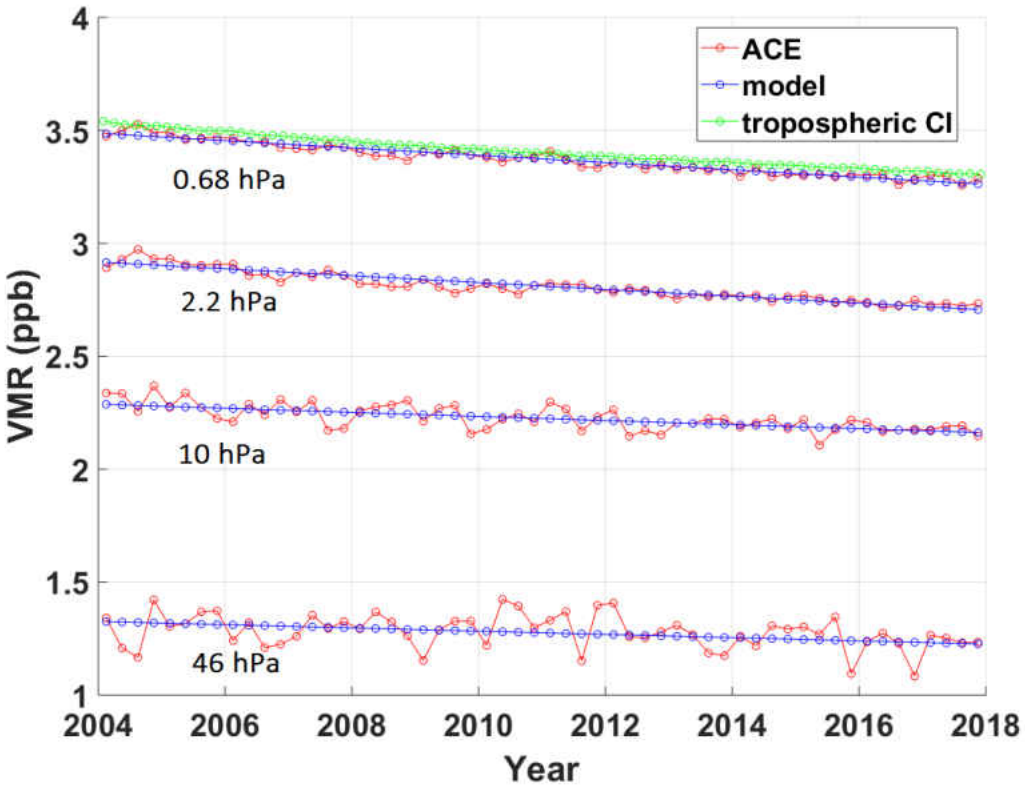

FIG. 45: Quarterly averages were then computed for Dec–Feb (DJF), Mar–May (MAM), Jun–Aug (JJA), Sep–Nov (SON) at each pressure level to make a time series for MAM 2004 to SON 2017.De-seasonalized HCl VMR time series from ACE-FTS data for 60°S - 60°N and the total effective tropospheric chlorine lagged by 4 years. The blue lines are linear fits. Figure was taken from Bernath and Fernando [12].

for all annual data and subtracting them from the corresponding quarter to obtain a time series of "anomalies". In order to obtain a VMR time series for HCl, these anomalies were converted back to a de-seasonalized VMR time series (Equation 63) by adding the 2004-2017 averages for each pressure level [12].

$$\mathrm{VMR}_{\mathrm{HCl(t)}} = a + b\mathrm{t} + c\mathrm{VMR}_{\mathrm{N2O(t)}} \tag{63}$$

(a,b and c are constants to be determined)

ACE-FTS HCl times series calculated for pressure levels 0.68, 2.2, 10, 46 hPa are shown in Figure 45 to represent the mid and upper stratosphere. The approximate

altitudes for these pressure levels are 51, 42, 31 and 21 km, respectively, and these altitudes were estimated using the US standard atmosphere [1]. Linear trend lines are also plotted for each pressure level presented in the Figure 45. Total effective tropospheric chlorine was also plotted lagged by 4 years since it takes almost 4 years for tropospheric air to get to the stratosphere [102].

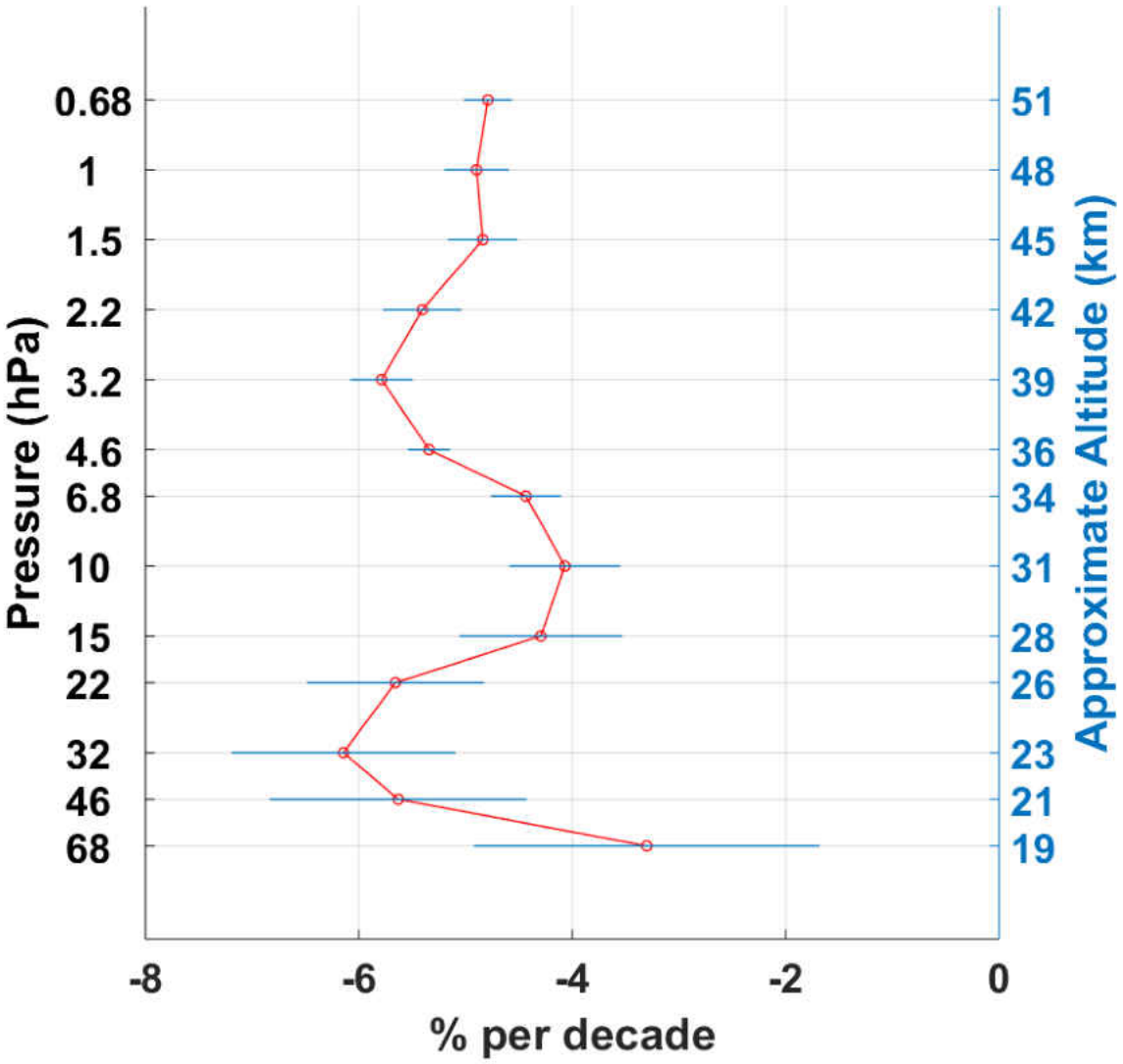

FIG. 46: Linear HCl trends as a function of pressure (approximate altitudes are on the right) for 2004 to 2017 for 60°S - 60°N with one standard deviation error bars. Figure was taken from Bernath and Fernando [12].

ACE-FTS HCl linear trends were calculated for 13 pressure levels from 68 hPa

to 0.68 Pa (about 19 - 51 km) for 60°N - 60°N, using linear regression for the de-seasonalized time series. The calculated linear trends are shown in the Figure 46 with one standard deviation error bars. The linear regression model (Equation 63) used to calculate the trends is consists of a constant, a linear term and a term for the N_2O VMRs (as in ref. [145]). N_2O term in the regression model is supposed to account for HCl variability due to dynamics and hence reduce the error of the trend value, b. The de-seasonalized N_2O time series were prepared similarly to the HCl anomaly time series was corrected for +0.28%/year trend before inclusion in the regression model [145]. Trend error of b was estimated using the procedure specified by Weatherhead et al. [159] that includes the first order autocorrelation effect. The standard error of the trend b is given by the formula $\sigma_N n^{-3/2}[(1+\phi)/(1-\phi)]^{1/2}$, in which σ_N is the standard deviation of the residuals (difference between the observed and the modeled HCl VMRs values), ϕ is the autocorrelation of the residuals and n is the number of years in the data [159].

The average trend, -4.8±0.2% per decade was calculated by averaging 3 values (from 1.5 hPa to 0.68 hPa) representing the upper stratosphere and the error was calculated using error propogation (square root of the sum of the square of the original errors). Similarly, a trend value was calculated for mid-upper stratosphere by averaging trends of all the 13 pressure levels and it was -5.0±0.8% per decade. Percentage trend values were obtained by dividing the linear trends by the mission average of the original time series [12].

The stratospheric trend values reported by 2014 WMO ozone report for 1997-2013 is -5.9±1.5% per decade [2] based on combined HALOE and ACE-FTS. Brown et al. [20] reported a HCl trend value of -7±1% per decade from ACE-FTS and -6±1% per decade from the SLIMCAT model. At 15 hPa, MLS gives a trend value of HCl of -5.0±0.4% per decade which agrees with ACE-FTS trend values. Although GOZCARDS [41] shows similar values compared to ACE-FTS trends, recent trend VMR values show a decrease [12].

ACE-FTS HCl VMR time series show a change in slope since 2010. As example, at 0.68 hPa, the linear trend from 2004 to 2010 is -5.9±0.5% per decade and from 2011 to 2017 is -4.1±0.4% per decade, with an overall linear trend of -4.8±0.2% per decade for 2004-2017. Tropospheric chlorine time series calculated, lagged by 4 years to match the age of air of the upper stratosphere [102] gives a trend value of -4.0±0.1% per decade for 2004-2010 (shown in the Figure 45). There is an excellent correlation of

0.86 and an excellent agreement with the trend values between tropospheric chlorine and ACE-FTS VMR time series. The change in the slopes of HCl time series at 2010 can be attributed to the rapid decline of species with shorter atmospheric lifetimes such as methyl chloroform (https://www.esrl.noaa.gov/gmd/odgi/) [12]. The column density trend values were also looked at by 16 NDACC sites and for 2000-2009, the average trend over all sites was -8% [72]. Recently a total Cl_y (mainly HCl) column trend was calculated by NDACC as -5.0±1.5% per decade that agrees with ACE-FTS trend [27].

8.3 METHOD AND DISCUSSION OF HFC CALCULATIONS

The ACE-FTS altitude profiles of HFC-134a and HFC-23 VMRs were filtered to remove outliers. All negative and large positive values were removed from the data for each altitude and values that were more than 2 standard deviations away from the mission averages were also discarded. This filtering removed 4% of the HFC-134a data and 1% of the CHF_3 data.

Figures 49 and 50 represent the annual mission average altitude profiles covering all the latitudes of CHF_3 and HFC-134a VMRs from 2004 to 2018 (only January and February data are available for 2018). Figure 49 shows that CHF_3 VMR altitude profiles increase steadily at 1 - 2 ppt per year, except between 2005 - 2006 and 2016 - 2017. Figure 50 shows that HFC-134a annual altitude profiles increase by 3 - 4 ppt per year, approximately at a steady rate. The HFC-134a annual altitude profiles (Figure 50) display an unexplained glitch at 9.5 km. It is unphysical for the VMR to be consistently low at a constant altitude of 9.5 km so there is problem in the retrieval. Figure 51 represents the ACE-FTS average altitude profiles of HFC-134a and CHF_3 VMRs for 2017. The percentage standard error of the annual altitude profiles of CHF_3 averages are around 30 - 40% and for HFC-134a are around 50 - 60% (similar to Figure 51). There are two years (2007 and 2011) for which anomalous increases are noted in the HFC-134a annual altitude profiles. This anomalous change lies within the uncertainties of the annual VMR averages and may not be real.

The Advanced Global Atmospheric Gases Experiment with Gas Chromatography with Mass Spectrometry (AGAGE GC-MS) system is used to measure concentrations of atmospheric species such as HCFCs and HFCs that are important for the Montreal Protocol. These gases are analyzed at AGAGE remote sites with a gas chromotograph-mass spectrometer (GC-MS) to obtain VMRs and are used to

estimate global monthly VMR averages [135, 119, 120].

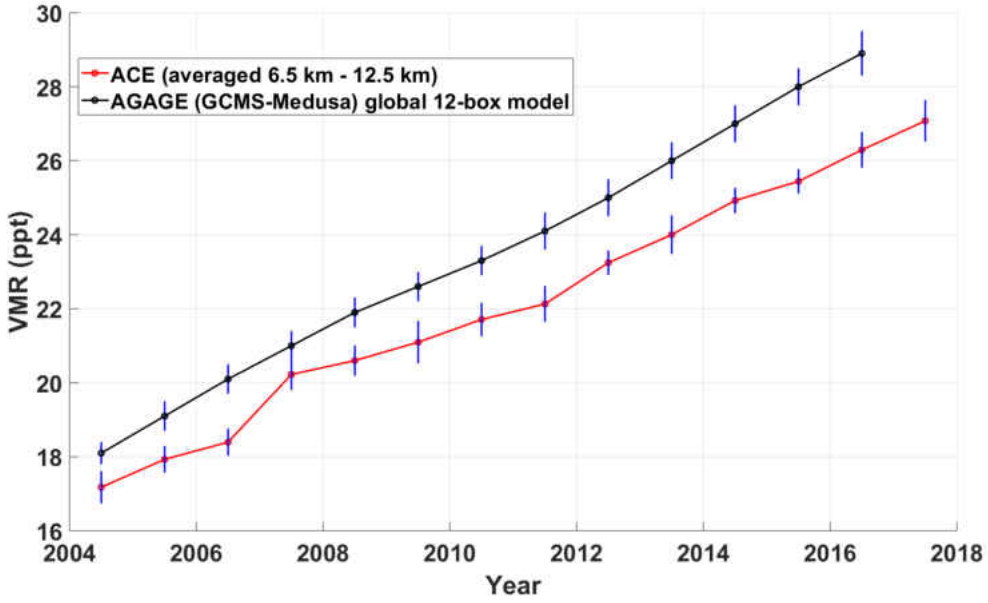

FIG. 47: ACE-FTS CHF_3 annual time series (60°S - 60°N) comparison with AGAGE 12 box model data from Simmonds et al. [135] and AGAGE global mean baseline GCMS-Medusa data from the AGAGE website

Figure 47 represents the overall mission annual average time series of CHF_3 for 60°S - 60°N along with AGAGE 12-box model values obtained from Simmonds et al. [135] (Simmonds et al. [135] provide data only up to 2016.) The 12-box model determines annual VMR values for CHF_3 assuming that the atmosphere consists of four zonal regions (90°S - 30°S, 30°S - 0°S, 0°N - 30°N and 30°N - 90°N) and at vertical heights of 500 and 200 hPa. These modelled VMRs were adjusted by comparison with the atmospheric observations of Simmonds et al. [135]. The Scientific Assessment of Ozone Depletion: 2018 provides annual mole fractions for 2012, 2015 and 2016 with a change of the mole fractions per year of CHF_3. For CHF_3 global mole fraction values (calculated from AGAGE in situ global measurements) were 24.9 ppt for 2012, 28.1 ppt for 2015 and 28.9 ppt for 2016 and, the annual mole fraction change is reported as 0.8 ppt yr^{-1} (2.9% yr^{-1}) for the period 2015 - 2016 [166]. These reported values are reasonably consistent with the calculated ACE-FTS values of 23.2±0.3 ppt for 2012, 25.4±0.3 ppt for 2015, 26.3±0.5 ppt for 2016 and the ACE trend of 0.9 ppt (3.2 %) yr^{-1} for the period 2015 - 2016.

Figure 48 represents overall mission average annual time series of HFC-134a for

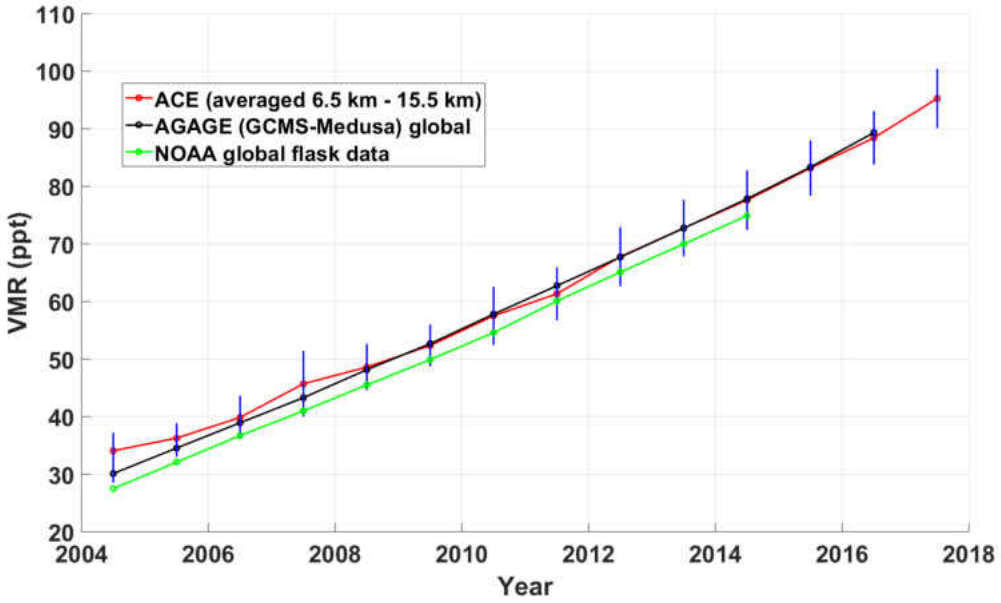

FIG. 48: ACE-FTS HFC-134a annual time series (60°S - 60°N) comparison with AGAGE global mean baseline GCMS-Medusa data from the AGAGE website and NOAA global flask data from Montzka et al. [103]

60°S - 60°N along with the HFC-134a annual time series obtained from the monthly global mean of baseline HFC-134a AGAGE GCMS-Medusa data available at the AGAGE website from 2004 - 2016 [90]. Montzka et al. [103] have also published global mean VMRs for HFC-134a based on NOAA sampling data and they are plotted in Figure 48.

Since HFC-134a VMRs start to decrease significantly above 15.5 km, HFC-134a VMRs were considered only up to 15.5 km and the lower limit of the altitude range was chosen to be 6.5 km. The trend values were based on the unweighted annual average of all VMR bins between 6.5 and 15.5 km. The linear trend of the ACE-FTS HFC-134a time series is 4.9±0.1 ppt per year. For AGAGE GCMS HFC-134a monthly data, annual means were calculated for both VMRs and their errors and then a weighted linear trend was calculated. The calculated linear trend for the AGAGE HFC-134a time series is 4.87±0.05 ppt per year. The calculated linear trend for HFC-134a NOAA global flask data from Montzka et al. [103] is 4.74±0.05 ppt per year. The Scientific Assessment of Ozone Depletion: 2018 also provides annual mole fractions of HFC-134a. AGAGE in situ measurements show 6.0 ppt yr^{-1} (7.2% per

yr^{-1}), NOAA flask measurements show 6.1 ppt yr^{-1} (7.4% per yr^{-1}) and UCI, flask measurements show ppt 7.2 yr^{-1} (8.5% per yr^{-1}) for 2015 - 2016. The annual mole fractions of AGAGE in situ measurements report 67.7 ppt in 2012, 83.3 ppt in 2015 and 89.3 ppt in 2016 [166]. Similarly, NOAA flask measurements report 67.5 ppt in 2012, 83.4 ppt in 2015 and 89.6 ppt in 2016 and UCI, flask measurements report 68.9 ppt in 2012, 84.9 ppt in 2015 and 92.1 ppt in 2016 [166]. These reported values are consistent with the ACE-FTS values in this study and the AGAGE values used to compare with ACE-FTS data.

ACE-FTS CHF_3 data were considered only between the altitudes 6.5 km and 12.5 km for the trend analysis. The linear trend of the ACE-FTS CHF_3 time series is 0.75±0.02 ppt per year. ACE-FTS CHF_3 data (Figure 52) show an average 5% difference compared to AGAGE 12-box model values. (ACE-FTS CHF_3 time series were also calculated for the latitude bins 50°S - 50°N and 40°S - 40°N and they show no significant difference from the original 60°S - 60°N ACE-FTS times series.) The reason for this discrepancy is not understood. The linear trend of the AGAGE 12-box model time series is 0.88±0.01 ppt per year. ACE-FTS HFC-134a and CHF_3 trend values show excellent agreement with the AGAGE trends. The trends and the VMRs of HFC-134a NOAA global flask data also show excellent agreement with the ACE-FTS HFC-134a VMR and trend values (Figure 48). The increasing atmospheric VMRs of HFC-134a have been used to derive global emissions by Fortems-Cheiney et al. [39]. These HFC-134a global data show that HFC-134a global emissions are increasing [39, 103] rapidly.

The ACE altitude ranges (6.5 - 12.5 km for CHF_3 and 6.5 - 15.5 km for HFC-134a) we have selected for comparisons with surface data are in the upper troposphere and lower extratropical stratosphere. Given the long lifetimes of CHF_3 (222 years) and HFC-134a (13.4 years), the gases should be well-mixed in the troposphere and lower stratosphere. Therefore, ACE-FTS VMRs and trends in Figure 47 and Figure 48 should be similar to the surface values.

The standard errors on the trends used in this paper are one standard deviation from a linear least squares analysis. The precision of individual VMR data points on the 1 km altitude grid for a particular occultation for CHF_3 is roughly 20 - 30% and around 100% for HFC-134a based on statistical error estimates in the retrievals. Since more than 2000 data points (n) are used for the annual averages in the ACE-FTS trend analysis, the precision of these average values is smaller (for uncorrelated

data the precision would be $\sqrt{n} = 45$ times smaller). The errors are therefore due to geophysical variability and systematic errors in the annual averages are not included in our analysis. For example, Harrison [49, 50] estimates the errors in the cross sections to be 3%. The systematic errors in the ACE-FTS retrievals can best be estimated by comparing with independent measurements as shown in Figures 47 and 48.

Figures 52 and 53 show the mission average latitudinal distributions of HFC-134a and CHF_3. The entire data set was averaged in 10 degree latitude bins for each altitude. Values more than 2 standard deviations away from each bin average were excluded. Data in the 80°N - 90°N bin of HFC-134a are not available as they were removed during the initial 2 standard deviation data filtering process. Both ACE-FTS HFC-134a and CHF_3 data are presented for the altitudes from 6.5 to 24.5 km. The standard deviation of the VMRs in each latitude-altitude bin of HFC-134a are 40 - 60% and of CHF_3 are about 20 - 30% for (Figure 54). These error estimates are therefore a combination of geophysical variability and fitting errors in the least-squares analysis in the retrievals. Notice the expanded color scale in Figure 52 for CHF_3 and the relatively large errors for HFC-134a. Most of the unusual patterns (e.g., 70°N for HFC-134a) lie within the error bars and are likely retrieval artifacts.

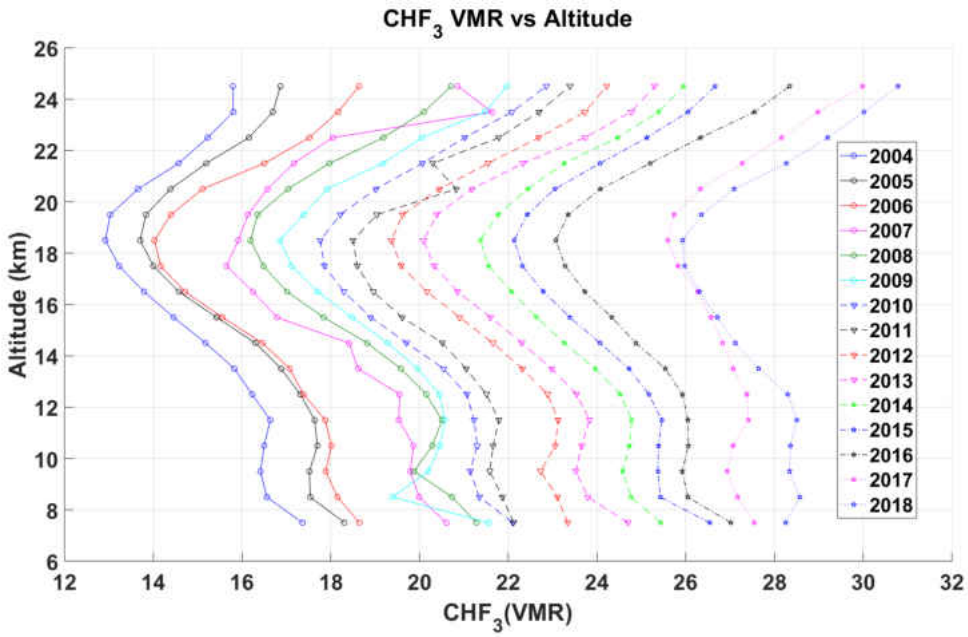

FIG. 49: ACE-FTS CHF_3 annual altitude profiles

The CHF_3 latitudinal distribution shows high VMRs (23 - 25 ppt) in the tropics

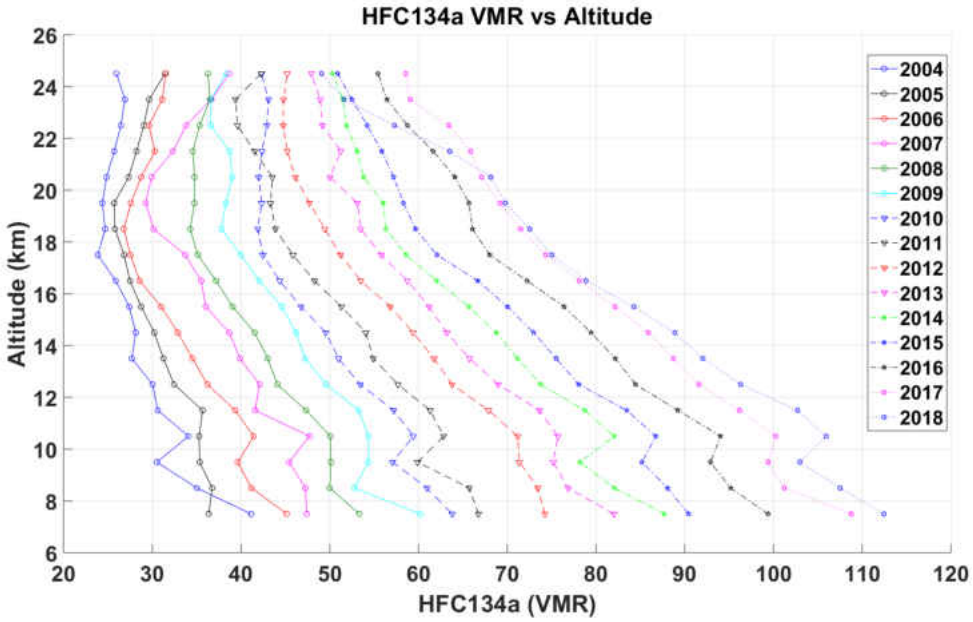

FIG. 50: ACE-FTS HFC-134a annual altitude profiles

in the upper troposphere relative to the poles. In the upper stratosphere (13.5 to 19.5 km) of the polar regions the volume mixing ratios of CHF_3 show low values between 18 - 22 ppt, and above 19.5 km the VMR values start to increase back to 23 - 25 ppt. There is also a band of high values from 22.5 km to 24.5 km at the top of the retrieval range. This unusual pattern may be a retrieval artifact because such VMR increases would imply a source. While such a source is conceivable from photolysis of other fluorine-containing molecules, a more likely explanation is a retrieval artifact.

In the troposphere the VMRs of the ACE-FTS HFC-134a range between 65 and 85 ppt. Compared to the CHF_3, the HFC-134a global distribution shows the expected decline with altitude. The peak HFC-134a cross section at 1104.5 cm^{-1} is about 5 times weaker than the peak HFC-23 cross section at 1156.1 cm^{-1} resulting in better precision for CHF_3 (Figure 54). Both molecules suffer from severe interference from ozone. Notice however that accuracy of CHF_3 (Figure 47) is worse than HFC-134a (Figure 48) probably because CHF_3 has a broader feature and suffers from more interference.

8.4 CONCLUSION

The global linear trend of the ACE-FTS HFC-134a time series is 4.9±0.1 ppt per

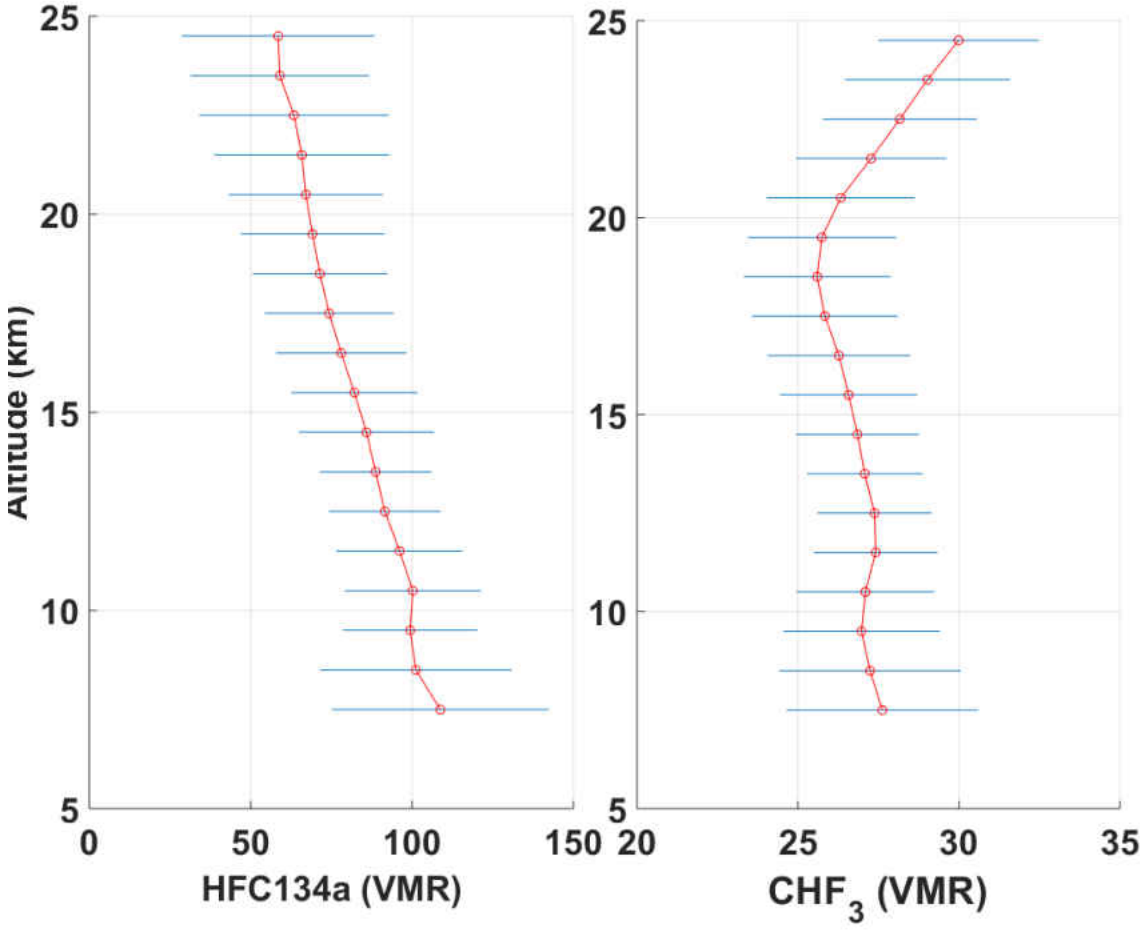

FIG. 51: ACE-FTS HFC-134a and CHF_3 average altitude profiles for 2017

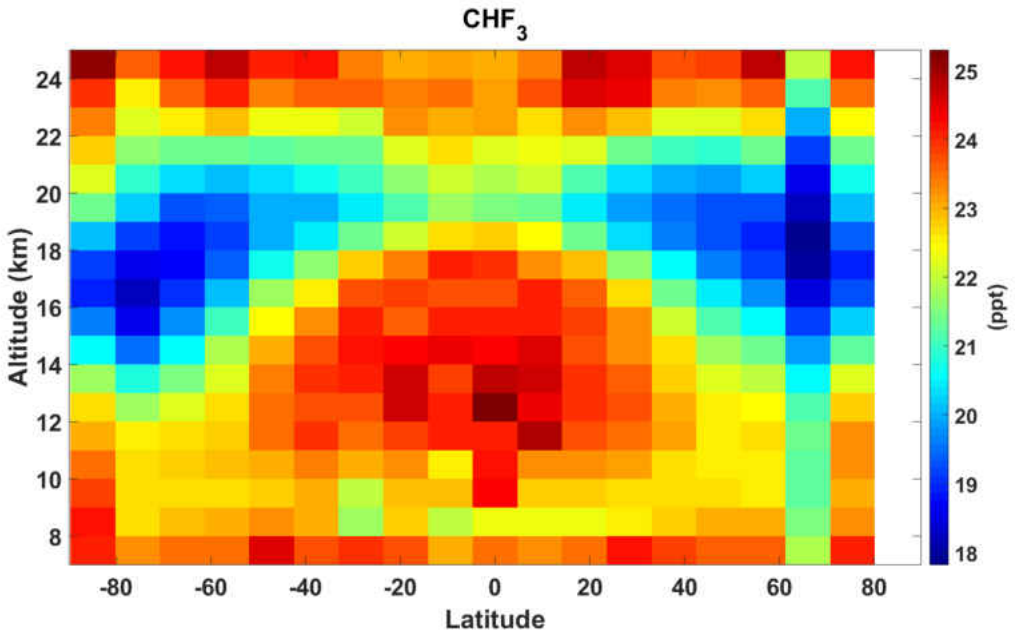

FIG. 52: CHF_3 latitudinal distribution

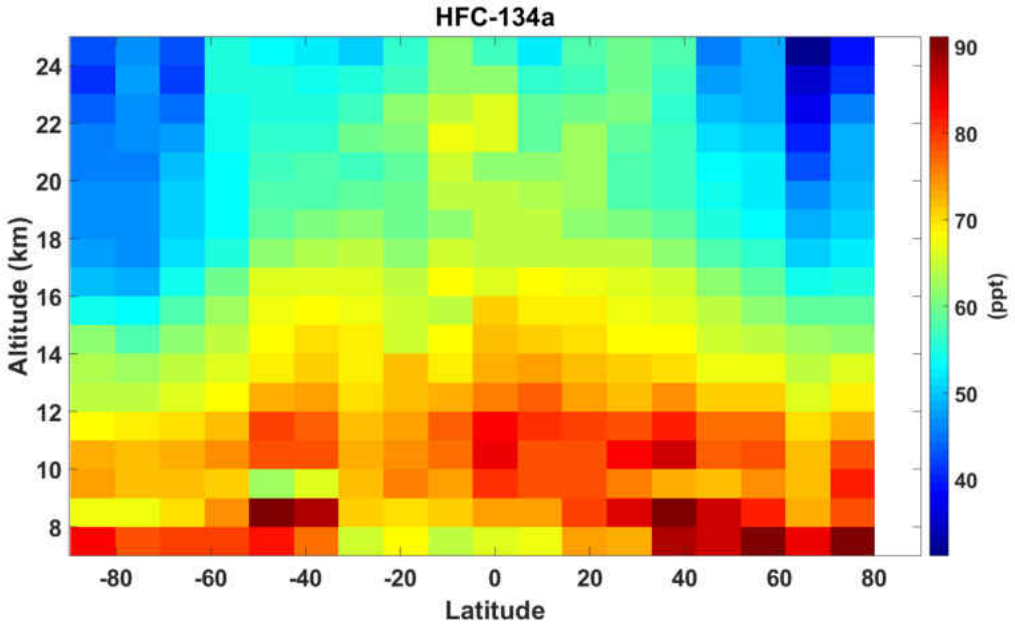

FIG. 53: HFC-134a latitudinal distribution

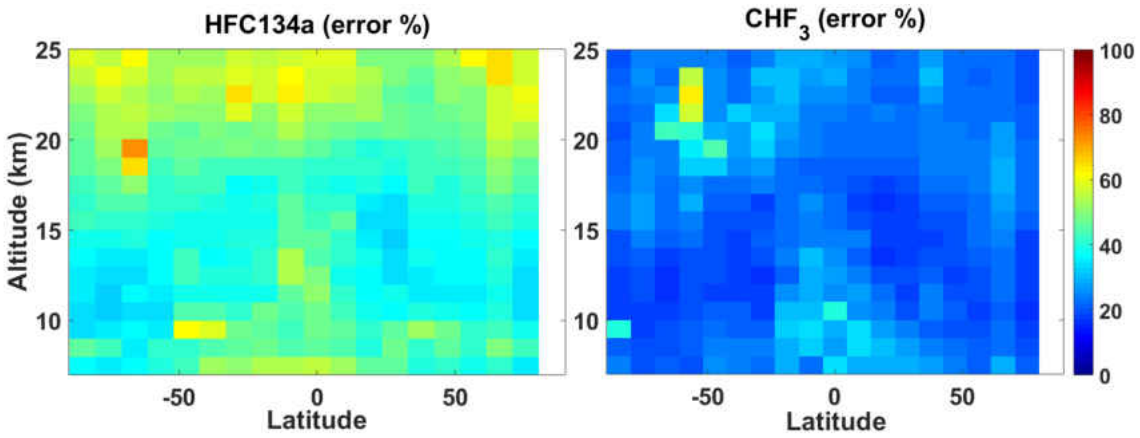

FIG. 54: Percentage error in HFC-134a and CHF_3 altitude-latitude distributions

year and is 4.87±0.05 ppt per year for the AGAGE time series. The global linear trend of the ACE-FTS CHF_3 time series is 0.75±0.02 ppt per year and the AGAGE 12-box model trend is 0.88±0.01 ppt per year. ACE-FTS trend values for HFC-134a and CHF_3 are in excellent agreement with the AGAGE linear trend values. The atmospheric abundances of HFC-134a and CHF_3 are increasing rapidly.

Almost all the trend values from different studies agree with ACE-FTS trends of HCl and also it shows that the success of Montreal Protocol has been and continues to be successful in reducing the surface emissions of Cl containing source gases [12].

REFERENCES

[1] *U.S. Standard Atmosphere, 1976*. U.S. Government Printing Office, Washington, D.C., 1976.

[2] Scientific assessment of ozone depletion. https://www.esrl.noaa.gov/csd/assessments/ozone/2014/, 2014.

[3] Montreal Protocol on Substances that Deplete the Ozone Layer. https://ozone.unep.org/countries, 2018.

[4] J. Anderson, J. M. Russell III, S. Solomon, and L. E. Deaver. Halogen Occultation Experiment confirmation of stratospheric chlorine decreases in accordance with the Montreal Protocol. *Journal of Geophysical Research: Atmospheres*, 105(D4):4483–4490, 2000.

[5] W. Aoki and T. Tsuji. High resolution infrared spectroscopy of CN and NH lines: nitrogen abundance in oxygen−rich giants through K to late M. *Astron. Astrophys*, 328:175–186, 1997.

[6] M. Asplund, N. Grevesse, A. J. Sauval, and P. Scott. The Chemical Composition of the Sun. *Annu. Rev. Astron. Astrophys*, 47:481–522, 2009.

[7] C. A. Beale, R. J. Hargreaves, and P. F. Bernath. Temperature-dependent high resolution absorption cross sections of propane. *Journal of Quantitative Spectroscopy and Radiative Transfer*, 182:219 – 224, 2016.

[8] B. A. Bergquist and J. D. Blum. Mass-Dependent and -Independent Fractionation of Hg Isotopes by Photoreduction in Aquatic Systems. *Science*, 318: 417–420, 2007.

[9] P. F. Bernath. *The Solar Occultation Mission ACE: An Overview. In: Kirchengast G., Foelsche U., Steiner A.K. (eds) Occultations for Probing Atmosphere and Climate*. Springer, Dordrecht., 2004.

[10] P. F. Bernath. *Spectra of Atoms and Molecules*. Oxford University Press, 3rd edition, 2016.

[11] P. F. Bernath. The Atmospheric Chemistry Experiment (ACE). *Journal of Quantitative Spectroscopy and Radiative Transfer*, 186:3 – 16, 2017. Satellite Remote Sensing and Spectroscopy: Joint ACE-Odin Meeting, October 2015.

[12] P. F. Bernath and A. M. Fernando. Trends in stratospheric HCl from the ACE satellite mission. *Journal of Quantitative Spectroscopy and Radiative Transfer*, 217:126 – 129, 2018.

[13] Peter F. Bernath, Dror M. Bittner, and Edwin L. Sibert III. Isobutane infrared bands: Partial rotational assignments, ab initio calculations, and local mode analysis. *The Journal of Physical Chemistry A*, 123(29):6185–6193, 2019.

[14] P.F. Bernath, C. Boone, A.M. Fernando, and S. Jones. Low altitude CO_2 from the Atmospheric Chemistry Experiment (ACE) satellite. *Journal of Quantitative Spectroscopy and Radiative Transfer*, 238:106528, 2019.

[15] C. D. Boone, R. Nassar, K. A. Walker, Y. Rochon, S. D. McLeod, C. P. Rinsland, and P. F. Bernath. Retrievals for the atmospheric chemistry experiment Fourier-transform spectrometer. *Appl. Opt*, 44(33):7218–7231, 2005.

[16] C. R. Brazier, R. S. Ram, and P. F. Bernath. Fourier transform spectroscopy of the $A^3\Pi - X^3\Sigma^-$ transition of NH. *J. Mol. Spectrosc*, 120(4):381–402, 1986.

[17] C. A. M. Brenninkmeijer, C. Janssen, J. Kaiser, T. Röckmann, T. S. Rhee, and S. S. Assonov. Isotope Effects in the Chemistry of Atmospheric Trace Compounds. *Chemical Reviews*, 103(12):5125–5162, 2003.

[18] C. A. M. Brenninkmeijer, P. Crutzen, F. Boumard, T. Dauer, B. Dix, R. Ebinghaus, D. Filippi, H. Fischer, H. Franke, U. Frieβ, J. Heintzenberg, F. Helleis, M. Hermann, H. H. Kock, C. Koeppel, J. Lelieveld, M. Leuenberger, B. G. Martinsson, S. Miemczyk, H. P. Moret, H. N. Nguyen, P. Nyfeler, D. Oram, D. O'Sullivan, S. Penkett, U. Platt, M. Pupek, M. Ramonet, B. Randa, M. Reichelt, T. S. Rhee, J. Rohwer, K. Rosenfeld, D. Scharffe, H. Schlager, U. Schumann, F. Slemr, D. Sprung, P. Stock, R. Thaler, F. Valentino, P. van Velthoven, A. Waibel, A. Wandel, K. Waschitschek, A. Wiedensohler, I. Xueref-Remy, A. Zahn, U. Zech, and H. Ziereis. Civil aircraft for the regular investigation of the atmosphere based on an instrumented container: The new CARIBIC system. *Atmospheric Chemistry and Physics*, 7(18):4953–4976, 2007.

[19] J. S. A. Brooke, P. F. Bernath, and C. M. Western. Improved line strengths of rovibrational and rotational transitions within the $X^3\Sigma^-$ ground state of NH. *J. Chem. Phys*, 143(2):026101, 2015.

[20] A. T. Brown, M. P. Chipperfield, C., C. Wilson, K. A. Walker, and P. F. Bernath. Trends in atmospheric halogen containing gases since 2004. *Journal of Quantitative Spectroscopy and Radiative Transfer*, 112(16):2552 – 2566, 2011.

[21] N. Butchart. The Brewer−Dobson circulation. *Reviews of Geophysics*, 52(2): 157–184, 2014.

[22] M. T. Chahine, Luke Chen, Paul Dimotakis, Xun Jiang, Qinbin Li, Edward T. Olsen, Thomas Pagano, James Randerson, and Yuk L. Yung. Satellite remote sounding of mid-tropospheric CO_2. *Geophysical Research Letters*, 35:L17807, 2008.

[23] R. J. Cicerone and J. L. McCrumb. Photodissociation of isotopically heavy O_2 as a source of atmospheric O_3. *Geophysical Research Letters*, 7(4):251–254, 1980.

[24] C. J. Cramer. *Essentials of Computational Chemistry: Theories and Models*. John Wiley & Sons, Ltd, 2nd edition, 2014.

[25] I. A. Crawford and D.A. Williams. Detection of interstellar NH towards ζ Ophiuchi by means of ultra-high-resolution spectroscopy. *Mon. Notices Royal Astron. Soc*, 291(3):L53–L56, 1997.

[26] C. Crevoisier, A. Chédin, H. Matsueda, T. Machida, R. Armante, and N. A. Scott. First year of upper tropospheric integrated content of CO_2 from IASI hyperspectral infrared observations. *Atmospheric Chemistry and Physics*, 9 (14):4797–4810, 2009.

[27] M. De Mazière, A. M. Thompson, M. J. Kurylo, J. D. Wild, G. Bernhard, T. Blumenstock, G. O. Braathen, J. W. Hannigan, J.C. Lambert, T. Leblanc, T. J. McGee, G. Nedoluha, I. Petropavlovskikh, G. Seckmeyer, P. C. Simon, W. Steinncht, and S. E. Strahan. The Network for the Detection of Atmospheric Composition Change (NDACC): history, status and perspectives. *Atmospheric Chemistry and Physics*, 18(7):4935–4964, 2018.

[28] H. Dekker, S. D'Odorico, A. Kaufer, B. Delabre, and H.Kotzlowski. Design, construction, and performance of UVES, the echelle spectrograph for the UT2 Kueyen Telescope at the ESO Paranal Observatory. *Proc. SPIE*, 4008:534–545, 2000.

[29] R. N. Dixon. The 0-0 and 1-0 bands of the $A^3\Pi - X^3\Sigma^-$ system of NH. *Can. J. Phys*, 37(10):1171–1186, 1959.

[30] M. Dobrijevic, J. C. Loison, K. M. Hickson, and G Gronoff. 1D-coupled photochemical model of neutrals, cations and anions in the atmosphere of Titan. *Icarus*, 268:313–339, 2016.

[31] J. R. Durig, Aiying Wang, Wafaa Beshir, and T. S. Little. Barrier to asymmetric internal rotation, conformational stability, vibrational spectra and assignments, and *ab initio* calculations of n-butane-d_0, d_5 and d_{10}. *Journal of Raman Spectroscopy*, 22(11):683–704, 1991.

[32] J. M. Eder. Contributions to spectral analysis. *Denkschr. Wien. Akad.*, 60: 1–24, 1893.

[33] P. W. Fairchild, G. P. Smith, D. R. Crosley, and J. B. Jeffries. Lifetimes and transition probabilities for NH ($A^3\Pi - X^3\Sigma^-$). *Chem. Phys. Lett*, 107(2): 181–186, 1984.

[34] J. C. Farman, B. G. Gardiner, and J. D. Shanklin. Large Losses of Total Ozone in Antarctica Reveal Seasonal ClO_x/NO_x Interaction. *Nature*, 315:207–210, 1985.

[35] G. T. Farmer and J. Cook. *Introduction to Earth's Atmosphere. In: Climate Change Science: A Modern Synthesis.* Springer, D., 2013.

[36] A. M. Fernando, P. F. Bernath, J. N. Hodges, and T. Masseron. A new linelist for the $A^3\Pi$ - $X^3\Sigma^-$ transition of the NH free radical. *Journal of Quantitative Spectroscopy and Radiative Transfer*, 217:29 – 34, 2018.

[37] A. M. Fernando, P. F. Bernath, and C. D. Boone. Ozone isotopologue measurements from the Atmospheric Chemistry Experiment (ACE). *Journal of Quantitative Spectroscopy and Radiative Transfer*, 238:106547, 2019.

[38] A. M. Fernando, P. F. Bernath, and C. D. Boone. Trends in atmospheric HFC-23 (CHF_3) and HFC-134a abundances. *Journal of Quantitative Spectroscopy and Radiative Transfer*, 238:106540, 2019.

[39] A. Fortems-Cheiney, M. Saunois, I. Pison, F. Chevallier, P. Bousquet, C. Cressot, S. A. Montzka, P. J. Fraser, M. K. Vollmer, P. G. Simmonds, D. Young, S. O'Doherty, R. F. Weiss, F. Artuso, B. Barletta, D. R. Blake, S. Li, C. Lunder, B. R. Miller, S. Park, R. Prinn, T. Saito, L. P. Steele, and Y. Yokouchi. Increase in HFC-134a emissions in response to the success of the Montreal Protocol. *Journal of Geophysical Research: Atmospheres*, 120(22):11,728–11,742, 2015.

[40] A. Fowler and C. C. L. Gregory. The ultra-violet band of ammonia and its occurrence in the solar spectrum. *Philos. Trans. Royal Soc. A*, 218:351–372, 1919.

[41] L. Froidevaux, J. Anderson, H.-J. Wang, R. A. Fuller, M. J. Schwartz, M. L. Santee, N. J. Livesey, H. C. Pumphrey, P. F. Bernath, J. M. Russell III, and M. P. McCormick. Global OZone Chemistry And Related trace gas Data records for the Stratosphere (GOZCARDS): methodology and sample results with a focus on HCl, H_2O, and O_3. *Atmospheric Chemistry and Physics*, 15 (18):10471–10507, 2015.

[42] G. W. Funke. Das Absorptions spektrum des NH. *Zeitschrift für Physik*, 101 (1):104–112, 1936.

[43] Y. Q. Gao and R. A. Marcus. Strange and Unconventional Isotope Effects in Ozone Formation. *Science*, 293:259–263, 2001.

[44] Y. Q. Gao and R. A. Marcus. An approximate theory of the ozone isotopic effects: Rate constant ratios and pressure dependence. *The Journal of Chemical Physics*, 127(24):244316, 2007.

[45] A. Grant, E. L. Yates, P. G. Simmonds, R. G. Derwent, A. J. Manning, D. Young, D. E. Shallcross, and S. O'Doherty. A five year record of high-frequency in situ measurements of non-methane hydrocarbons at Mace Head, Ireland. *Atmospheric Measurement Techniques*, 4(5):955–964, 2011.

[46] T. K. Greathouse, J. H. Lacy, B.Bézard, J. I. Moses, M. J. Richter, and C. Knez. The first detection of propane on Saturn. *Icarus*, 181(1):266 – 271, 2006.

[47] O. Gustafsson, G. Kindvall, M. Larsson, B. J. Olsson, and P. Sigray. An experimental and theoretical investigation of the radiative properties of the $A^3\Pi$ state of NH. *Chem. Phys. Lett*, 138(2):185–194, 1987.

[48] R. J. Hargreaves, E. Buzan, M. Dulick, and P. F. Bernath. High-resolution absorption cross sections of C_2H_6 at elevated temperatures. *Molecular Astrophysics*, 1:20 – 25, 2015.

[49] J. J. Harrison. Infrared absorption cross sections for trifluoromethane. *Journal of Quantitative Spectroscopy and Radiative Transfer*, 130:359 – 364, 2013.

[50] J. J. Harrison. Infrared absorption cross sections for 1,1,1,2-tetrafluoroethane. *Journal of Quantitative Spectroscopy and Radiative Transfer*, 151:210 – 216, 2015.

[51] J. J. Harrison and P. F. Bernath. Infrared absorption cross sections for propane (C_3H_8) in the 3 μm region. *Journal of Quantitative Spectroscopy and Radiative Transfer*, 111(9):1282 – 1288, 2010.

[52] J. J. Harrison, C. D. Boone, A. T. Brown, N. D. C. Allen, G. C. Toon, and P. F. Bernath. First remote sensing observations of trifluoromethane (HFC-23) in the upper troposphere and lower stratosphere. *Journal of Geophysical Research: Atmospheres*, 117(D5):308, 2012.

[53] V. Haverd, Geoffrey C. Toon, and David W. T. Griffith. Evidence for altitude-dependent photolysis-induced ^{18}O isotopic fractionation in stratospheric ozone. *Geophysical Research Letters*, 32(22), 2005.

[54] W. G. Hawkins and P. L. Houston. Hydrazine photochemistry induced by an argon fluoride excimer laser. *J. Phys. Chem*, 86(5):704–709, 1982.

[55] R. Herman and R. F. Wallis. Influence of vibration-rotation interaction on line intensities in vibration-rotation bands of diatomic molecules. *J. Chem. Phys*, 23(4):637–646, 1955.

[56] G. Herzberg. *Molecular spectra and molecular structure: 1. Spectra of diatomic molecules*. Princeton, New Jersey, 2nd edition, 1999.

[57] D. M. Hewett, P. F. Bernath, and B. E. Billinghurst. Infrared absorption cross sections of isobutane with hydrogen and nitrogen as broadening gases. *Journal of Quantitative Spectroscopy and Radiative Transfer*, 227:226 – 229, 2019.

[58] R. L. S. Hilderbrandt and J. D. Wieser. The zero point average structure of isobutane as determined by electron diffraction and microwave spectroscopy. *Journal of Molecular Structure*, 15:27–36, 1973.

[59] J. N. Hodges, D. M. Bittner, and P. F. Bernath. Improved Ultraviolet and Infrared Oscillator Strengths for OH^+. *Astrophys. J*, 855(1):21, 2018.

[60] J. M. Hollas. *Modern Spectroscopy*. John Wiley & Sons, Ltd, 3rd edition, 1996.

[61] Intergovernmental Panel on Climate Change. *Climate Change 2013: The Physical Science Basis: Working Group I Contribution to the Fifth Assessment Report of the Intergovernmental Panel on Climate Change*. Cambridge University Press, 2014.

[62] F. W. Irion, M. R. Gunson, C. P. Rinsland, Y. L. Yung, M. C. Abrams, A. Y. Chang, and A. Goldman. Heavy ozone enrichments from ATMOS infrared solar spectra. *Geophysical Research Letters*, 23(17):2377–2380, 1986.

[63] D. J. Jacob. *Introduction to Atmospheric Chemistry*. Princeton University Press, 1999.

[64] C. Janssen, J. Guenther, D. Krankowsky, and K. Mauersberger. Temperature dependence of ozone rate coefficients and isotopologue fractionation in ^{16}O - ^{18}O oxygen mixtures. *Chemical Physics Letters*, 367(1):34 – 38, 2003.

[65] X. Jiang, D. Crisp, E. T. Olsen, S. S. Kulawik, C. E. Miller, T. S. Pagano, M.G Liang, and Y. L. Yung. CO_2 annual and semiannual cycles from multiple satellite retrievals and models. *Earth and Space Science*, 3(2):78–87, 2016.

[66] D. G. Johnson, K. W. Jucks, W. A. Traub, and K. V. Chance. Isotopic composition of stratospheric ozone. *Journal of Geophysical Research: Atmospheres*, 105(D7):9025–9031, 2000.

[67] B. Jonkheid, T. Röckmann, N. Glatthor, C. Janssen, G. Stiller, and T. von Clarmann. Retrievals of heavy ozone with MIPAS. *Atmospheric Measurement Techniques*, 9(12):6069–6079, 2016.

[68] A. Karion, C. Sweeney, P. Tans, and T. Newberger. AirCore: An Innovative Atmospheric Sampling System. *Journal of Atmospheric and Oceanic Technology*, 27(11):1839–1853, 2010.

[69] J. F. Kasting. Runaway and moist greenhouse atmospheres and the evolution of Earth and Venus. *Icarus*, 74(3):472 – 494, 1988.

[70] J. A. Kaye and D. F. Strobel. Enhancement of heavy ozone in the Earth's atmosphere. *Journal of Geophysical Research: Oceans*, 88(C13):8447–8452, 1983.

[71] H. Keller-Rudek, G. K. Moortgat, R. Sander, and R. Sörensen. The MPI-Mainz UV/VIS Spectral Atlas of Gaseous Molecules of Atmospheric Interest. *Earth System Science Data*, 5(2):365–373, 2013.

[72] R. Kohlhepp, R. Ruhnke, M. P. Chipperfield, M. De Mazière, J. Notholt, S. Barthlott, R. L. Batchelor, R. D. Blatherwick, Th. Blumenstock, M. T. Coffey, P. Demoulin, H. Fast, W. Feng, A. Goldman, D. W. T. Griffith, K. Hamann, J. W. Hannigan, F. Hase, N. B. Jones, A. Kagawa, I. Kaiser, Y. Kasai, O. Kirner, W. Kouker, R. Lindenmaier, E. Mahieu, R. L. Mittermeier, B. Monge-Sanz, I. Morino, I. Murata, H. Nakajima, M. Palm, C. Paton-Walsh, U. Raffalski, Th. Reddmann, M. Rettinger, C. P. Rinsland, E. Rozanov, M. Schneider, C. Senten, C. Servais, B.-M. Sinnhuber, D. Smale, K. Strong, R. Sussmann, J. R. Taylor, G. Vanhaelewyn, T. Warneke, C. Whaley, M. Wiehle, and S. W. Wood. Observed and simulated time evolution of HCl, $ClONO_2$, and HF total column abundances. *Atmospheric Chemistry and Physics*, 12(7):3527–3556, 2012.

[73] D. Krankowsky, P. Lämmerzahl, and K. Mauersberger. Isotopic measurements of stratospheric ozone. *Geophysical Research Letters*, 27(17):2593–2595, 2000.

[74] D. Krankowsky, P. Lämmerzahl, K. Mauersberger, C. Janssen, B. Tuzson, and T. Röckmann. Stratospheric ozone isotope fractionations derived from collected samples. *Journal of Geophysical Research: Atmospheres*, 112(D8):301, 2007.

[75] L. Kuai, J. Worden, S. Kulawik, K. Bowman, M. Lee, S. C. Biraud, J. B. Abshire, S. C. Wofsy, V. Natraj, C. Frankenberg, D. Wunch, B. Connor, C. Miller, C. Roehl, R.-L. Shia, and Y. Yung. Profiling tropospheric CO_2 using Aura TES

and TCCON instruments. *Atmospheric Measurement Techniques*, 6(1):63–79, 2013.

[76] A. Kuze, H. Suto, M. Nakajima, and T. Hamazaki. Thermal and near infrared sensor for carbon observation Fourier-transform spectrometer on the Greenhouse Gases Observing Satellite for greenhouse gases monitoring. *Appl. Opt*, 48(35):6716–6733, 2009.

[77] A. A. Lacis, G. A. Schmidt, D. Rind, and R. A. Ruedy. Atmospheric CO_2: Principal Control Knob Governing Earth's Temperature. *Science*, 330(6002): 356–359, 2010.

[78] D. L. Lambert, J. A. Brown, K. H. Hinkle, and H. R. Johnson. Carbon, Nitrogen and Oxygen Abundances in Betelgeuse. *Astrophys. J*, 284(3):223–237, 1984.

[79] X. Lan, P. Tans, C. Sweeney, A. Andrews, A. Jacobson, M. Crotwell, E. Dlugokencky, J. Kofler, P. Lang, K. Thoning, and S. Wolter. Gradients of column CO_2 across North America from the NOAA Global Greenhouse Gas Reference Network. *Atmospheric Chemistry and Physics*, 17(24):15151–15165, 2017.

[80] R. J. Le Roy. RKR1: A computer program implementing the first-order RKR method for determining diatomic molecule potential energy functions. *Journal of Quantitative Spectroscopy and Radiative Transfer*, 186:158–166, 2017.

[81] R. J. Le Roy. LEVEL: A computer program for solving the radial Schrödinger equation for bound and quasi-bound levels. *Journal of Quantitative Spectroscopy and Radiative Transfer*, 186:167–178, 2017.

[82] K. Lee, Z. Li, Y. Kim, and A. Kokhanovsky. *Atmospheric Aerosol Monitoring from Satellite Observations: A History of Three Decades*. 2009.

[83] J. M. Lents. An evaluation of molecular constants and transition probabilities for the NH free radical. *Journal of Quantitative Spectroscopy and Radiative Transfer*, 13(4):297–310, 1973.

[84] I. N. Levine. *Quantum Chemistry*. Pearson Education Inc., 7rd edition, 2014.

[85] M. C. Liang, G. A. Blake, and Y. L. Yung. A semianalytic model for photo-induced isotopic fractionation in simple molecules. *Journal of Geophysical Research: Atmospheres*, 109(D5):308, 2004.

[86] D. R. Lide. Structure of the Isobutane Molecule; Change of Dipole Moment on Isotopic Substitution. *The Journal of Chemical Physics*, 33(5):1519–1522, 1960.

[87] K. Lodders and B. Fegley. Atmospheric Chemistry in Giant Planets, Brown Dwarfs, and Low-Mass Dwarf Stars: I. Carbon, Nitrogen, and Oxygen. *Icarus*, 155(2):393 – 424, 2002.

[88] M. López-Puertas, B. Funke, Á. A. Jurado-Navarro, M. García-Comas, A. Gardini, C. D. Boone, L. Rezac, and R. R. Garcia. Validation of the MIPAS CO_2 volume mixing ratio in the mesosphere and lower thermosphere and comparison with WACCM simulations. *Journal of Geophysical Research: Atmospheres*, 122(15):8345–8366, 2017.

[89] J. I. Lunine. Surface-atmosphere interactions on titan. In B. Schmitt, C. De Bergh, and M. Festou, editors, *Solar System Ices: Based on Reviews Presented at the International Symposium "Solar System Ices" held in Toulouse, France, on March 27–30, 1995*, pages 639–653. Springer Netherlands, 1998.

[90] M. F. Lunt, M. Rigby, A. L. Ganesan, A. J. Manning, R. G. Prinn, S. O'Doherty, J. Mühle, C. M. Harth, P. K. Salameh, T. Arnold, R. F. Weiss, T. Saito, Y. Yokouchi, P. B. Krummel, L. P. Steele, P. J. Fraser, S. Li, S. Park, S. Reimann, M. K. Vollmer, C. Lunder, O. Hermansen, N. Schmidbauer, M. Maione, J. Arduini, D. Young, and P. G. Simmonds. Reconciling reported and unreported HFC emissions with atmospheric observations. *Proc. Natl. Acad. Sci. U.S.A.*, 112(19):5927–5931, 2015.

[91] J. R. Lyons. Transfer of mass-independent fractionation in ozone to other oxygen-containing radicals in the atmosphere. *Geophysical Research Letters*, 28(17):3231–3234, 2001.

[92] E. Mahieu, M. P. Chipperfield, J. Notholt, T. Reddmann, J. Anderson, P. F. Bernath, T. Blumenstock, M. T. Coffey, S. S. Dhomse, W. Feng, B. Franco, L. Froidevaux, D. W. T. Griffith, J. W. Hannigan, F. Hase, R. Hossaini, N. B.

Jones, I. Morino, I. Murata, H. Nakajima, M. Palm, C. Paton-Walsh, J. M. Russell, M. Schneider, C. Servais, D. Smale, and K. A. Walker. Recent Northern Hemisphere stratospheric HCl increase due to atmospheric circulation changes. *Nature*, 515:104–107, 2014.

[93] J. Malicet, J. Brion, and H. Guenebaut. Contribution to the spectroscopic study of the transition $A^3\Pi - X^3\Sigma^-$ of the NH radical. *J. Chim. Phys*, 67: 25–30, 1970.

[94] C. Manzanares, J. Peng, N. Mina-Camilde, and A. Brock. Overtone spectroscopy of isobutane at cryogenic temperatures. *Chemical Physics*, 190(2):247 – 259, 1995.

[95] H. T. Mark. The mass-independent ozone isotope effect. *Science*, 293(5528): 226–226, 2001.

[96] T. Masseron, J.A. Johnson, B. Plez, S.Van Eck, F. Primas, S. Goriely, and A. Jorissen. A holistic approach to carbon-enhanced metal-poor stars. *Astron. Astrophys*, 509:A93, 2010.

[97] K. Mauersberger. Measurement of heavy ozone in the stratosphere. *Geophysical Research Letters*, 8(8):935–937, 1981.

[98] K. Mauersberger, B. Erbacher, D. Krankowsky, J. Günther, and R. Nickel. Ozone Isotope Enrichment: Isotopomer-Specific Rate Coefficients. *Science*, 283:370–372, 1999.

[99] K. Mauersberger, P. Lämmerzahl, and D. Krankowsky. Stratospheric ozone isotope enrichments revisited. *Geophysical Research Letters*, 28(16):3155–3158, 2001.

[100] D. M. Meyer and K. C. Roth. Discovery of Interstellar NH. *Astrophys. J*, 376: L49–L52, 1991.

[101] N. G. Mirkin and S. Krimm. Ab initio analysis of the vibrational spectra of conformers of some branched alkanes. *Journal of Molecular Structure*, 550-551: 67 – 91, 2000.

[102] S. A. Montzka, J. H. Butler, R. C. Myers, T. M. Thompson, T. H. Swanson, A. D. Clarke, L. T. Lock, and J. W. Elkins. Decline in the Tropospheric Abundance of Halogen from Halocarbons: Implications for Stratospheric Ozone Depletion. *Science*, 272:1318–1322, 1996.

[103] S. A. Montzka, M. McFarland, S. O. Andersen, B. R. Miller, D. W. Fahey, B. D. Hall, L. Hu, C. Siso, and J. W. Elkins. Recent Trends in Global Emissions of Hydrochlorofluorocarbons and Hydrofluorocarbons: Reflecting on the 2007 Adjustments to the Montreal Protocol. *J. Phys. Chem. A*, 119(19):4439–4449, 2015.

[104] G. Moreau, C. Robert, V. Catoire, M. Chartier, C. Camy-Peyret, N. Huret, M. Pirre, L. Pomathiod, and G. Chalumeau. SPIRALE: a multispecies in situ balloon−borne instrument with six tunable diode laser spectrometers. *Appl. Opt*, 44(28):5972–5989, 2005.

[105] T. Murai and M. Shimauchi. Rotational distortions of $^3\Pi$ states applied to NH molecule. *Sci. Light (Tokyo)*, 15:48–67, 1966.

[106] G. Myhre, D. Shindell, F.M. Brèon, W. Collins, J. Fuglestvedt, D. Koch J. Huang, J. F. Lamarque, D. Lee, B. Mendoza, T. Nakajima, A. Robock, G. Stephens, T. Takemura, and H. Zhang. *2013: Anthropogenic and Natural Radiative Forcing. In: Climate Change 2013: The Physical Science Basis: Working Group I Contribution to the Fifth Assessment Report of the Intergovernmental Panel on Climate Change [Stocker, T.F., D. Qin, G.-K. Plattner, M. Tignor, S.K. Allen, J. Boschung, A. Nauels, Y. Xia, V. Bex and P.M. Midgley (eds.)].* Cambridge University Press, Cambridge, United Kingdom and NY, USA., 2014.

[107] V. Naik, A. K. Jain, K. O. Patten, and D. J. Wuebbles. Consistent sets of atmospheric lifetimes and radiative forcings on climate for CFC replacements: HCFCs and HFCs. *Journal of Geophysical Research*, 105(D5):6903–6914, 2000.

[108] S. Ndengué, S. Madronich, F. Gatti, H. D. Meyer, O. Motapon, and R. Jost. Ozone photolysis: Strong isotopologue/isotopomer selectivity in the stratosphere. *Journal of Geophysical Research: Atmospheres*, 119(7):4286–4302, 2014.

[109] H. Neckel. Announcement. *Sol. Phys*, 184:421–422, 1999.

[110] C. A. Nixon, D. E. Jennings, J. M. Flaud, B. Bézard, N. A. Teanby, P. G. J. Irwin, T. M. Ansty, A. Coustenis, S. Vinatier, and F. M. Flasar. Titan's prolific propane: The Cassini CIRS perspective. *Planetary and Space Science*, 57(13): 1573 – 1585, 2009.

[111] D. E. Oram, C. E. Reeves, W. T. Sturges, S. A. Penkett, P. J. Fraser, and R. L. Langenfelds. Recent tropospheric growth rate and distribution of HFC-134a (CF_3CH_2F). *Geophysical Research Letters*, 23(15):1949–1952, 1996.

[112] D. E. Oram, W. T. Sturges, S. A. Penkett, A. McCulloch, and P. J. Fraser. Growth of fluoroform (CHF_3, HFC-23) in the background atmosphere. *Geophysical Research Letters*, 25(1):35–38, 1998.

[113] L. C. Owono Owono, D. B. Abdallah, N. Jaidane, and Z. B. Lakhdar. Theoretical radiative properties between states of the triplet manifold of NH radical. *J. Chem. Phys*, 128(8):084309, 2008.

[114] A. A. Pavlov and J. F. Kasting. Mass-Independent Fractionation of Sulfur Isotopes in Archean Sediments: Strong Evidence for an Anoxic Archean Atmosphere. *Astrobiology*, 2(1):27–41, 2002.

[115] W. Peters, A. R. Jacobson, C. Sweeney, A. E. Andrews, T. J. Conway, K. Masarie, J. B. Miller, L. M. P. Bruhwiler, G. Pétron, A. I. Hirsch, D. E. J. Worthy, G. R. van der Werf, J. T. Randerson, P. O. Wennberg, M. C. Krol, and P. P. Tans. An atmospheric perspective on North American carbon dioxide exchange: CarbonTracker. *Proceedings of the National Academy of Sciences*, 104(48):18925–18930, 2007.

[116] C. Piccolo, A. Dudhia, and V. H. Payne. Heavy ozone enrichments from MIPAS limb emission spectra. *Atmospheric Chemistry and Physics Discussions*, 9: 25127–25158, 2009.

[117] A. Pozzer, J. Pollmann, D. Taraborrelli, P. Jöckel, D. Helmig, P. Tans, J. Hueber, and J. Lelieveld. Observed and simulated global distribution and budget of atmospheric C_2-C_5 alkanes. *Atmospheric Chemistry and Physics*, 10(9): 4403–4422, 2010.

[118] D. Priem, J. M. Colmont, D. Petitprez, and S. Bailleux. The Rotational Spectrum of Isobutane up to 640 GHz: Splitting of the | K | = 3 Transitions. *Journal of Molecular Spectroscopy*, 184(1):84 – 87, 1997.

[119] R. G. Prinn, R. F. Weiss, P. J. Fraser, P. G. Simmonds, D. M. Cunnold, F. N. Alyea, S. O'Doherty, P. Salameh, B. R. Miller, J. Huang, R. H. J. Wang, D. E. Hartley, C. Harth, L. P. Steele, G. Sturrock, P. M. Midgley, and A. McCulloch. A history of chemically and radiatively important gases in air deduced from ALE/GAGE/AGAGE. *Journal of Geophysical Research: Atmospheres*, 105 (D14):17751–17792, 2000.

[120] R. G. Prinn, R. F. Weiss, J. Arduini, T. Arnold, H. L. DeWitt, P. J. Fraser, A. L. Ganesan, J. Gasore, C. M. Harth, O. Hermansen, J. Kim, P. B. Krummel, S. Li, Z. M. Loh, C. R. Lunder, M. Maione, A. J. Manning, B. R. Miller, B. Mitrevski, J. Mühle, S. O'Doherty, S. Park, S. Reimann, M. Rigby, T. Saito, P. K. Salameh, R. Schmidt, P. G. Simmonds, L. P. Steele, M. K. Vollmer, R. H. Wang, B. Yao, Y. Yokouchi, D. Young, and L. Zhou. History of chemically and radiatively important atmospheric gases from the Advanced Global Atmospheric Gases Experiment (AGAGE). *Earth System Science Data*, 10(2): 985–1018, 2018.

[121] B. Proedrou and K. Hocke. Characterising the three-dimensional ozone distribution of a tidally locked earth-like planet. *Earth, Planets and Space*, 68:96, 2016.

[122] R. S. Ram and P. F. Bernath. Revised molecular constants and term values for the $A^3\Pi$ and $X^3\Sigma^-$ states of NH. *J. Mol. Spectrosc*, 260(2):115–119, 2010.

[123] R. S. Ram, P. F. Bernath, and K. H. Hinkle. Infrared emission spectroscopy of NH: Comparison of a cryogenic echelle spectrograph with a Fourier transform spectrometer. *J. Chem. Phys*, 110(12):5557–5563, 1999.

[124] F. Raulin, P. Bruston, P. Coll, D. Coscia, M-C. Gazeau, L. Guez, and E. de Vanssay. Exobiology on Titan. *Journal of Biological Physics*, 20(1): 39–53, 1995.

[125] A. R. Ravishankara and E. R. Lovejoy. Atmospheric lifetime, its application

and its determination: CFC-substitutes as a case study. *J. Chem. Soc., Faraday Trans*, 90:2159–2169, 1994.

[126] E. A. Ray, F. L. Moore, K. H. Rosenlof, S. M. Davis, C. Sweeney, P. Tans, T. Wang, J. W. Elkins, H. Bönisch, A. Engel, S. Sugawara, T. Nakazawa, and S. Aoki. Improving stratospheric transport trend analysis based on SF_6 and CO_2 measurements. *Journal of Geophysical Research: Atmospheres*, 119(24): 14,110–14,128, 2014.

[127] S. S. Richard. The Antarctic Ozone Hole. *Scientific American*, 258(1):30–37, 1988.

[128] H. K. Roscoe. The Brewer-Dobson circulation in the stratosphere and mesosphere: Is there a trend?. *Advances in Space Research*, 38(11):2446 – 2451, 2006.

[129] L. S. Rothman, D. Jacquemart, A. Barbe, D. Chris Benner, M. Birk, L. R. Brown, M. R. Carleer, C. Chackerian, K. Chance, L. H. Coudert, V. Dana, V. M. Devi, J. M. Flaud, R. R. Gamache, A. Goldman, J. M. Hartmann, K. W. Jucks, A. G. Maki, J. Y. Mandin, S. T. Massie, J. Orphal, A. Perrin, C. P. Rinsland, M. A. H. Smith, J. Tennyson, R. N. Tolchenov, R. A. Toth, J. V. Auwera, P. Varanasi, and G. Wagner. The HITRAN 2004 molecular spectroscopic database. *Journal of Quantitative Spectroscopy and Radiative Transfer*, 96(2):139 – 204, 2005.

[130] F. S. Rowland and M. J. Molina. Stratospheric sink for chlorofluoromethanes: chlorine atom-catalysed destruction of ozone. *Nature*, 249(2):810–812, 1974.

[131] B. Ruscic. Active Thermochemical Tables: Sequential Bond Dissociation Enthalpies of Methane, Ethane, and Methanol and the Related Thermochemistry. *J. Phys. Chem. A*, 119(28):7810–7837, 2015.

[132] R. Schinke, S. Yu. Grebenshchikov, M. V. Ivanov, and P. Fleurat-Lessard. Dynamical studies of the ozone isotope effect: A Status Report. *Annual Review of Physical Chemistry*, 57(1):625–661, 2006.

[133] B. Schrader, J. Pacansky, and U. Pfeiffer. Calculation of the frequencies and intensities in the infrared spectra of matrix-isolated tert-butyl radical and isobutane. *The Journal of Physical Chemistry*, 88(18):4069–4073, 1984.

[134] S. W. Sharpe, T. J. Johnson, R. L. Sams, P. M. Chu, G. C. Rhoderick, and P. A. Johnson. Gas-Phase Databases for Quantitative Infrared Spectroscopy. *Applied Spectroscopy*, 58(12):1452–1461, 2004.

[135] P. G. Simmonds, M. Rigby, A. McCulloch, M. K. Vollmer, S. Henne, J. Mühle, S. O'Doherty, A. J. Manning, P. B. Krummel, P. J. Fraser, D. Young, R. F. Weiss, P. K. Salameh, C. M. Harth, S. Reimann, C. M. Trudinger, L. P. Steele, R. H. J. Wang, D. J. Ivy, R. G. Prinn, B. Mitrevski, and D. M. Etheridge. Recent increases in the atmospheric growth rate and emissions of HFC-23 (CHF_3) and the link to HCFC-22 ($CHClF_2$) production. *Atmos Chem Phys*, 18(6): 4153–4169, 2018.

[136] P. D. Sing and R. B. Gruenwald. The photodissociation lifetimes of the NH radical in comets. *Astron. Astrophys*, 178:277–282, 1987.

[137] C. Slater, T. Preston, and L. T. Weaver. Stable isotopes and the international system of units. *Rapid Communications in Mass Spectrometry*, 15(15):1270–1273, 2001.

[138] V. V. Smith and D. L. Lambert. The chemical composition of Red Giants. II. Helium burning and the s-process in the MS and S stars. *Astrophys. J*, 311: 843–863, 1986.

[139] W. H. Smith and H. S. Liszt. Franck-Condon factors and absolute oscillator strengths for NH, SiH, S_2 and SO. *Journal of Quantitative Spectroscopy and Radiative Transfer*, 11(1):45–54, 1971.

[140] W. H. Smith, J. Brzozowski, and P. Erman. Lifetime studies of the NH molecule: New predissociations, the dissociation energy, and interstellar diatomic recombination. *J. Chem. Phys*, 64(11):4628–4633, 1976.

[141] C. Sneden. The nitrogen abundance of the very metal-poor star HD 122563. *Astrophys. J.*, 184:839–849, 1973.

[142] Z. Song, D. Shi, J. Sun, and Z. Zhu. Accurate spectroscopic calculations of the 12 Λ-S and 25 Ω states of the NH radical including the spin-orbit coupling effect. *Comput. Theor. Chem*, 1093(5):81–90, 2016.

[143] M. Spite, R. Cayrel, B. Plez, V. Hill, F. Spite, E. Depagne, P. François, P. Bonifacio, B. Barbuy, T. Beers, J. Andersen, P. Molaro, B. Nordström, and F. Primas. First stars VI - Abundances of C, N, O, Li, and mixing in extremely metal-poor giants. Galactic evolution of the light elements. *Astron. Astrophys*, 430:655–668, 2005.

[144] A. R. Stavert, R. M. Law, M. van der Schoot, R. L. Langenfelds, D. A. Spencer, P. B. Krummel, S. D. Chambers, A. G. Williams, S. Werczynski, R. J. Francey, and R. T. Howden. The Macquarie Island (LoFlo2G) high-precision continuous atmospheric carbon dioxide record. *Atmospheric Measurement Techniques*, 12 (2):1103–1121, 2019.

[145] R. S. Stolarski, A. R. Douglass, and S. E. Strahan. Using satellite measurements of N_2O to remove dynamical variability from HCl measurements. *Atmospheric Chemistry and Physics*, 18(8):5691–5697, 2018.

[146] M. R. Swain, G. Tinetti, G. Vasisht, P. Deroo, C. Griffith, J. Bouwman, Pin Chen, Y. Yung, A. Burrows, L. R. Brown, J. Matthews, J. F. Rowe, R. Kuschnig, and D. Angerhausen. Water, methane, and carbon dioxide present in the dayside spectrum of the exoplanet HD 209458b. *The Astrophysical Journal*, 704(2):1616–1621, 2009.

[147] P. Swings, C. T. Elvey, and W. Babcock. The Spectrum of Comet Cunningham, 1940C. *Astrophys. J*, 94:320, 1941.

[148] J. T. Emmert, M. H. Stevens, P. F. Bernath, D. P. Drob, and C. D. Boone. Observations of increasing carbon dioxide concentration in Earth's thermosphere. *Nature Geoscience*, 5:868–871, 2012.

[149] M. H. Thiemens and J. E. Heidenreich. The Mass-Independent Fractionation of Oxygen: A Novel Isotope Effect and Its Possible Cosmochemical Implications. *Science*, 219:1073–1075, 1983.

[150] G. C. Toon, J. F. Blavier, B. Sen, J. J. Margitan, C. R. Webster, R. D. May, D. Fahey, R. Gao, L. Del Negro, M. Proffitt, J. Elkins, P. A. Romashkin, D. F. Hurst, S. Oltmans, E. Atlas, S. Schauffler, F. Flocke, T. P. Bui, R. M. Stimpfle, G. P. Bonne, P. B. Voss, and R. C. Cohen. Comparison of MkIV balloon and

ER-2 aircraft measurements of atmospheric trace gases. *Journal of Geophysical Research: Atmospheres*, 104(D21):26779–26790, 1999.

[151] T. Tsuji. Molecular abundance in stellar atmospheres. *Annals of the Tokyo Astronomical Observatory*, 9:1–110, 1964.

[152] T. Umezawa, H. Matsueda, Y. Sawa, Y. Niwa, T. Machida, and L. Zhou. Seasonal evaluation of tropospheric CO_2 over the Asia-Pacific region observed by the CONTRAIL commercial airliner measurements. *Atmospheric Chemistry and Physics*, 18(20):14851–14866, 2018.

[153] UNEP Ozone Secretariat. *Handbook for the Montreal Protocol on Substances that Deplete the Ozone Layer: Eleventh edition (2017)*. Cambridge University Press, 2017.

[154] R. Van Wachem, F.H. De Leeuw, and A. Dymanus. Dipole Moments of KF and KBr Measured by the Molecular-Beam Electric-Resonance Method. *The Journal of Chemical Physics*, 47(7):2256–2258, 1967.

[155] G. J. M. Velders, D. W. Fahey, J. S. Daniel, M. McFarland, and S. O. Andersen. Large contribution of projected HFC emissions to future climate forcing. *Proc. Natl. Acad. Sci.*, 106(27):10949–10954, 2009.

[156] G. J. M. Velders, D. W. Fahey, J. S. Daniel, S. O. Andersen, and M. McFarland. Future atmospheric abundances and climate forcings from scenarios of global and regional hydrofluorocarbon (HFC) emissions. *Atmos Env*, 123:200 – 209, 2015.

[157] V. Vuitton, R. V. Yelle, S. J. Klippenstein, S. M. Hörst, and P. Lavvas. Simulating the density of organic species in the atmosphere of Titan with a coupled ion-neutral photochemical model. *Icarus*, 324:120 – 197, 2019.

[158] J. W. Waters, L. Froidevaux, R. S. Harwood, R. F. Jarnot, H. M. Pickett, W. G. Read, P. H. Siegel, R. E. Cofield, M. J. Filipiak, D. A. Flower, J. R. Holden, G. K. Lau, N. J. Livesey, G. L. Manney, H. C. Pumphrey, M. L. Santee, D. L. Wu, D. T. Cuddy, R. R. Lay, M. S. Loo, V. S. Perun, M. J. Schwartz, P. C. Stek, R. P. Thurstans, M. A. Boyles, K. M. Chandra, M. C. Chavez, Gun-Shing Chen, B. V. Chudasama, R. Dodge, R. A. Fuller, M. A.

Girard, J. H. Jiang, Yibo Jiang, B. W. Knosp, R. C. LaBelle, J. C. Lam, K. A. Lee, D. Miller, J. E. Oswald, N. C. Patel, D. M. Pukala, O. Quintero, D. M. Scaff, W. Van Snyder, M. C. Tope, P. A. Wagner, and M. J. Walch. The Earth Observing System Microwave Limb Sounder (EOS MLS) on the Aura Satellite. *IEEE Transactions on Geoscience and Remote Sensing*, 44(5):1075–1092, 2006.

[159] E. C. Weatherhead, G. C. Reinsel, G. C. Tiao, X. L. Meng, D. Choi, W. K. Cheang, T. Keller, J. DeLuisi, D. J. Wuebbles, J. B. Kerr, A. J. Miller, S. J. Oltmans, and J. E. Frederick. Factors affecting the detection of trends: Statistical considerations and applications to environmental data. *Journal of Geophysical Research: Atmospheres*, 103(D14):17149–17161, 1998.

[160] S. Weiss and G. Leroi. Infrared spectra and internal rotation in propane, isobutane and neopentane. *Spectrochimica Acta Part A: Molecular Spectroscopy*, 25: 1759–1766, 1969.

[161] H. J. Werner, P. J. Knowles, G. Knizia, F. R. Manby, and M. Schütz. Molpro: A general-purpose quantum chemistry program package. *Wiley Interdisciplinary Reviews: Computational Molecular Science*, 2(2):242–253, 2012.

[162] T. Weselak, G. A. Galazutdinov, Y. Beletsky, and J. Krelowski. Interstellar NH molecule in translucent sightlines. *Mon. Notices Royal Astron. Soc*, 400 (1):392–397, 2009.

[163] C. M. Western. PGOPHER: A program for simulating rotational, vibrational and electronic spectra. *Journal of Quantitative Spectroscopy and Radiative Transfer*, 186:221–242, 2017.

[164] WMO (World Meteorological Organization). *Scientific Assessment of Ozone Depletion: 1998, Global Ozone Research and Monitoring Project-Report No. 37, 25 pp.* Geneva, Switzerland, 1994.

[165] WMO (World Meteorological Organization). *Scientific Assessment of Ozone Depletion: 1998, Global Ozone Research and Monitoring Project-Report No. 44, 27 pp.* Geneva, Switzerland, 1998.

[166] WMO (World Meteorological Organization). *Scientific Assessment of Ozone Depletion: 2018, Global Ozone Research and Monitoring Project-Report No. 58, 588 pp.* Geneva, Switzerland, 2018.

[167] S. C. Wofsy. HIAPER Pole-to-Pole Observations (HIPPO): fine-grained, global-scale measurements of climatically important atmospheric gases and aerosols. *Philosophical Transactions of the Royal Society A: Mathematical, Physical and Engineering Sciences*, 369:2073–2086, 2011.

[168] D. Wunch, G. C. Toon, J. F. L. Blavier, R. A. Washenfelder, J. Notholt, B. J. Connor, D. W. T. Griffith, V. Sherlock, and P. O. Wennberg. The Total Carbon Column Observing Network. *Philosophical Transactions of the Royal Society A: Mathematical, Physical and Engineering Sciences*, 369:2087–2112, 2011.

[169] B. Xiang, P. K. Patra, S. A. Montzka, S. M. Miller, J. W. Elkins, F. L. Moore, E. L. Atlas, B. R. Miller, R. F. Weiss, R. G. Prinn, and S. C. Wofsy. Global emissions of refrigerants HCFC-22 and HFC-134a: Unforeseen seasonal contributions. *Proc. Natl. Acad. Sci.*, 111(49):17379–17384, 2014.

[170] D. R. Yarkony. On the electronic structure of the NH radical. The fine structure splitting of the $X^3\Sigma^-$ state and the spin forbidden $(b^1\Sigma^+, a^1\Delta) \rightarrow X^3\Sigma^-$, and the spin allowed $A^3\Pi - X^3\Sigma^-$ and $c^1\Pi \rightarrow (b^1\Sigma^+, a^1\Delta)$, radiative transitions. *J. Chem. Phys*, 91(8):4745–4757, 1989.

[171] L. Y. Yeung, L. T. Murray, J. L. Ash, E. D. Young, K. A. Boering, E. L. Atlas, S. M. Schauffler, R. A. Lueb, R. L. Langenfelds, P. B. Krummel, L. P. Steele, and S. D. Eastham. Isotopic ordering in atmospheric O_2 as a tracer of ozone photochemistry and the tropical atmosphere. *Journal of Geophysical Research: Atmospheres*, 121(20):12,541–12,559, 2016.

[172] Y. L. Yung, M. A. Allen, and J. P. Pinto. Photochemistry of the atmosphere of Titan - comparison between model and observations. *The Astrophysical journal. Supplement series*, 55:465–506, 1984.

VITA

Anton M. Fernando
B.S. November 2011, University of Colombo, Sri Lanka
M.S. May 2014, Old Dominion University
Department of Physics
Old Dominion University
Norfolk, VA 23529

Anton Fernando earned his Bachelor of Science degree in physics from University of Colombo (Sri Lanka) in 2011. Anton joined the Department of Physics of Old Dominion University (Norfolk, VA) in 2013 and completed him Masters of Science degree in physics in 2014.

Typeset using LaTeX.